When superconductivity crosses over: From BCS to BEC

Qijin Chen

Hefei National Research Center for Physical Sciences at the Microscale and School of Physical Sciences, University of Science and Technology of China,
Hefei, Anhui 230026, China,
Shanghai Research Center for Quantum Science and CAS Center for Excellence in Quantum Information and Quantum Physics, University of Science and Technology of China,
Shanghai 201315, China,
and Hefei National Laboratory, University of Science and Technology of China,
Hefei 230088, China

Zhiqiang Wang

Department of Physics and James Franck Institute, University of Chicago,
Chicago, Illinois 60637, USA,
Hefei National Research Center for Physical Sciences at the Microscale and School of Physical Sciences, University of Science and Technology of China,
Hefei, Anhui 230026, China,
Shanghai Research Center for Quantum Science and CAS Center for Excellence in Quantum Information and Quantum Physics, University of Science and Technology of China,
Shanghai 201315, China,
and Hefei National Laboratory, University of Science and Technology of China,
Hefei 230088, China

Rufus Boyack

Department of Physics and Astronomy, Dartmouth College,
Hanover, New Hampshire 03755, USA

Shuolong Yang

Pritzker School of Molecular Engineering, University of Chicago, Chicago, Illinois 60637, USA

K. Levin

Department of Physics and James Franck Institute, University of Chicago,
Chicago, Illinois 60637, USA

(published 23 May 2024)

New developments in superconductivity, particularly through unexpected and often surprising forms of superconducting materials, continue to excite the community and stimulate theory. It is now becoming clear that there are two distinct platforms for superconductivity: natural and synthetic materials. The study of these artificial materials has greatly expanded in the past decade or so, with the discoveries of new forms of superfluidity in artificial heterostructures and the exploitation of proximitization. Natural superconductors continue to surprise through Fe-based pnictides and chalcogenides, and nickelates as well as others. This review presents a two-pronged investigation into such superconductors, with an emphasis on those that have come to be understood to belong somewhere between the Bardeen-Cooper-Schrieffer (BCS) and Bose-Einstein condensation (BEC) regimes. The nature of this "crossover" superconductivity, which is to be distinguished from crossover superfluidity in atomic Fermi gases, is a focus here. Multiple ways of promoting a system out of the BCS and into the BCS-BEC crossover regime are addressed in the context of concrete experimental realizations. These involve natural materials, such as organic conductors, as well as artificial, mostly two-dimensional materials, such as magic-angle twisted bilayer and trilayer graphene, or gate-controlled devices, as well as one-layer and interfacial superconducting films. Such developments should be viewed as a celebration of BCS theory, as it is now clear that, even though this theory was initially implemented with the special case of weak correlations in mind, it can be extended in a natural way to treat the case of these more exotic strongly correlated superconductors.

CONTENTS

I. INTRODUCTION: BACKGROUND AND HISTORY

There has been a recent abundance of papers addressing a new form of superconductivity. Superconductivity as traditionally addressed within the well-known Bardeen-Cooper-Schrieffer (BCS) theory (Bardeen, Cooper, and Schrieffer, 1957) arises in metals when an attractive interaction is present. We often refer to this attractive interaction as the pairing glue. This attraction causes fermions to form pairs, called Cooper pairs, that are in some sense "bosonic" (Schrieffer, 1964). Because of this connection to bosonic statistics, the ground state of the pairs can effectively counteract the Pauli exclusion principle. Thus, as in a Bose system, the ground state of fermion pairs can now be macroscopically occupied, and the system thereby condenses. This BCS form of condensation, however, is not the same as the phenomenon of Bose-Einstein condensation (BEC), which is appropriate for Bose systems, in which all fermionic degrees of freedom have disappeared.

But something different from the BCS picture is found in a new generation of superconductors in which it appears that there is an anomalously strong pairing glue (of unspecified origin). We refer to these systems as strongly correlated superconductors, and we characterize their form of superconductivity as being described by a machinery that is neither the more familiar BCS theory nor does it correspond to BEC; here the fermionic degrees of freedom are not completely absent. These superconductors are said to be described via "BCS-BEC crossover theory." This new type of condensation phenomenon also appears to be present in ultracold atomic Fermi gases, where it has been widely studied (Chen *et al.*, 2005; Giorgini, Pitaevskii, and Stringari, 2008; Randeria and Taylor, 2014).

An interesting fact is that there is now a large class of recently discovered superconductors that appear to exhibit BCS-BEC crossover-like characteristics. These include iron-based superconductors, organic superconductors, magic-angle twisted bilayer graphene (MATBG) and magic-angle twisted trilayer graphene (MATTG) gate-controlled two-dimensional devices, interfacial superconductivity, and magnetoexcitonic condensates in graphene heterostructures. High-transition-temperature cuprates may also be included in this class.

We note here an important characteristic of BCS-BEC crossover theory aside from the previously discussed ground state. In this theory, because the pairing interaction is stronger than in conventional materials, it follows that fermion pairs form before they Bose condense at the superfluid transition temperature T_c. We find in the review that this property leads to a variety of experimental implications. It is in sharp contrast to the well-established theory of BCS, where (because the attractive interaction is extremely weak) pairing and condensation occur at exactly the same temperature; there is no hint that a given BCS superconductor will undergo the phase transition at any temperature above T_c.

This review addresses these issues in considerable depth and describes what has been observed in these two-dimensional (2D) and three-dimensional (3D) superconductors, which appear to be somewhere between BCS and BEC. We show how their various experimentally measured characteristics relate to BCS-BEC crossover, paying special attention to 2D materials, where there seem to be a surprisingly large number of examples. In the process, we present a theoretical understanding of the crossover formalism at general temperatures.

Lest there be any confusion at the start, throughout this review what we mean by BCS-BEC crossover is not the onset or proximity to the BEC regime as defined by some researchers, but rather an intermediate regime between BCS and BEC, where a significant departure from strict BCS theory is apparent. We also emphasize that what is being discussed here pertains to the theoretical "machinery" of superconductivity rather than the microscopic pairing mechanism.

We begin the discussion of BCS-BEC crossover by following the original discovery papers (Eagles, 1969; Leggett, 1980), which focused on a particular choice of ground state, namely, that having the form originally introduced in BCS theory. While there is a body of literature on alternative approaches to BCS-BEC crossover in the solid state (some of which is reviewed here), we focus mainly on this so-called BCS-Leggett ground state and its finite-temperature implications (Kadanoff and Martin, 1961), rather than on variants that have ground states that are incompletely characterized and less well understood.

The appreciation of this broader applicability of BCS theory and its straightforward extension to a form of Bose condensation underlines how remarkable the original contribution of Bardeen, Cooper, and Schrieffer was. We note that their discovery has provided support and a crucial framework for multiple Nobel prizes (on the order of ten or so) besides their own, including those in nuclear and particle physics. In this way, the recognition of its even greater generality is particularly significant.

This recognition can be credited to two physicists: A. J. Leggett (Leggett, 1980) and D. M. Eagles (Eagles, 1969). Leggett's contribution was motivated by the discovery of a BCS-like triplet-pairing state in neutral superfluid helium-3. Leggett emphasized that this form of fermionic superfluidity has features that are distinct from conventional superconductors; here the Cooper pairs have complex degrees of freedom. Moreover, the underlying attraction that leads to superconductivity in this neutral system must derive from a distinct pairing mechanism (Levin and Valls, 1983).

In making his claims, Leggett pointed to the sweeping generality of the BCS ground state,

$$\Psi^{\text{BCS}} = \Pi_{\mathbf{k}}(u_{\mathbf{k}} + v_{\mathbf{k}} a^{\dagger}_{\mathbf{k},\uparrow} a^{\dagger}_{-\mathbf{k},\downarrow})|0\rangle, \qquad (1)$$

where $a^{\dagger}_{\mathbf{k},\uparrow} a^{\dagger}_{-\mathbf{k},\downarrow}$ creates a pair of fermions with opposite spins and opposite momenta $\mathbf{k}$ and $-\mathbf{k}$ from the vacuum ($|0\rangle$).

The broader applicability of this wave function is accessed by self-consistently adjusting the variational parameters $u_{\mathbf{k}}$ and $v_{\mathbf{k}}$ as one varies the strength of the attractive interaction. This accommodates a continuous evolution from weak to strong pairing. One can replace $u_{\mathbf{k}}$ and $v_{\mathbf{k}}$ with more experimentally relevant parameters: the fermionic chemical potential μ and the zero-temperature fermionic excitation gap parameter

$$\Delta_0 \equiv \Delta(T = 0).$$

These are two important parameters that we refer to throughout this review. Notably the wave function Ψ^{BCS} supports a smooth transition between a BCS- and a BEC-like phase. The former is characterized by a large pair size, a small Δ_0, and a chemical potential equal to the noninteracting Fermi energy (E_{F}). In the latter case the pair size is small, Δ_0 is large (comparable to or even larger than E_{F}), and μ is negative.

We emphasize that this BEC phase is specific to the ground-state fermionic wave function and need not represent that of a true weakly interacting Bose gas. Note that within a generalized BCS framework it is relatively straightforward to address finite temperatures above and below T_c (Kadanoff and Martin, 1961); this is, in part, a consequence of the fact that the pairing formalism is closely related to an exactly solvable many-body problem (Richardson, 1963).

In a related way, Eagles (1969) also made groundbreaking observations. Eagles should be credited with emphasizing the concept of "pairing without superconductivity." This preformed-pair normal-state scenario is at the heart of BCS-BEC crossover theory once the attraction strength is beyond the BCS regime. Eagles should also be credited with drawing attention to the possibility that superconductivity in lightly doped semiconductors can be described by a form of BCS-BEC crossover. Indeed, we see in this review that there is currently renewed interest in these superconductors with low carrier density.

Conventions and notation. We follow standard notations as much as possible. They are summarized in the List of Symbols and Abbreviations. When we specify the interaction parameter U as increasing or decreasing, we always refer to the absolute value.

Throughout this review, we use the convention for units where it is not explicitly spelled out: $\hbar = k_{\text{B}} = c = 1$. In numerics, we set the volume to unity and $E_{\text{F}} = T_{\text{F}} = k_{\text{F}} = 2m = 1$ for the free-space cases, which leads to $n = 1/3\pi^2$ in three dimensions.

For the lattice cases, we take the half bandwidth $W = zt = 1$ and lattice constants $a = b = c = 1$. In a simple (quasi-)2D square or 3D cubic lattice, $n = 1$ at half filling.

Our fermionic chemical potential μ is measured with respect to the bottom of the noninteracting energy band, such that $\epsilon_{\mathbf{k}=0} = 0$. (i) This leads to $\mu = E_{\text{F}}$ in the noninteracting limit at $T = 0$, and (ii) μ changes sign when the system crosses the boundary between the fermionic and bosonic regimes.
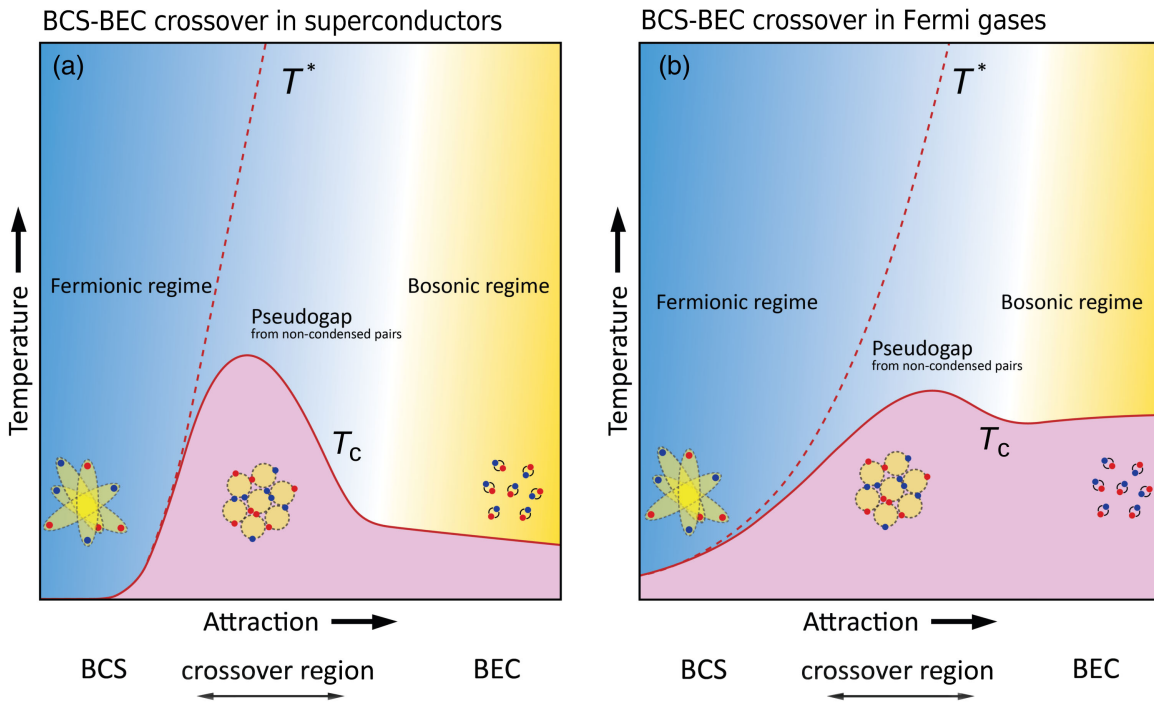
FIG. 1. Contrasting behavior of the 3D *s*-wave BCS-BEC crossover phase diagram for (a) superconductors, as in the attractive Hubbard model, and (b) Fermi gases with contact interactions and a free-particle dispersion. Note the contrasting behavior in the BEC regime where T_c approaches either (a) zero or (b) a finite number. Also important is the ubiquitous dome shape in the solid-state system. The minimum or shoulder in both T_c curves marks a transition to a different physical regime, as it corresponds to the onset of a bosonic superfluid, with $\mu = 0$. We emphasize here that the crossover regime begins at the point where the two temperature scales T^* (corresponding to the opening of a pairing gap) and T_c become distinct. Microscopic units for the superconducting case are provided in Fig. 12(a) in Sec. V.C.

A. Early theoretical work: Extending BCS-BEC crossover theory to finite temperatures

In 1985, Noziéres and Schmitt-Rink (NSR) began to think about going beyond the ground state and including the effects of finite temperature. They wrote a well-known and important paper (Nozières and Schmitt-Rink, 1985) that brought attention back to the earlier work by Eagles and Leggett and presented an in-depth discussion of the ground state given in Eq. (1). Moreover, they suggested an approach for computing the transition temperature T_c. Note, however, that the extrapolated ground state associated with NSR's finite-temperature theory is different (Diener, Sensarma, and Randeria, 2008) than the expression Ψ^{BCS} in Eq. (1). Additionally, NSR were the first to emphasize that BCS-BEC crossover theory in a solid-state lattice system assumes a character in the strong-coupling BEC regime that is significantly different from that of a Fermi gas.

Figure 1 relates to this observation. It compares the phase diagram for BCS-BEC crossover in (a) a lattice as contrasted with (b) a Fermi gas. A central difference arises from the kinetic-energy degrees of freedom associated with the motion of fermions in solids having a periodic lattice that is distinct from their motion in free space. The most striking consequence is that in a solid T_c in the BEC regime can become arbitrarily small as the pairing strength increases. Indeed, we emphasize this distinction in this review, as it bears on the relevance (or lack thereof) of the ultracold atomic Fermi-gas superfluids to the solid-state superconductors discussed here.

Related work in the form of a review was written by Micnas, Ranninger, and Robaszkiewicz (1990), who addressed superconductors in the BEC-like or strong-attraction limit. In their approach, a local pairing scenario was adopted, rather like treating a hard-core Bose gas on a lattice. The emphasis was on clarifying the various alternative phases that compete with superconductivity. Subsequently, the finite-temperature theory of the NSR paper was followed by work from Sá de Melo, Randeria, and Engelbrecht (1993), who provided its functional-integral reformulation.

At around the same time and in collaboration with Trivedi and Randeria (1995), Sá de Melo, Randeria, and Engelbrecht presented a series of papers using quantum Monte Carlo (QMC) simulation techniques to address normal-state features of the attractive 2D Hubbard model. This was thought to be relevant to high-temperature superconductivity and its anomalous "pseudogap" phase. This phase corresponds to a "normal" state above T_c in which there is a gap for fermionic excitations. Sá de Melo, Randeria, and Engelbrecht (1993) presumed that the pseudogap was associated with pairing in the absence of condensation.[1]

The onset temperature for such a normal-state gap is called T^*. Although there are a number of competing explanations, understanding the origin of this pseudogap, which shows up in thermodynamics and transport (Timusk and Statt, 1999), has been a central focus in the cuprate field. We emphasize that the

---

[1]They noted that their particular numerics supported the interpretation of the pseudogap (or equivalently a normal-state excitation gap) as a "spin gap" in which the charge degrees of freedom did not equally participate.

pseudogap and the distinct temperature scales $T^* \neq T_c$ both play important roles in general BCS-BEC crossover physics and are discussed throughout this review. They are also depicted in the schematic comparison plot in Fig. 1.

B. BCS-BEC crossover in cold-atom experimental research

Because the cold-atom systems constitute ideal laboratories for investigating the phenomena of BCS-BEC crossover (albeit in a Fermi gas), it is useful next to summarize the groundbreaking achievements beginning in around 2003, when Fermi condensates in trapped atoms were first reported. Condensation was observed initially (Greiner, Regal, and Jin, 2003; Jochim *et al.*, 2003) at strong coupling in the BEC regime (where $\mu < 0$) and shortly thereafter (Regal, Greiner, and Jin, 2004; Zwierlein *et al.*, 2004) at intermediate coupling (in a "unitary" gas, where the chemical potential was positive). These experiments should be recognized by the solid-state physics community as a true *tour de force*. Researchers managed to surmount multiple challenges stemming from the facts that the atomic gases are charge neutral, that they are confined to inaccessible traps, and that there is no direct way of measuring their temperature.

As a result, in the first few generations of experiments, "proof" of superfluidity was established indirectly through magnetic-field sweeps. These sweeps make use of a Feshbach resonance to take a gas in the more fermionic regime and quickly change the magnetic field, thereby projecting the system onto the strong-pairing regime. In this limit, a bimodality in the density profiles of the fermion pairs, with a narrow central peak on top of a broad distribution, reveals the presence of a condensate along with thermally excited pairs. In the following year or two, subsequent experiments made claims for superfluidity through measurements of the specific heat (Kinast *et al.*, 2005), and later it was definitively established through direct observation of quantized vortices (Zwierlein *et al.*, 2005).

With increased understanding of these Fermi-gas superfluids, the community then focused on additional probes such as transport (Sommer *et al.*, 2011; Joseph, Elliott, and Thomas, 2015) and additional complexities associated with spin-imbalanced or polarized gases (Partridge *et al.*, 2006; Zwierlein *et al.*, 2006) (much like superconductors in magnetic fields), as well as in optical lattices (Chin *et al.*, 2006). Along these lines, there were interesting accompanying theoretical contributions (Chien, Chen *et al.*, 2006; Radzihovsky and Sheehy, 2010), as well as those that contemplated even more exotic phases (for example, spin-orbit coupled and topological phases) (He *et al.*, 2013; J. Zhang *et al.*, 2014; Anderson *et al.*, 2015; Wu *et al.*, 2015a). Also notable were the contrasts with solid-state superconductors centered around low viscosity or "perfect" fluids (Kovtun, Son, and Starinets, 2005; Guo *et al.*, 2011a) in the Fermi gases and "bad metals" (Gunnarsson, Calandra, and Han, 2003; Guo *et al.*, 2011b) associated with highly resistive transport, as in cuprate superconductors.

The collective contribution of the dedicated experimental groups who met the challenge of finding and characterizing these Fermi condensates deserves great respect. Among these groups were Greiner, Regal, and Jin (2003), Regal, Greiner, and Jin (2004), and Stewart, Gaebler, and Jin (2008);

Zwierlein *et al.* (2003, 2004); Jochim *et al.* (2003) and Bartenstein *et al.* (2004); O'Hara *et al.* (2002) and Kinast *et al.* (2004); Zhang, Sackett, and Hulet (1999) and Strecker, Partridge, and Hulet (2003); and Bourdel *et al.* (2004).

Among the first to apply BCS-BEC crossover theory to cold gases were Ohashi and Griffin (2002), who implemented the theory of Nozières and Schmitt-Rink (1985). This was followed by our work (Stajic *et al.*, 2004), which, shortly before the 2003 discovery, called attention to the expected importance of a pseudogap in these cold gases. This in turn helped motivate experimental efforts beginning with early observations of possible pseudogap signatures (Jochim *et al.*, 2003) using rf spectroscopy (Chin *et al.*, 2004). Later research by Stewart, Gaebler, and Jin (2008) introduced a rather ingenious analog of angle-resolved photoemission spectroscopy (ARPES) to investigate the pseudogap in more detail. These experiments were revisited more recently with some of the trap complications removed using a so-called box trap, where pseudogap effects appear to be more prominent (Li *et al.*, 2024).

In addition to this focus on the pseudogap, substantial effort was devoted to the unitary gas, which is intermediate between BCS and BEC, where the scattering length becomes infinite. Here precise numbers for thermodynamic features, variables in the equation of state, and special interrelationships (Tan, 2008; Nascimbène *et al.*, 2010; Ku *et al.*, 2012) provided a series of challenges to test the numerical accuracy of different BCS-BEC crossover theories.

C. Hamiltonian and interpretation of the ground-state wave function

All discussions of detailed theory are deferred to later sections of the review, but for the purposes of an overview we next introduce the underlying Hamiltonian. As in all superconductors, it is assumed that electrons are paired in the superconducting phase. This pairing arises from an attractive interaction. In strict BCS theory, pairing takes place only between electrons with opposite momenta $(\mathbf{k}, -\mathbf{k})$. More generally, in BCS-BEC crossover theory we consider pairings between $\mathbf{k} + \mathbf{q}/2$ and $-\mathbf{k} + \mathbf{q}/2$, where the pair momentum $\mathbf{q}$ can be arbitrary but generally is small (compared to k_F). This pairing physics is described by the following Hamiltonian:

$$
\begin{aligned}
\mathcal{H} = & \sum_{\mathbf{k}\sigma} \epsilon_{\mathbf{k}} a_{\mathbf{k}\sigma}^{\dagger} a_{\mathbf{k}\sigma} \\
& + \sum_{\mathbf{k},\mathbf{k}',\mathbf{q}} V_{\mathbf{k}\mathbf{k}'} a_{\mathbf{k}+\mathbf{q}/2\uparrow}^{\dagger} a_{-\mathbf{k}+\mathbf{q}/2\downarrow}^{\dagger} a_{-\mathbf{k}'+\mathbf{q}/2\downarrow} a_{\mathbf{k}'+\mathbf{q}/2\uparrow}, \quad (2)
\end{aligned}
$$

where $a_{\mathbf{k}\sigma}^{\dagger}$ creates an electron in the momentum state $\mathbf{k}$ with spin σ and $\epsilon_{\mathbf{k}}$ is the kinetic-energy dispersion. We assume a separable potential $V_{\mathbf{k}\mathbf{k}'} = U\varphi_{\mathbf{k}}\varphi_{\mathbf{k}'}$, where $U = -|U|$ is the attractive coupling strength; the momentum-dependent function $\varphi_{\mathbf{k}}$ determines the symmetry of the order parameter. For a contact potential or on-site interactions $\varphi_{\mathbf{k}} = 1$, whereas for d-wave cuprate superconductors $\varphi_{\mathbf{k}} = \cos k_x - \cos k_y$. To avoid this notational complexity here we drop $\varphi_{\mathbf{k}}$ in the forthcoming equations and set the volume to unity in free space. Similarly, we choose the lattice constant to be 1 for the lattice case.

In Eq. (2) we assume spin-singlet pairing, which is relevant for both simple s-wave and d-wave superconductors. We do not make any assumptions in this review about the origin or

the detailed nature of the interaction, other than that it is attractive. The energy dispersion $\epsilon_{\mathbf{k}}$ can be associated with either a lattice or a free gas. We generally consider only a one-band model (with the exception of Sec. V.E, where band topology plays a role), but this Hamiltonian can be extended to include more bands and a finite range of interaction. For the *s*-wave case on a lattice, the interaction $V_{\mathbf{kk'}}$ in Eq. (2) corresponds to an attractive Hubbard model with on-site interactions. We have found that the effect of a finite range is generally not qualitatively important in the context of BCS-BEC crossover. In the *d*-wave case, $V_{\mathbf{kk'}}$ is in general nonlocal in real space and should be regarded as an approximation to the actual pairing interaction in real materials.

Note that when we refer to a finite-**q** pairing, this does not refer to condensed Larkin-Ovchinnikov (Larkin and Ovchinnikov, 1965) or Fulde-Ferrell phases (Fulde and Ferrell, 1964), but rather to noncondensed or thermally excited pair states. These are to be distinguished from condensed pairs having zero center-of-mass momentum. We emphasize that BCS-BEC crossover deals with superconductors that have strong pairing or strong "glue." This characterizes the interaction term in the Hamiltonian, where it is assumed that the pairing strength $|U|$ is not small compared to the kinetic energy. As a result of large $|U|$, pairing and condensation will take place at different temperatures. In particular, at the superconducting transition temperature T_c there will be a finite number of noncondensed pairs present.

Note that $\mathcal{H}$ in Eq. (2) is a many-body Hamiltonian, and there are many ways of solving it. In this review and as in the literature (Leggett, 1980), we base our solution on a variational ground state of the BCS form that was presented in Eq. (1). By contrast with strict BCS theory, we allow the attractive interaction to be arbitrarily strong, assuming that this does not change the generic form of the variational wave function Ψ^{BCS}. We emphasize that Ψ^{BCS} is not an exact solution of Eq. (2), but rather an approximation that presumes that the system does not make large excursions from BCS theory, no matter how strong the attraction is. Throughout this review we adopt this version of BCS-BEC crossover theory. Unless otherwise indicated, all equations that we present in the review are based on this ground state and its finite-temperature implications.

We emphasize that the advantage of this approach to BCS-BEC crossover theory is that we are dealing with a known ground state. This preserves the fundamental way that superconductivity has come to be understood. Another advantage of the BCS wave function is that these Cooper pairs form an essentially ideal gas. One can see this from the form of the BCS wave function of Eq. (1), which can be rewritten as $\Psi^{\mathrm{BCS}} \propto e^{b_0^\dagger}|0\rangle$, with the composite bosonic operator $b_0^\dagger = \sum_{\mathbf{k}}(v_{\mathbf{k}}/u_{\mathbf{k}})a_{\mathbf{k},\uparrow}^\dagger a_{-\mathbf{k},\downarrow}^\dagger$. Thus, this condensate corresponds to a ground state containing bosons that interact directly with the fermions and only indirectly with each other (Combescot, Pogosov, and Betbeder-Matibet, 2013; Combescot, Combescot, and Dubin, 2017). This makes for a simpler and more solvable many-body problem (Richardson, 1963).

One could contemplate other ground states with a structure different from the Gaussian-like Ψ^{BCS}, in which one has a composite bosonic operator in the exponent that involves four or more fermionic creation operators (Tan, 2008). Such approaches can be viewed as more equivalent to a weakly interacting theory of bosons: Bogoliubov theory. But a more complicated theory such as this is not necessarily an improvement, as Bogoliubov theory for bosons is known to be inappropriate at temperatures near T_c, or even well above $T = 0$ but far below T_c, as it is strictly a low-temperature theory.

Nevertheless, the known weaknesses of the BCS-Leggett approach should be clarified at this point. In particular, such an approach leads to inaccuracies in numerical values of thermodynamic parameters associated with the unitary gas. One can attribute this in part to the approximate treatment of the particle-hole channel for BCS-based theories, which focus primarily on the particle-particle channel. This is evident through the Bertsch parameter appearing as the ground-state fermionic chemical potential ratio μ/E_{F} of the unitary Fermi gas. This is found experimentally (Ku *et al.*, 2012) to be around 0.37, whereas in the BCS ground state this parameter is equal to 0.59 (Viverit *et al.*, 2004).

D. Kadanoff and Martin interpretation: BCS theory as a Bose condensation of electron pairs

Knowing the ground state still leaves the challenge of how to introduce finite-temperature effects. At this stage, to gain further physical insight into BCS-BEC crossover theory, it is useful first to revisit an approach due to Schafroth (1955). Two years before the BCS ground state of Eq. (1) was proposed, Schafroth suggested a more expanded interpretation of superconductivity. He argued that superconductivity could be thought of as being associated with Bose condensation of an ideal charged Bose gas. While most in the community view Schafroth's scheme as appropriate to the extreme BEC, often called the local pair limit, here we consider this approach to fermionic superconductivity more generally for all systems beyond the strict BCS limit.

Schafroth argued that condensation sets in at the transition temperature T_c, where there are preformed electron pairs. The expression for this temperature, which follows that of an ideal Bose gas, is given by

$$T_c = \left(\frac{2\pi}{\mathcal{C}}\right)\frac{n_{\mathrm{B}}^{2/3}(T_c)}{M_{\mathrm{B}}(T_c)}, \tag{3}$$

where $\mathcal{C} = [\zeta(3/2)]^{2/3}$ with the Riemann zeta function $\zeta(3/2) \approx 2.612$. The parameters n_{B} and M_{B} represent the 3D number density and mass of the bosons. We view these as yet unspecified bosons representing fermion-pair degrees of freedom such that

$$n_{\mathrm{B}} \equiv n_{\mathrm{pair}}, \qquad M_{\mathrm{B}} \equiv M_{\mathrm{pair}}. \tag{4}$$

Note that at the time of the BCS discovery there was some resistance to Schafroth's notion that this approach had anything in common with BCS theory. The key point that Schafroth emphasized is that there must be a form of Bose condensation embedded in superconductivity theory and that this boson inevitably involves a pair of electrons.

Schafroth's work introduced an important question: What kind of out-of-condensate boson or preformed pair is in fact compatible with BCS theory? The answer to this query would allow us to compute the transition temperature after establishing a precise meaning for n_{pair} and M_{pair}. Presumably because this work predated BCS theory, Schafroth did not ascribe any complexity to these quantities, which we now think must depend on both temperature and attractive interaction strength. Because of the latter, we inevitably have to deal with BCS-BEC crossover physics.

The challenge to quantitatively characterize these out-of-condensate pairs at general temperatures T was met in an important paper by Kadanoff and Martin (1961). Just as Eagles (1969) and Leggett (1980) recognized the greater generality of the BCS ground-state wave function, Kadanoff and Martin provided key insights into the finite-temperature physics of BCS theory. Their work was based on a systematic study of the coupled equations of motion. This established how to characterize the noncondensed pairs associated with BCS theory (through their propagator or "t matrix").

Kadanoff and Martin made an important observation that related to the Schafroth picture. They stated, "Below [the transition] temperature … a nonperturbative, stable solution involving a Bose condensation of pairs can be derived within the pair correlation approximation … which [approximation] is identical with the one proposed by BCS … that the superconducting transition is a Bose condensation phenomenon [was] originally proposed by Schafroth [and co-workers]."

From their work, one infers that the BCS gap equation can be reinterpreted as a BEC condensation condition requiring that the noncondensed pairs have zero chemical potential (that is, they are gapless) at every $T \leq T_c$. This Hugenholtz-Pines constraint (Hugenholtz and Pines, 1959) is also a generalization of the familiar Thouless condition (Thouless, 1960). While in strict BCS theory all preformed pairs at the onset of the superconducting transition should be viewed as virtual, it is reasonable to presume that, once one enters the BCS-BEC crossover regime, these noncondensed pairs are no longer virtual, and their number and mass at general T can be quantified according to the prescription of Kadanoff and Martin.

The work that we summarize here should be differentiated from other approaches to BCS-BEC crossover, such as those of Nozières and Schmitt-Rink (1985), Sá de Melo, Randeria, and Engelbrecht (1993), Ohashi and Griffin (2002), and Pieri, Pisani, and Strinati (2004). Their finite-temperature analysis was presumably designed to accommodate some of the physics of bosonic Bogoliubov theory for the fermion pairs. In the NSR picture, which involves more strongly interacting composite bosons than would be associated with a BCS-like ground state, the bosonic degrees of freedom were described as follows (Nozières and Schmitt-Rink, 1985): "A bound pair [which] is a collective mode of the superfluid … T_c thus results from thermal excitation of collective modes." Their scenario can be compared to other work (Pieri and Strinati, 2005; Tan and Levin, 2006) that addresses the extreme BEC regime and investigates the nature of that fermionic ground-state wave function associated with a composite-boson Bogoliubov picture (including Lee-Huang-Yang corrections).

E. Mechanisms for driving BCS-BEC crossover

An important aim of this review is to communicate in physical terms what BCS-BEC crossover is and what it is not. More specifically, we ask the following questions: How do we know when a superconductor is promoted out of the BCS regime, and what are the typical mechanisms for promoting it?

It is useful to establish the variables that quantify the size of the deviation from BCS. One of these, the ratio T^*/T_c, has already emerged. When this ratio exceeds unity the superconductor may no longer be in the BCS regime. Here, as defined previously, T^* corresponds to that temperature at which a gap opens in the fermionic excitation spectrum, while T_c corresponds to the temperature for fermion-pair condensation. Strong pairing is not uniquely implied by large T^*/T_c; however, the converse is true. Notably there can be other mechanisms for this spectral gap opening.

By contrast, the presence of a large ratio of the zero-temperature gap to E_F, Δ_0/E_F, is more unambiguously suggestive of a system that has been promoted out of the BCS regime. Finally, there is a third, equally important parameter that quantifies the deviation from BCS theory. This corresponds to the size of the Ginzburg-Landau (GL) coherence length, which we define more precisely later in this section. When this is anomalously small, the system is presumed to be driven away from the BCS regime.

What, then, are the mechanisms that are responsible for driving a superconductor out of the BCS regime and into the BCS-BEC crossover regime? We identify three main mechanisms: low dimensionality, strong attraction, and low electronic energy scales.

We begin with the issue of low dimensionality, which is known to naturally introduce distinct energy scales T^* and T_{BKT}. Notably, as stated by Kosterlitz (2016), "The onset of superconductivity in 2D … requires a pre-existing condensate or pairing of electrons." One can understand this by noting that the underlying physical picture characterizing the onset of two-dimensional superconductivity [or the Berezinskii-Kosterlitz-Thouless (BKT) superconducting state (Berezinskii, 1972; Kosterlitz and Thouless, 1973)] assumes the separation of energy scales: phase coherence cannot occur until a pairing amplitude is established.

An equally important aspect of superconductivity in two dimensions is that there is a stronger tendency to pair. In particular, in the low-density limit where there is a quadratic band dispersion near the conduction band bottom, it follows that there is no critical value of the pairing interaction that is required to form two-body bound states. This is in contrast to the situation in three dimensions. Hence, the "pairing glue" in a 2D superconductor need not be anomalously strong to promote the system into the BCS-BEC crossover regime. These observations may explain why there are many 2D examples in the recent BCS-BEC crossover literature.

Figure 2 provides a key summary of different mechanisms for promoting a system out of the BCS regime. The figure quantifies the values of the attractive interaction at which a given 2D or 3D superconductor departs from BCS theory and enters into the BCS-BEC crossover regime, as well as where it enters into the BEC regime. Plotted on the vertical axis is T^*/T_c (or for the two-dimensional system T^*/T_{BKT}).
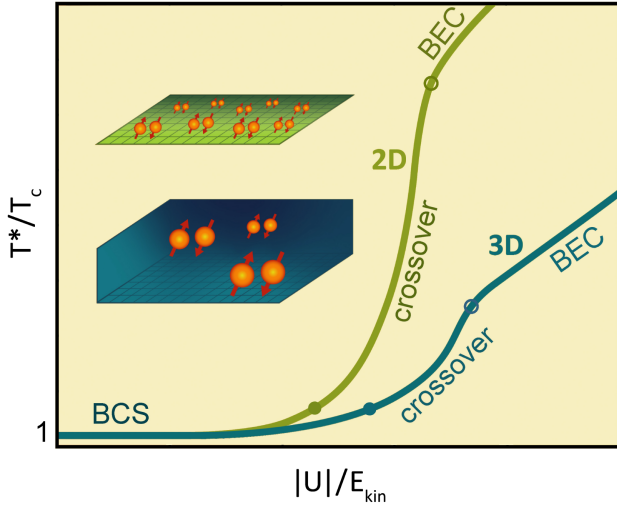
FIG. 2. Comparison of schematic phase diagrams in two and three dimensions for an attractive Hubbard model, based on plots of T^*/T_c as a function of the dimensionless attractive interaction $|U|/E_{kin}$. The onset of the departure from the BCS into the BCS-BEC crossover regime is determined from the point where the ratio T^*/T_c slightly exceeds unity, as shown by the solid circles. Thus, a relatively weaker attraction $|U|/E_{kin}$ is sufficient to promote a 2D superconductor out of the strict BCS limit, as compared to a 3D superconductor. Reaching either of these onset values for $|U|/E_{kin}$ (the solid circles) can be achieved by increasing the attraction $|U|$ or decreasing the electronic energy scales E_{kin}. Insets: schematic representations of the number of pairs (or pair density) in the 2D sheets or 3D volumes at these onsets. Also shown is the transition to the BEC regime, which is indicated by open circles. For actual units on this figure, see the inset in Fig. 12(a).

The horizontal axis indicates the strength of the dimensionless attractive interaction in units of a characteristic electronic energy scale E_{kin}.

A key observation about this figure is that a relatively weak attraction $|U|/E_{kin}$ is needed to promote a 2D superconductor as compared to a 3D superconductor out of the strict BCS limit. The point of departure from the BCS regime is associated with the point where T^*/T_c slightly exceeds unity, say, by 20%. Figure 2 is characteristic of the intermediate- and low-carrier-density regimes. The corresponding crossover values of $|U|/E_{kin}$ are indicated in the figure by the solid dots. This fraction can assume sufficiently large values as a consequence of a strong pairing glue; i.e., it is associated with anomalously large $|U|$. We might speculate that this stronger pairing scenario applies, if at all, to the cuprate superconductors. But the ratio can also be large when the characteristic electronic energy scales (called E_{kin}) become anomalously small. This can occur through flat bands (because of a small hopping integral, called t, or a small bandwidth) or through low electronic densities (which reduce E_F). We see in this review that both two dimensionality and/or small electronic energy scales are likely to be responsible for the many recent observations of BCS-BEC crossover superconductivity.

The fact that there is no critical value of the pairing required to form bound states in a moderately low-density 2D superconductor also serves to interpret the illustrations to the left of

the curves in Fig. 2. These are schematic representations of the number of pairs (or pair density n_{pair}) in the 2D sheets or 3D volumes at the onset of the transition. For the same fixed attractive interaction, Fig. 2 emphasizes that in two dimensions there is a significantly higher density of pairs at T_{BKT} than for the analog 3D system.

We end this discussion by referring back to the GL coherence length and showing that it provides a quantifiable measure of where a superconductor is within the BCS-BEC crossover spectrum. This is based on a calculation of T_{BKT} that is similar to the Schafroth-like result in Eq. (3) but here for the 2D limit. This analysis is abbreviated here as a summary and further discussed in Sec. V.

We approach the BKT state from the high-temperature side, and thus will use the methodology advocated for by the cold-atom community (Prokof'ev and Svistunov, 2002; Hadzibabic *et al.*, 2006; José, 2013), where in atomic Bose gases one finds some of the most convincing evidence for a Kosterlitz-Thouless state. Although originally much of this literature was focused on BKT for bosonic superfluids, by extension to fermionic superconductors and superfluids, one can deduce that this transition temperature roughly scales as[2]

$$T_{BKT} \sim \frac{n_B(T_{BKT})}{M_B(T_{BKT})}, \qquad (5)$$

where again these as yet unspecified bosons with a 2D number density n_B and mass M_B represent pair degrees of freedom, as defined in Eq. (4). Note that a fraction involving the same temperature-dependent terms $n_{pair}(T)$ and $M_{pair}(T)$ enters into both the 2D and 3D expressions for the transition temperature. Here the omitted prefactor represents a slightly more complicated term that is discussed later in the context of Eq. (23).

These Schafroth-like expressions for the transition temperatures in two and three dimensions [Eqs. (3) and (5)] then provide a simple expression for the important superconducting GL coherence length ξ_0^{coh}; this is given by $\hbar^2/[2M_{pair}(\xi_0^{coh})^2] = k_B T_c$ (Boyack *et al.*, 2018, 2019), where we have restored Planck's constant $\hbar$ and the Boltzmann constant k_B. As a result ξ_0^{coh} depends only on the pair density n_{pair} (presumed at the onset of the transition). Note that this coherence length reveals the location of a given system within the BCS-BEC crossover for the 2D case,

$$k_F \xi_0^{coh} \propto (n/n_{pair})^{1/2},$$

where k_F reflects the total particle density n, and a similar expression (with an exponent of $1/3$) can be obtained in the 3D case as well. Since the number of pairs at T_c varies from essentially 0 in the BCS limit to $n/2$ in the BEC case, this provides a measure of where a given superconductor is within the BCS-BEC crossover spectrum. This GL coherence length (Suzuki and Hikita, 1991) has been widely discussed in the recent literature on superconductivity (Nakagawa *et al.*, 2021; Park *et al.*, 2021; Suzuki *et al.*, 2022). It is accessible through the response to a magnetic field. Because it has been measured

---

[2]The proportionality constant between T_{BKT} and n_B/M_B in Eq. (5) has an additional double-logarithmic dependence (Fisher and Hohenberg, 1988) on n_B, which is weak.

in a large number of systems that are viewed as candidates for BCS-BEC crossover, it is addressed in some detail in this review.

II. OVERVIEW OF BCS-BEC CROSSOVER

A. Signatures of BCS-BEC crossover

Since the concept of BCS-BEC crossover is sometimes interpreted in different ways in the literature, we emphasize what we associate with the term *crossover* in this review. We consider here solid-state superconductors (as distinct from atomic Fermi gases) that are promoted out of the strict BCS regime through moderately strong pairing interactions (or through a combination of the mechanisms discussed in Sec. I.E). These interactions in turn lead to emerging bosonic degrees of freedom that coexist with a well-defined Fermi surface. With ever-increasing interaction strength, the bosonic component will eventually become dominant, leading to a disappearance of the fermiology; here the system enters the BEC regime. It is still an open question as to whether a BEC phase (with its attendant low transition temperatures) has ever been observed in a solid-state system. While some researchers (Sous, He, and Kivelson, 2023; Chen *et al.*, 2024) have identified crossover with the onset of the BEC regime, in this review we adhere to the conventional definition of BCS-BEC crossover emphasizing the associated new and interesting properties, which are distinct from those observed in either the BCS or BEC regime.

There are a number of signatures of BCS-BEC crossover, some of which we discussed in Sec. I and which we more precisely quantify here. Many of these features can have multiple interpretations. While the first three criteria in the following list are necessary conditions, a conclusion in support of the appropriateness of a BCS-BEC crossover for a particular superconductor often comes from a preponderance of evidence, rather than from any "smoking gun" single signature on this list. One makes the following observations:

(1) Large values of the normalized zero-temperature pairing gap Δ_0/E_F from ≈ 0.1 to 1.0.

(2) The presence of a normal-state gap (or pseudogap) with an onset at $T^*/T_c \gtrsim 1.2$.

(3) A moderately short coherence length that should be no longer than $k_F \xi_0^{coh} \sim 30$.

(4) Enhanced superconducting fluctuation-like behavior, particularly in the response to a magnetic field (such as the Nernst effect and diamagnetic susceptibility), well above T_c.

(5) A precursor downturn (Timusk and Statt, 1999; Boyack *et al.*, 2021) in the temperature dependence of the resistivity around the gap onset temperature T^*.

(6) The presence of bosonic (or pair) degrees of freedom above the transition. The pairing gap and the bosonic degrees of freedom are two sides of the same coin, although the latter aspect is more difficult to identify.

(7) BCS mean-field-like relations that characterize the ratio of the ground-state excitation gap Δ_0 and the pairing-onset temperature T^*.

(8) Two distinct energy gaps. In contrast to strict BCS theory, in the crossover regime the gap associated with

coherent superconducting phenomena that set in at T_c is distinct from that associated with bosonic or pair excitations, which appear in the vicinity of T^*.

(9) Normal-state experimental observations such as shot noise (Zhou *et al.*, 2019), which are indications of $2e$ charge carriers.

(10) The observation of BCS-like "back bending" (Kanigel *et al.*, 2008) of the electronic band dispersion in the vicinity of but above T_c.

B. Analogies with an ideal Bose gas

What is essential is that the treatment of BCS-BEC crossover, which we present here, be compatible with generalized BCS physics, both in the ground state and at all temperatures $T \leq T_c$. Unlike in strict BCS theory, in the crossover regime bosonic degrees of freedom or preformed pairs are already present at the onset of condensation. Their number progressively increases as the system evolves from BCS to BEC. These normal-state pairs are associated with an excitation gap (or pseudogap) in the fermionic spectrum, and in BCS-BEC crossover this implies that $\Delta(T_c) \neq 0$. The gap size increases continuously starting at nearly 0 in the BCS regime. The excited pair states involve a combination of two fermions associated with momenta $\mathbf{k} + \mathbf{q}/2$ and $-\mathbf{k} + \mathbf{q}/2$, where the pair momentum $\mathbf{q}$ is nonzero. Preformed pairs are necessarily distinct from condensed pairs, for which $\mathbf{q} = \mathbf{0}$.

To understand these preformed pairs we present a simple figure based on a close analogy to an ideal Bose gas. The upper row of Fig. 3 is a schematic representation of the temperature evolution of a BCS-BEC crossover superfluid. This shows that as temperature decreases below an onset temperature T^* a new form of quasiparticle or excitation appears. These noncondensed pairs are represented by dashed red circles. At the same temperature a pairing gap or pseudogap is present, which reflects the fact that there must be an input of energy to create fermionic excitations by breaking pairs. As temperature further decreases to just above T_c, the number of these preformed pairs increases. Note that the figure shows that there are also a number of unpaired fermions at the transition. The ratio of the boson to fermion number continuously increases from BCS to BEC. In the BCS limit the number of pairs at T_c is essentially 0, while in the BEC limit this number approaches $n/2$.

Below T_c, condensed pairs (solid blue circles) appear. As the temperature is further lowered, noncondensed pairs gradually (and, at $T = 0$, completely) convert to the condensate. There are no noncondensed pairs in the BCS-like ground state. Note that strict BCS theory is the special case where $T^* = T_c$ and concomitantly where the number of noncondensed bosons becomes arbitrarily small at any temperature T. This signals that there is essentially no pairing-related gap in the fermionic excitation spectrum at T_c.

C. Contrasting the present pair-fluctuation and phase-fluctuation scenarios

We emphasize that this pair-fluctuation picture of BCS-BEC crossover is not the same as the phase-fluctuation
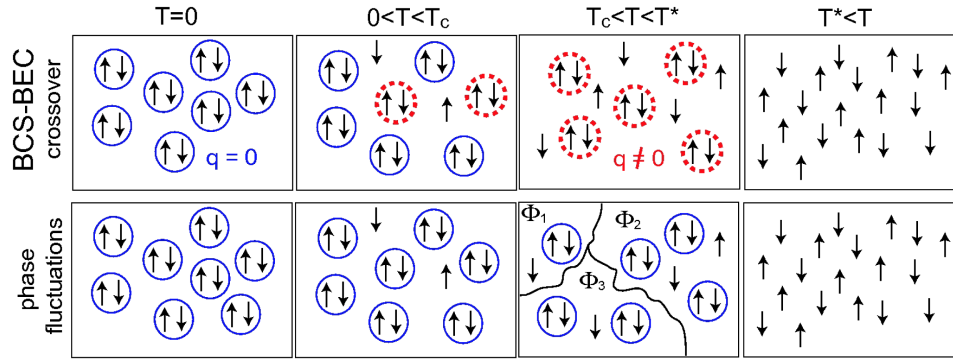
FIG. 3.   Comparison of the 3D BCS-BEC crossover and phase-fluctuation scenarios. Throughout, the closed blue circles, lone arrows, and dashed red circles represent condensed fermion pairs, unpaired fermions, and finite-momentum pairs, respectively. The crossover theory is distinguished by the presence of noncondensed pairs, whose center-of-mass momentum $\mathbf{q} \neq \mathbf{0}$, for nonzero temperatures below T^*. The defining feature of the phase-fluctuation picture is the presence of different phase domains above T_c, which are indicated by the regions labeled with distinct phases Φ_i.

scenario (Emery and Kivelson, 1995). There are similarities, but the contrast was stressed by Emery and Kivelson (Emery and Kivelson, 1995), who described the phase-fluctuation scenario as follows: "Our discussion attributes the properties of high-temperature superconductors to the low superfluid density … and not to a short in-plane coherence length and a crossover to real-space pairing."

The most significant differences would appear, then, to be attached to the driving mechanisms (small superfluid density versus strong attraction) behind the observed exotic normal states, as well as the pair "size" or in-plane coherence length. This can help researchers distinguish between the so-called phase-fluctuation picture and BCS-BEC crossover. A small coherence length or the observation of concomitant, moderately large Δ_0/E_F similarly lends support to the crossover scenario.

To compare these two scenarios, we return to Fig. 3. In the figure, the pair-fluctuation or BCS-BEC crossover picture in the upper panel is associated with a new type of paired quasiparticle (excited pair states), whereas the phase-fluctuation scenario in the lower panel relates to more collective behavior. In this collective behavior, low carrier density is associated with poor screening, which is then responsible for small phase stiffness. As a further point of contrast, we emphasize that all parameters pertaining to the fermionic sector (Δ_0, T^*, etc.) are essentially absent in the phase-fluctuation scenario, as this theory is an effective low-energy description of the bosonic degrees of freedom once the fermions are integrated out.

At the same time, the deep BEC limit of the BCS-BEC crossover scenario, where the fermions are essentially absent at T_c, will have features in common with the phase-fluctuation scenario. Similarly, in two dimensions, where fluctuation effects become more pronounced, the differences between the two approaches become more subtle, despite the fact that this bosonic regime is driven by strong pairing glue rather than low carrier density. Finally, we emphasize that phase fluctuations themselves will be present in the usually narrow critical region of temperatures near T_c in all superconductors once one includes the beyond-mean-field effects, which are not addressed in this review.

D. Quantitative summary of the present theory

It should not be surprising that accompanying the two forms of quasiparticles in the upper panel of Fig. 3 (in red and blue) are two different forms of fermionic excitation gaps: Δ_{PG} and Δ_{sc}. These represent the contributions from noncondensed and condensed pairs, respectively. Indeed, their squares will turn out to be proportional to the number density of these two types of pairs.

A more detailed theory (Chen *et al.*, 2005) discussed in Sec. III revealed that the gaps combine approximately in quadrature in such a way as to yield the total, physically measurable fermionic excitation gap called $\Delta(T)$. Thus,

$$\Delta^2(T) = \Delta_{sc}^2(T) + \Delta_{PG}^2(T). \tag{6}$$

In this way, the total number density of pairs, which is proportional to $\Delta^2(T)$, will determine the energy that must be applied in order to excite the fermions.

A central consequence of this picture, as we later establish, is that

$$\Delta^2(T) = \Delta_{BCS}^2(T) \quad \text{for } T \leq T_c, \tag{7}$$

where Δ_{BCS} is the mean-field gap obtained in BCS theory. In this way, in the ordered phase the total fermionic excitation gap coincides with the results of strict mean-field BCS theory.

As shown in Fig. 4, the two contributions to Δ^2, called Δ_{PG}^2 and Δ_{sc}^2, play a similar role as their respective counterparts in the ideal-Bose-gas scenario. The latter theory considers a decomposition of the total number of bosonic particles N_B in terms of those deriving from the excited bosons $N^{excited}$ and the condensed bosons N^{cond}. As a function of decreasing temperature, the former convert into the latter, so there are no excitations in the ground state. The temperature-dependent quantity N^{cond} is established by evaluating the difference $N_B - N^{excited}$.

In the crossover picture, as in an ideal Bose gas, the condensate contribution Δ_{sc}^2 is obtained by subtracting the

3D
Ideal Bose Condensate
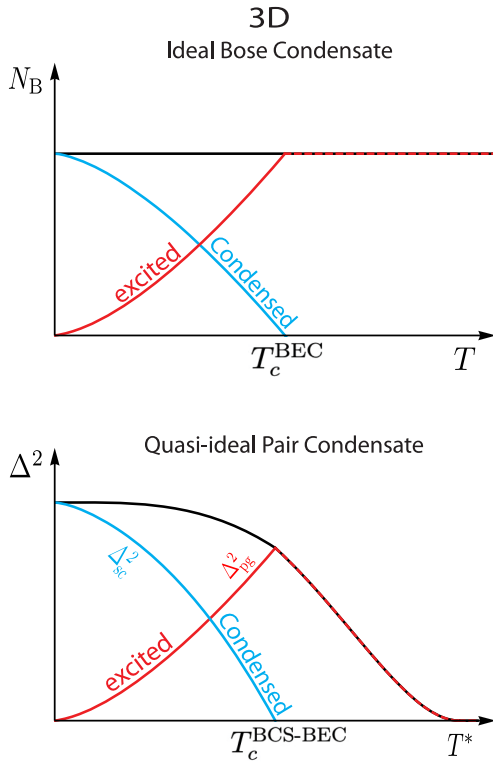

Quasi-ideal Pair Condensate

FIG. 4. Comparison of ideal-gas decomposition of the boson number N_B into condensed and excited contributions (upper panel) with the analog decomposition for a fermionic superfluid (lower panel) which involves the square of the pairing gap Δ^2 as a function of temperature T. T_c^{BEC} and $T_c^{\mathrm{BCS\text{-}BEC}}$ are the respective transition temperatures. The two gap contributions to Δ^2, called Δ_{PG}^2 and Δ_{sc}^2, are closely analogous to their counterparts in the ideal Bose gas. Indicated schematically is how to arrive at the transition temperature. This is associated with the intersection of the "excited" curve with either the total boson number curve (black line in the top panel) or the total Δ^2 curve (black line in the bottom panel), which marks the onset of the condensate contribution.

noncondensate piece Δ_{PG}^2 from the total Δ^2, which is approximated as $\Delta_{\mathrm{BCS}}^2(T)$ near but above T_c. This determines T_c from the condition that the noncondensed contribution is no longer sufficiently large to accommodate the full value of the mean-field gap squared. Thus, there must be an additional contribution from the condensate Δ_{sc}^2.

In this way, one can not only directly derive the Schafroth expression (Schafroth, 1955) shown in Eq. (3) but also write this same equation in a more familiar way from the perspective of BCS theory. In strict BCS theory, T_c is obtained from

$$1 = (-U) \sum_{\mathbf{k}} \frac{1 - 2f(|\xi_{\mathbf{k}}|)}{2|\xi_{\mathbf{k}}|} \bigg|_{T=T_c}, \qquad (8)$$

where $U < 0$ and $f(x) = 1/(e^{x/T} + 1)$ is the Fermi-Dirac distribution function. In Eq. (8) $\xi_{\mathbf{k}} = \epsilon_{\mathbf{k}} - \mu$ is the bare fermion dispersion measured from the Fermi level. We later see that, in the present BCS-BEC crossover theory, there is a similar expression for the determination of T_c,

$$1 = (-U) \sum_{\mathbf{k}} \frac{1 - 2f(\tilde{E}_{\mathbf{k}})}{2\tilde{E}_{\mathbf{k}}} \bigg|_{T=T_c}, \qquad (9)$$

where $\tilde{E}_{\mathbf{k}} \equiv \sqrt{\xi_{\mathbf{k}}^2 + \Delta^2(T_c)}$.

Thus, the central change from strict BCS theory [aside from a self-consistent readjustment of the fermionic chemical potential (Leggett, 1980)] is that T_c is determined in the presence of a finite excitation gap $\Delta(T_c)$. Solving for T_c involves finding the point of separation between $\Delta_{\mathrm{PG}}^2(T)$ and the mean-field gap $\Delta_{\mathrm{BCS}}^2(T)$ as a function of decreasing temperature, as shown in the bottom panel of Fig. 4.

We now have two different equations, Eq. (9) and the Schafroth expression in Eq. (3), both of which determine the transition temperature in the BCS-BEC crossover theory; both are intuitively reasonable. What is satisfying is to find that these two equations are equivalent, provided that one properly computes the number of pairs and their mass. Thus, this meets the goal of connecting a Schafroth-like approach to a more microscopic approach based on BCS theory. Schafroth's expression for T_c in this extended form is appropriate throughout the crossover once the system has emerged from the BCS limit such that $\Delta(T_c)$ is no longer strictly zero.

E. Qualitative summary of BCS-BEC crossover

Before going into more technical details of the present BCS-BEC crossover theory, as addressed in Sec. III, we now consider some of the more obvious questions that can be raised at this point. One of the first issues that arises is to clarify what is generic about BCS-BEC crossover theories. We note that BCS-BEC crossover theory belongs to the class of theories of strong-coupling superconductors. While there are a number of others in this class, what is essential is that this particular form of strong-coupling superconductivity is driven by charge $2e$ Cooper pairing. This differs from some of the alternative types of strongly correlated superconductors: spinon-holon pairing (Lee, Nagaosa, and Wen, 2006), kinetic-energy-driven superconductivity (Leggett, 1996), superconductivity strongly coupled to antiferromagnetism ["SO(5)"] (Demler, Hanke, and Zhang, 2004), and fractionalized electron superconductivity (Senthil and Fisher, 2000).

Moreover, within the BCS-BEC crossover class there are a number of variants, some of which are reviewed in Sec. II.F. Generically a BCS-BEC crossover theory of superconductivity represents an interpolation scheme between weak- and strong-coupling forms of $2e$-pairing-governed superconductivity. In the weak-coupling limit the fermions within a pair are loosely associated, whereas in the strong-coupling limit they become tightly bound. Between the two extremes, there is generally a smooth crossover. In all theories of the BEC regime in a lattice, the fermionic chemical potential lies below the bottom of the noninteracting conduction band. These generic features are illustrated in Fig. 1(a), which indicates how the transition temperature and pairing-onset temperatures smoothly vary between the fermionic and bosonic regimes.

There are, however, a number of features that are not generic in the family of BCS-BEC crossover theories. For example, not all theories reproduce BCS theory in the weak-coupling limit. Indeed, even the "BEC" limit has many

different interpretations. Some would argue that the BEC limit should be that of a true weakly interacting Bose system. Alternatively, in the present theory it is argued to be distinctly different, as this state is characterized through its fermionic properties even though a Fermi surface is no longer present. In such a BEC limit the fermionic pairing-gap parameter is large and temperature independent well above and below T_c. Among other features that are not generic is the presence in the intermediate-coupling regime of a pseudogap, which is indicated in Fig. 1. This pseudogap appears in some crossover theories (Strinati *et al.*, 2018), but not in others (Haussmann, Punk, and Zwerger, 2009; Morawetz, 2011).

More precisely the pseudogap corresponds to a gap in the fermionic excitation spectrum, which has a smooth onset at $T^* > T_c$. The pseudogap that we consider here enters into the theoretical framework as a distinct parameter Δ_{PG} and is more apparent (Levin *et al.*, 2010); in other approaches (Strinati *et al.*, 2018) it is only indirectly seen to be present through the behavior of the fermionic spectral function. This reflects the fact that electrons are starting to pair up at T^* and that breaking the pairs in order to create fermions will cost a gap energy. There is no true ordering or broken symmetry that takes place at T^*, only the onset of bosonic (pair) degrees of freedom. Because of the pseudogap, superconductivity at T_c will occur in the presence of a finite fermionic excitation gap $\Delta(T_c)$.

Additionally, we argue that these pseudogap effects persist below T_c, as they reflect the contribution of noncondensed pairs that are continuously converting to the condensate as temperature is lowered toward the ground state. Below T_c there is the additional energy gap deriving from the order parameter Δ_{sc}. It is often difficult to disentangle these two gap parameters, which reflect the energies that must be input to break the noncondensed and condensed pairs, and for many purposes they contribute additively in quadrature. Note that the pseudogap is not associated with superconducting coherence and is not responsible for Meissner or Josephson effects.

More concretely, this energy gap appears in both the charge and spin channels and, more generally, in thermodynamics and transport, which is in many respects similar to the way the below-T_c superconducting gap shows up in BCS theory. It enters, however, as a slightly rounded or smeared gap structure in normal-state tunneling and photoemission and leads to a gentle onset of a decrease in entropy with decreasing T. Note that the energy gap corresponds not to a true zero of the fermionic spectral function but rather to a depression that appears at energies around the chemical potential due to a finite lifetime of the noncondensed pairs.

In this approach, to a good approximation [see Eqs. (16) and (20)] the electron spectral function $A(\omega, \mathbf{k})$ depends on a self-energy of the form (Maly, 1997; Chen, Levin, and Kosztin, 2001)

$$\Sigma(\omega, \mathbf{k}) = \frac{\Delta_{PG}^2}{\omega + \xi_{-\mathbf{k}} + i\gamma} + \frac{\Delta_{sc}^2}{\omega + \xi_{-\mathbf{k}}}, \qquad (10)$$

which contains both gap parameters (here written for the s-wave case). Note the presence of a phenomenological parameter $i\gamma$, which reflects the fact that the noncondensed

pairs have a finite lifetime or are metastable. Its magnitude is not particularly important. In the normal state this expression is associated with a phenomenology widely used for the cuprates and introduced by Norman *et al.* (1998) in their analysis of ARPES data.

Additionally, the pseudogap can be detected indirectly through bosonic contributions that emerge as a result of the pairing of fermions; these are generally associated with familiar fluctuation transport signatures, as seen in a downturn in the dc resistivity around T^*.

In this review we connect the BCS-BEC crossover scenario to experiments. There is a challenge here because the fundamental tuning parameter $|U|$ of the BCS-BEC crossover is not accessible. This is in contrast to the Fermi gases where the interaction strength can be directly measured through a scattering length. What is most important is that it can be reasonably straightforward to replace the attractive interaction parameter, which always appears in traditional BCS-BEC crossover calculations on a lattice, in favor of measurable variables. This imposes a requirement on lattice crossover theories: a broad range of phenomena must be able to be addressed, thereby enabling connections to multiple experiments. The phenomena of interest involve parameters that scale directly or inversely with $|U|$. These are T^*/T_c, Δ_0/E_F, and $k_F \xi_0^{coh}$.

How to interpret experimental observations is the final important issue we consider in this qualitative summary section. In particular, one needs to determine whether there are experimentally verifiable or falsifiable conditions surrounding the applicability of BCS-BEC crossover. We identify qualitative trends that are seen through important correlations. These involve the fact that increases in Δ_0/E_F should be associated with increases in T^*/T_c, and that decreases in the coherence length, through $k_F \xi_0^{coh}$, should be correlated with increases in T^*/T_c. In this review these correlations are represented in a more quantitative fashion by detailed predictive curves. These are shown in Figs. 10, 12, 13, and 15 and, most importantly, in Figs. 36 and 40. Related issues have come up in experimental studies, as seen in Fig. 19. To address specific experiments, these predicted associations have to be tested carefully by changing an internal variable such as pressure or, possibly, doping within the same superconducting family.

F. Other theoretical approaches: Addressing BCS-BEC crossover on lattices

As emphasized in the Introduction, this review focuses primarily on a theoretical approach to BCS-BEC crossover based on the ground state of Eq. (1). Nevertheless, for completeness it is useful to give an overview of some alternative theoretical schemes in the literature that are particularly relevant to solid-state systems.

We first note that there is significantly less literature on BCS-BEC crossover theory in solid-state superconductors than in Fermi gases. For these atomic systems this extensive effort has largely been driven by experimental discoveries. Review articles (Chien *et al.*, 2010; Levin *et al.*, 2010) are available that summarized different variations of a t-matrix approach to BCS-BEC crossover theory at finite temperature. Key aspects of these comparisons are discussed in Sec. III.D,

albeit with an emphasis on applications to solid-state systems. Among the Fermi-gas reviews are those from our own group (Chen *et al.*, 2005), from Strinati *et al.* (2018), and from Zwerger (2012). In addition, extensive overviews were given by Randeria and Taylor (2014) and Bloch, Dalibard, and Zwerger (2008). What has not been as thoroughly reviewed is the next-generation research on crossover effects associated with superconductors in the solid state. Notable is an overview from Loktev, Quick, and Sharapov (2001), who covered early work through 2001.

This section presents an overview of alternative theories of crossover in the solid state. A key point to note here is that T_c approaches zero in the extreme BEC limit. This has to do with the fact that the hopping or kinetic degrees of freedom are associated with the fermions. The "composite bosons" do not directly hop on a lattice, even in the BEC regime, as a consequence of the assumed form for the Hamiltonian in Eq. (2). The depression of T_c in the BEC regime coincides with the onset of negative μ or, equivalently, where μ falls below the band bottom. Indeed, the transition to BEC can be seen in Fig. 1 to correspond to the onset of shoulders.

The fact that T_c in a superconductor progressively decreases with stronger coupling in the BEC regime was pointed out by Nozières and Schmitt-Rink and is reasonably straightforward to understand. The hopping of pairs requires the individual hopping of fermions, and when two fermions are tightly glued together this hopping is highly suppressed, leading to the asymptotic behavior seen in Fig. 1(a). More quantitatively, Nozières and Schmitt-Rink showed that this suppressed hopping of pairs varies as $t^2/|U|$, where t is the fermionic hopping matrix element and $|U|$ is the magnitude of the attractive interaction.

The contributions of Nozières and Schmitt-Rink (1985) are considered groundbreaking, and it is fitting that we discuss their work early in this section. Nevertheless, they expressed some reservations that should be noted, as they state that their particular "continuum model … provides an accurate description of the two [BCS-BEC] limits but [leads to] a failure for a lattice gas." In hindsight, this is probably an unduly negative assessment, but perhaps it bears on the rather small body of literature applying NSR theory to solid-state superconductors.

Most of the canonical features in the lattice phase diagram, such as those shown in Figs. 5(a)–5(c), including this $t^2/|U|$

asymptote, can be obtained from different BCS-BEC crossover theories. These involve the t-matrix-approximation-(TMA-) based approaches [of which there are three main categories (Chien *et al.*, 2010; Levin *et al.*, 2010), as discussed in Sec. III.D], dynamical mean-field theory (DMFT) (Georges *et al.*, 1996; Bauer and Hewson, 2009; Lin, Gull, and Millis, 2010; Koga and Werner, 2011; Kuchinskii, Kuleeva, and Sadovskii, 2015, 2016; Peters and Bauer, 2015; Sakai *et al.*, 2015; Park and Choi, 2019), quantum Monte Carlo simulations (Sewer, Zotos, and Beck, 2002), and the functional renormalization group method (Strack, Gersch, and Metzner, 2008), as well as other techniques. Among these, the TMA approach is principally analytical and thus provides more intuition about the relevant physical processes behind the crossover, making it the primary theoretical tool discussed in this review.

We can understand why there is a smaller body of analytical literature on lattice BCS-BEC crossover theories as compared to the Fermi gases. This is due in part to the fact that many of the sophisticated and insightful field theory techniques, such as large-N and ϵ expansions (Nishida and Son, 2006, 2007a; 2007b; Nussinov and Nussinov, 2006; Nikolić and Sachdev, 2007; Veillette, Sheehy, and Radzihovsky, 2007; Abuki and Brauner, 2008; Nishida and Son, 2010), are not directly adaptable to lattice systems. In the following we summarize some of the DMFT and QMC studies, highlighting a few prototypical phase diagrams shown in Fig. 5, which reflect a spectrum of different approaches in the literature. To begin, we note that Sewer, Zotos, and Beck (2002) provided a useful study of 3D comparative crossover approaches that yield the phase diagrams shown in Fig. 5(c). These are in many ways similar to their 2D analogs; see Fig. 5(b) for Monte Carlo–based results.

DMFT studies of the attractive Hubbard model (addressing either the ground state or the normal state) were presented by Keller, Metzner, and Schollwöck (2001), Capone, Castellani, and Grilli (2002), Garg, Krishnamurthy, and Randeria (2005), and Bauer and Hewson (2009). Some representative phase diagrams are presented in Fig. 5(a) (Koga and Werner, 2011). In DMFT, the attractive Hubbard model is mapped to an impurity problem on a lattice, which typically has a dimension that is effectively infinite. In this infinite-dimension limit, the fermionic self-energy associated with pairing becomes a
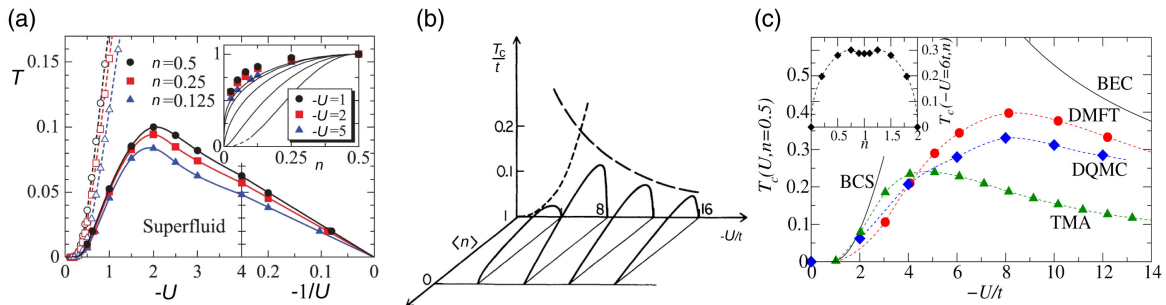

FIG. 5. Comparison of BCS-BEC crossover phase diagrams obtained from different theoretical approaches in the literature. All the diagrams are for a local attractive Hubbard model with attraction strength $|U|$ on a lattice. (a) Summary from Koga and Werner (2011) of dynamical mean-field calculations. The energy units are the half bandwidth associated with a Bethe lattice, having an infinite coordination number. (b) Quantum Monte Carlo result (Scalettar *et al.*, 1989) for a 2D square lattice with a nearest-neighbor hopping t. (c) Comparison of T_c calculated with different approaches in a 3D Hubbard model. (c) From Sewer, Zotos, and Beck, 2002.

function only of frequency. As a result, computing the self-energy can be reduced to self-consistently solving a local impurity problem, for which one can generally resort to various numerical methods. The advantage of DMFT is that it may capture local dynamical quantum fluctuations non-perturbatively, which can be important for a quantitative accounting of the quasiparticle spectral function at intermediate coupling ($|U|$ on the order of the bandwidth). However, DMFT is exact only in infinite dimensions because it ignores both spatial fluctuations beyond mean-field level and dimensional fluctuations. Therefore, the DMFT results need to be interpreted with care when one makes a quantitative comparison to other approaches in three or two dimensions.

Keller, Metzner, and Schollwöck (2001) provided an interesting DMFT study of the normal phase of the attractive Hubbard model showing that it is a Fermi liquid at weak coupling but consists of bound pairs and pseudogap physics at strong coupling. Perhaps surprisingly, the crossover between these two normal states may not be smooth at temperatures lower than T_c when the superconductivity is suppressed. There are indications at these low temperatures that, in this form of DMFT, a first-order transition occurs in the attractive Hubbard model between a thermally excited Fermi liquid state and a thermally excited bound-pair state as the attraction strength increases.

Figure 5(b) shows a Monte Carlo result for T_c or T_{BKT} for an attractive Hubbard model on a 2D square lattice with nearest-neighbor hopping (Scalettar *et al.*, 1989). At a generic electron filling level, the overall shape of the T_{BKT} vs $|U|/t$ curve is similar to its 3D counterpart, as shown in Fig. 5(c).

It is notable that, in two dimensions, it is more straightforward to arrive at a mean-field-level understanding of T_{BKT} varying from BCS to BEC (provided that the lattice is away from half filling). An illustrative example (Denteneer, An, and van Leeuwen, 1993) is based on calculations of the superfluid density or helicity modulus where one treats crossover effects at the mean-field level. This can be done either within the attractive Hubbard model or within its repulsive counterpart, which is obtained via a particle-hole transformation on the bipartite lattice. The T_{BKT} results calculated in this way are similar to those shown in Fig. 5(b).

For completeness, it is useful to highlight some additional literature contributions that address the physics of BCS-BEC crossover for fermions on a lattice. Closely related to the NSR theory (which has been mostly applied to the Fermi-gas state) is work by Wallington and Annett (2000) and Quintanilla *et al.* (2002), who studied lattice crossover theory using a functional-integral formalism, including Gaussian fluctuations. Their focus was on the effects of varying the symmetry of the order parameter within the extended attractive Hubbard model. Similarly, Tamaki, Ohashi, and Miyake (2008) also addressed NSR theory on a lattice, by providing an interesting comparison with other t-matrix theories.

It is also useful to summarize additional miscellaneous references of interest. Zero-temperature approaches based mainly on the BCS-like ground-state wave function in Eq. (1) were addressed by Andrenacci *et al.* (1999), Pistolesi and Nozières (2002), Herbut (2004), and Volcko and Quader (2012). Similarly relevant to topics in this review are observations about the contrast between s- and d-wave

superconductors (Loktev, Quick, and Sharapov, 2001), where it was noted that in the d-wave case moderate densities and large coupling suppress the BEC region of the phase diagram, leading to a premature disappearance of the superfluid phase deep inside the fermionic regime (Chen *et al.*, 1999).

Finally, by way of a digest of the more analytical theories of the crossover (for the gas as well as the lattice), we note that in describing BCS-BEC crossover effects it is tempting to introduce features of Bose superfluidity. As in Bogoliubov theory, this includes more direct interaction effects between bosons or pairs of fermions. One is saddled, however, with theoretical obstacles, as finite-temperature effects are much more difficult to include properly in Bose superfluids than in the BCS (fermionic) case. In strict BCS theory the entire temperature range is accessible, whereas in the Bose case one is restricted to the low-temperature regime. As a consequence, in many BCS-BEC crossover approaches one can encounter unphysical effects that are inherited from problems in theories of Bose gases (Reatto and Straley, 1969; Shi and Griffin, 1998). Among these are first order jumps in thermodynamic properties at T_c and violations (Haussmann and Zwerger, 2008) of the Hugenholtz-Pines constraint (Hugenholtz and Pines, 1959).

III. MICROSCOPIC THEORY OF 3D BCS-BEC CROSSOVER SUPERCONDUCTIVITY AT $T \neq 0$

Section II.D provided a reasonably complete summary of results from the current formalism. In this section we present additional details.

A. Characterizing the bosons embedded in BCS theory

Here we determine how to microscopically and quantitatively understand the noncondensed bosons of the BCS approach using slightly different language (Chen *et al.*, 2005) than that of Kadanoff and Martin. We present the theory for the s-wave case, while the application to d-wave superconductivity can be found elsewhere (Chen, 2000). We build on a centrally important observation: at any temperature in which there is a condensate, the noncondensed bosons that are in equilibrium with the condensate must have a vanishing chemical potential,

$$\mu_{\text{pair}} = 0 \quad \text{for } T \leq T_c. \tag{11}$$

This statement is equivalent to the famous Hugenholtz-Pines theorem (Hugenholtz and Pines, 1959). How do we guarantee that the pair chemical potential is zero? BCS provides us with an important temperature-dependent self-consistency condition known as the gap equation that is valid for all $T \leq T_c$. This gap equation is given by

$$0 = \frac{1}{U} + \sum_{\mathbf{k}} \frac{1 - 2f(E_{\mathbf{k}})}{2E_{\mathbf{k}}}, \tag{12}$$

where $E_{\mathbf{k}} = \sqrt{\xi_{\mathbf{k}}^2 + \Delta^2}$ and Δ is the temperature-dependent pairing gap.
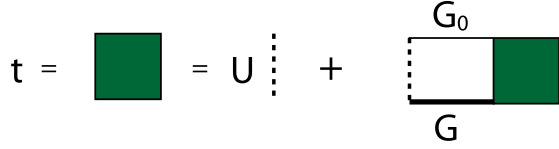
FIG. 6. Pair propagator, where U is the attractive interaction and G_0 and G are the bare and dressed fermion Green's functions, respectively, as given by Kadanoff and Martin (1961).

We argue that Eq. (12) should be incorporated in one way or another to arrive at an understanding of pair excitations. This leads us to constrain the form of the pair propagator $t(q)$ (or, more precisely, the t matrix) for the noncondensed pairs to satisfy

$$t^{-1}(q = 0) \propto \mu_{\text{pair}} = 0, \qquad T \leq T_c. \tag{13}$$

Indeed, Thouless argued that a divergence of a sum of "ladder" diagrams (within a pair propagator) is to be associated with the BCS transition temperature. Here we assert that this Thouless condition can be extended to characterize the full temperature-dependent gap equation for all $T \leq T_c$, not just the transition region. This constraint leads to a pair propagator of the form[3]

$$t^{-1}(q) = \sum_k G(k)G_0(q - k) + U^{-1}, \tag{14}$$

whose diagrammatic representation is shown in Fig. 6. In Eq. (14) $G_0(k) = (i\omega_n - \xi_{\mathbf{k}})^{-1}$ and $G(k) \equiv [G_0^{-1}(k) - \Sigma(k)]^{-1}$, corresponding to the bare and dressed fermion Green's functions, respectively, with $\Sigma(k) = -\Delta^2 G_0(-k)$. We define $k = (i\omega_n, \mathbf{k})$ and $q = (i\Omega_l, \mathbf{q})$ as two four-vectors with $\omega_n = (2n + 1)\pi T$ and $\Omega_l = 2l\pi T$, while $\sum_k$ is a shorthand notation for $T\sum_n\sum_{\mathbf{k}}$, with $\{n, l\} \in \mathbb{Z}$.

It is important in Eq. (14) to properly define the fermionic chemical potential[4] μ. In this way one avoids unphysical effects that stem from the asymmetric form of the t matrix of BCS theory involving different spin states pertaining to dressed and bare Green's functions. If care is not taken, such calculations may lead incorrectly to an artificial Fermi surface mismatch between the two spin states, and thereby to regions of unstable superconductivity in the phase diagram (Pini, Pieri, and Strinati, 2019).

Kadanoff and Martin (1961) and Patton (1971) arrived at the same conclusion concerning the presence of both dressed and bare Green's functions. As stated by Kadanoff and Martin, "This asymmetry … has led several people to surmise that the symmetrical equation … solved in the same approximation would be more accurate. This surmise is not correct… ."

---

[3]A more systematic and first principles derivation of this t matrix can be found using Eqs. (2.3), (2.4), (2.7), (2.8), (2.7′), (2.8′), and (2.10) of Kadanoff and Martin (1961).

[4]To be consistent, this requires setting $\text{Re}\Sigma(\mathbf{k}_\mu) = 0$ so that Hartree-like terms in the diagonal part of the self-energy are absorbed into the chemical potential. Here $\mathbf{k}_\mu$ is a wave vector on the Fermi surface.

B. Determining the pair mass M_{pair} and the noncondensed pair number density n_{pair} for $T \leq T_c$

The fundamental quantities that determine the transition temperature (Chen *et al.*, 2005) in Eqs. (3) and (5) require that we determine n_{pair} and M_{pair}. We argue that both of these must depend on the BCS gap Δ. In general t-matrix theories the self-energy is given by a convolution between a Green's function and the t matrix. Here this self-energy due to noncondensed pairs takes the form

$$\Sigma_{\text{PG}}(k) = \sum_{q \neq 0} t(q)G_0(q - k). \tag{15}$$

Note that the $q = 0$ component of $t(q)$ (which corresponds to the condensate) is necessarily excluded in the summation in Eq. (15). To proceed further one adopts the so-called pseudogap (PG) approximation. This was inspired originally by detailed numerical work (Maly, Jankó, and Levin, 1999a, 1999b). We also emphasize that it is appropriate at all T below T_c. It can also be applied to a restricted set of temperatures near but slightly above the transition (Maly, Jankó, and Levin, 1999a, 1999b) where $|\mu_{\text{pair}}|$ is small. Since $|\mu_{\text{pair}}| \approx 0$, $t(q)$ is strongly peaked at about $q = 0$ so that the self-energy can be approximated by

$$\Sigma_{\text{PG}}(k) \approx -\Delta^2_{\text{PG}}G_0(-k), \tag{16a}$$

with

$$\Delta^2_{\text{PG}} = -\sum_{q \neq 0} t(q), \qquad T \lesssim T_c. \tag{16b}$$

We emphasize that Eqs. (16a) and (16b) constitute the central approximation made [for numerical simplicity (Maly, Jankó, and Levin, 1999a)] in the present theoretical framework. The other crucial approximation is the adoption of Eq. (1) as the essential starting point.

We are now in a position to compute the pair mass and number density. After analytical continuation $i\Omega_l \rightarrow \Omega + i0^+$, we expand the inverse t matrix for small argument q to find

$$t(\Omega, \mathbf{q}) = \frac{Z^{-1}}{\Omega - \Omega_{\mathbf{q}} + \mu_{\text{pair}} + i\Gamma_{\Omega,\mathbf{q}}}, \tag{17}$$

where Z is a frequency- and momentum-independent proportionality coefficient; the pair mass is contained in the pair dispersion[5] $\Omega_{\mathbf{q}} = \mathbf{q}^2/2M_{\text{pair}}$; the last term in the denominator $i\Gamma_{\Omega,\mathbf{q}}$ is frequency dependent and describes the finite lifetime of the noncondensed pairs due to decay into the two-fermion continuum. Defining the propagator for the noncondensed pairs as $Zt(\Omega, \mathbf{q})$ and neglecting the generally small dissipative term $i\Gamma_{\Omega,\mathbf{q}}$, one can obtain the noncondensed pair density as

---

[5]In the quasi-2D case, one can expand the pair dispersion as $\Omega_{\mathbf{q}} = \mathbf{q}^2_\parallel/2M_{\text{pair},\parallel} + \mathbf{q}^2_\perp/2M_{\text{pair},\perp}$, where the subscripts $\parallel$ and $\perp$ denote in-plane and out-of-plane components, respectively. Away from the long-wavelength limit on a lattice, one can use a Bloch band dispersion instead of a simple parabola. An Ω^2 term may be added to the expansion of $t^{-1}(q)$ for better quantitative accuracy.

$$n_{\text{pair}} = \sum_{\mathbf{q}} b(\Omega_{\mathbf{q}}) = Z\Delta_{\text{PG}}^2, \qquad (18)$$

which is naturally temperature dependent. In Eq. (18), $b(x) = 1/(e^{x/T} - 1)$ is the Bose-Einstein distribution function.

We have asserted that the total fermionic gap is given by $\Delta^2 = \Delta_{\text{sc}}^2 + \Delta_{\text{PG}}^2$. To complete the arguments, we now show that this derives from the following two self-energy contributions [from the condensate (sc) and the noncondensate (PG)]:

$$\Sigma(k) = \sum_q t(q)G_0(-k+q) = \Sigma_{\text{sc}}(k) + \Sigma_{\text{PG}}(k). \qquad (19)$$

In Eq. (19), Σ_{sc} comes from the Dirac delta function piece of $t(q)$ at $q = 0$, i.e., $t_{\text{sc}} \equiv t(q = 0) = -(\Delta_{\text{sc}}^2/T)\delta(q)$. Using Eq. (16a), we then obtain

$$\Sigma(k) \approx -(\Delta_{\text{sc}}^2 + \Delta_{\text{PG}}^2)G_0(-k) \equiv -\Delta^2 G_0(-k). \qquad (20)$$

In this way, Eq. (6) results and we have $\Delta^2 = \Delta_{\text{sc}}^2 + \Delta_{\text{PG}}^2$.

C. Establishing the form of T_c

We approach T_c from high temperatures, where $\Delta_{\text{PG}}^2 = \Delta^2$ and $\mu_{\text{pair}} < 0$. As T decreases, μ_{pair} increases, and Eq. (18) will be satisfied under the condition $\Delta_{\text{PG}}^2 = \Delta^2$ at $T \geq T_c$. The transition temperature T_c is reached when this is no longer possible; below this temperature Δ_{PG}^2 cannot accommodate the value of Δ^2, so an additional contribution Δ_{sc}^2 is needed. This occurs when μ_{pair}, as a function of decreasing T, first reaches zero in Eq. (18), from which one recovers the following Schafroth-like expression for T_c:

$$T_c = \left(\frac{2\pi}{\mathcal{C}}\right) \frac{n_{\text{pair}}^{2/3}(T_c)}{M_{\text{pair}}(T_c)}, \qquad (21)$$

as was anticipated in Eq. (3). While it was not recognized in the original Schafroth calculations, on the right-hand side of Eq. (21) both n_{pair} and M_{pair} depend on Δ^2 and are therefore functions of T. Below T_c, Eq. (18) holds for noncondensed pairs with $\mu_{\text{pair}} = 0$ and $\Delta_{\text{PG}}^2 < \Delta^2$. Here the total pair density can be deduced to be $n_{\text{pair}}^{\text{total}} = Z\Delta^2$.

D. Alternative *t*-matrix approaches to BCS-BEC crossover

From Fig. 6 or, equivalently, Eq. (14) one can see that, within the BCS ground-state-based *t*-matrix approach to BCS-BEC crossover, an asymmetric combination of dressed (G) and bare (G_0) Green's functions enters the definition of the *t* matrix or pair propagator. As noted earlier, the connection between this combination and BCS theory was first identified by Kadanoff and Martin (1961), who used an equation of motion approach. However, in general one could contemplate other combinations of G and G_0 in defining the *t* matrix. Except for the particular combination shown in Fig. 6, the related ground states are not as well understood (Diener, Sensarma, and Randeria, 2008).

The NSR scheme is associated with two bare Green's functions. The self-consistent *t*-matrix approximation (SCTA), associated with two dressed Green's functions, was discussed by Haussmann (1993) and Haussmann *et al.* (2007) in applications to the Fermi gases, and even earlier in the context of the cuprates (Micnas *et al.*, 1995; Tchernyshyov, 1997; Allen and Tremblay, 2001). It is also known as the Luttinger-Ward formalism (Haussmann, Punk, and Zwerger, 2009) or Galitskii-Feynman theory (Šopík *et al.*, 2011). This Φ-derivable theory possesses an appealing simplicity, as it readily satisfies conservation laws. However, this *t*-matrix theory will not satisfy the equations of motion, such as those derived by Kadanoff and Martin (1961), as prescribed by the Hamiltonian.

Comparisons among these different *t*-matrix schemes have been extensively discussed in the literature (Levin *et al.*, 2010). Here we give a critical summary, noting that it is useful to first discuss the comparisons in the context of Fermi gases and then turn to the lattice case. While the differences among different schemes might seem to be technical and therefore possibly minor, they have led to significantly different qualitative physics. Among these is the fact that the transition at T_c is first order (Pieri, Pisani, and Strinati, 2004; Fukushima *et al.*, 2007; Haussmann *et al.*, 2007; Hu, Drummond, and Liu, 2007) in the standard NSR-based approaches, as well as in the SCTA scheme. This leads to unwanted features in the Fermi-gas density profiles (Perali *et al.*, 2004) and temperature dependence of the superfluid density (Fukushima *et al.*, 2007).

Serene (1989) and Sofo and Balseiro (1992) addressed other problematic aspects regarding the NSR approach. Of additional concern in the SCTA scheme is the failure to satisfy the Hugenholtz-Pines gapless condition (Haussmann and Zwerger, 2008). In this context it was also noted by Haussmann, Punk, and Zwerger (2009) that "a simple pseudogap ansatz for the spectral function (Norman *et al.*, 1998) is not consistent with our results … we do not observe a strong suppression of the spectral weight near the chemical potential." More generally there is some controversy in the Fermi-gas literature (Tchernyshyov, 1997; Morawetz, 2011; Šopík *et al.*, 2011; Zwerger, 2012) about the presence or absence of a (pseudo)gap in this SCTA approach. In the same vein, we note that the principal weakness of the BCS-Leggett approach is that it focuses on the pairing channel while embedding all Hartree-like effects in an effective chemical potential. This leads to numerical discrepancies of some significance, particularly for the unitary Fermi gas.

In the lattice case an on-site attractive Hubbard Hamiltonian provides a prototypical model for studying BCS-BEC crossover in the literature. While in many ways *t*-matrix schemes involving all fully dressed Green's functions (Deisz, Hess, and Serene, 1998; Engelbrecht, Zhao, and Nazarenko, 2002; Tamaki, Ohashi, and Miyake, 2008) would seem to be more complete, in this model the nature of the (pseudo)gap and whether it exists both above and below T_c continues to be debated in the lattice context as well (Micnas *et al.*, 1995; Tchernyshyov, 1997; Moukouri *et al.*, 2000; Allen and Tremblay, 2001; Tremblay, Kyung, and Sénéchal, 2006).

Indeed, a relatively complete study of the associated excitation spectrum for a conserving SCTA formalism showed multiple, complex excitation branches (Micnas *et al.*, 1995).

Tamaki, Ohashi, and Miyake (2008) presented comparative T_c calculations for SCTA schemes along with the NSR approach and with DMFT. Here one sees that the transition temperatures in the NSR scheme are significantly higher (particularly in the asymptotic regime at large $|U|$). This is attributed to the fact that this approach may tend to underestimate the effects of an indirect repulsion between fermion pairs. All *t*-matrix approaches, in some sense, ignore the effects of direct interpair repulsion (Micnas, Ranninger, and Robaszkiewicz, 1990), but indirect effects appear via interactions with the fermions. These observations may bear on Haussmann's observation (Haussmann, 1994) that the approach to the BEC asymptote in the Fermi-gas case should be from below and not above in a T-U phase diagram, as found by NSR.

IV. QUANTITATIVE IMPLICATIONS FOR 3D CROSSOVER SUPERCONDUCTORS

A. Two-gap physics present in BCS-BEC crossover

One should understand the necessity of having two distinct energy gaps in BCS-BEC crossover physics. These were illustrated in Fig. 4. The recognition of these two distinct gaps is an issue that bears on some of the interesting candidate materials that are claimed to exhibit BCS-BEC crossover, as we discuss in this review.

One of the central ways in which these two-gap contributions are manifested has to do with the distinction between two classes of experiments: those associated with phenomena that reflect superfluid coherence and those that reflect an excitation or pairing gap. The superfluid density n_s (Chen *et al.*, 1998; Chen, 2000) provides a useful example, as it necessarily vanishes when coherence is destroyed or, equivalently, when $\Delta_{sc} = 0$. Notably, however, it also depends on the total fermionic excitation gap Δ through the quasiparticle energy $E_{\mathbf{k}}$,

$$\frac{n_s}{m} = \frac{2}{3} \sum_{\mathbf{k}} \left(\frac{\partial \xi_{\mathbf{k}}}{\partial \mathbf{k}}\right)^2 \frac{\Delta_{sc}^2}{E_{\mathbf{k}}^2} \left[\frac{1 - 2f(E_{\mathbf{k}})}{2E_{\mathbf{k}}} + \frac{\partial f(E_{\mathbf{k}})}{\partial E_{\mathbf{k}}}\right], \quad (22)$$

which is written here for an isotropic *s*-wave superconductor in three dimensions with fermion mass m.

Similarly, it has been argued that Andreev scattering appears to measure the gap associated with the order parameter, as opposed to conventional quasiparticle tunneling, which measures the full pairing gap Δ. This has been recognized for the cuprates (Deutscher, 2005) and more recently for twisted bilayer graphene (Oh *et al.*, 2021).

We emphasize the fact that, even though the bosonic degrees of freedom may be viewed as "quasi-ideal" within this generalized BCS framework, in contrast to an ideal Bose gas, this does not compromise the existence of stable superfluidity. Superconductivity is stable in this framework, as it is to be associated with the underlying fermionic degrees of freedom.

This analysis of the superfluid density provides a general template for other experiments that reflect true long-range order in a superconductor. Its low-T behavior has often been

used to distinguish between superconductors of different pairing symmetries, such as *s*-wave versus *d*-wave superconductors. We end by noting that this intrinsic two-gap behavior appears to have no natural counterpart in other preformed-pair scenarios (such as the phase-fluctuation approach) for the pseudogap.

B. Contrasting BCS-BEC crossover in *s*- and *d*-wave superconductors

A crucial feature of BCS-BEC crossover in superconductors (in either two or three dimensions) to be emphasized throughout this review is that the canonical plots of the phase diagram (based on Fermi gases) do not capture the physics of superconductivity in the solid state. For the latter, as shown in Fig. 1(a), one finds that T_c follows a superconducting dome as a function of variable interaction strength within the fermionic regime. Thus, one should not infer, as is often the case, that for solid-state superconductors in the BEC there is a large and maximal transition temperature.

Figure 7 provides further quantitative details on the key energy scale parameters that enter BCS-BEC crossover for the *s*-wave lattice case in Fig. 1(a). Figure 7 indicates the behavior of Δ and μ at T_c in units of a characteristic electronic scale (in this case corresponding to the half bandwidth). These energies are plotted as a function of varying attractive interaction strength, normalized to the half bandwidth $W = 6t$, where t is the hopping matrix element. Also plotted is the important parameter n_{pair}, which corresponds to the number density of pairs at the onset of the transition [normalized by $n/2$, as determined from Eq. (18)].

In particular, one can glean from the plot of n_{pair} that the BEC or $\mu = 0$ transition is associated with the absence of fermions so that only pairs are present ($n_{pair} = n/2$). More generally one can view the function n_{pair} as a kind of theoretical "dial" indicating approximately where a given system is within the crossover. Tuning the dial provides access to the counterpart values of μ and Δ at T_c. When n_{pair} is
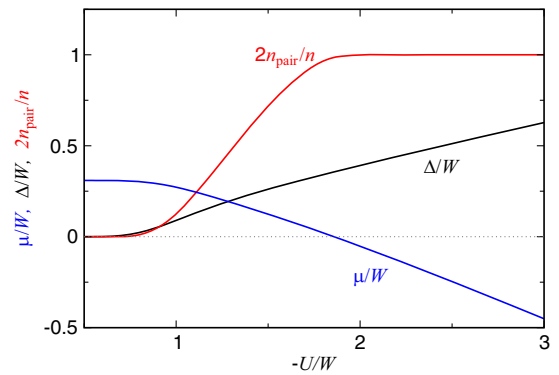

FIG. 7. Quantitative values of the parameters μ, Δ, and the number of pairs n_{pair} at T_c for the *s*-wave BCS-BEC crossover superconductor on a 3D cubic lattice in Fig. 1(a) as a function of the attractive interaction U (normalized by the half bandwidth $W = 6t$). Here the electron density is $n = 0.1$ per unit cell. The normal-state electronic energy dispersion is $\epsilon_{\mathbf{k}} = 2t(3 - \cos k_x - \cos k_y - \cos k_z)$, where the lattice constant a has been set to unity.
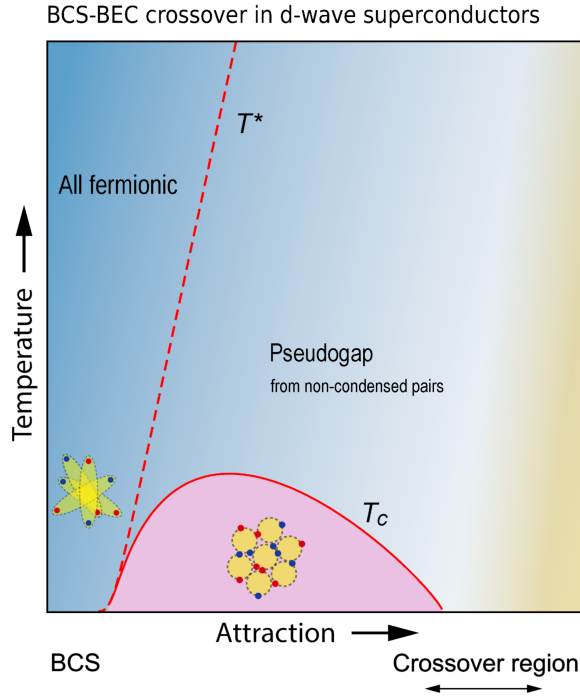
BCS-BEC crossover in d-wave superconductors

FIG. 8. BCS-BEC crossover phase diagram for a *d*-wave superconductor. This is for an attractive Hubbard-like interaction $V_{\mathbf{k},k'} = U\varphi_{\mathbf{k}}\varphi_{\mathbf{k}'}$, where the momentum-dependent function $\varphi_{\mathbf{k}}$ possesses a $d_{x^2-y^2}$ symmetry. This system (near half filling) has vanishing T_c before the onset of the BEC regime. This behavior persists down to $n \simeq 0.1$. We can compare this scenario with the schematic *s*-wave case in Fig. 1(a). For *s*-wave symmetry the BEC regime is in principle accessible up to around a quarter filling. Actual units for the vertical and horizontal axes can be found in Fig. 37, which corresponds to a slightly modified band structure that is specific to the cuprates. From Chen *et al.*, 1999.

essentially zero this corresponds to the BCS case, and when $n_{\text{pair}} \approx n/2$ one enters the BEC regime.

The crossover behavior for a *d*-wave superconductor is generally different (Chen *et al.*, 1999); some aspects are discussed in Appendix B. For definiteness, we consider here the symmetry to be of the form $d_{x^2-y^2}$, which is relevant to the cuprate superconductors. The central contrasting feature is the termination of *d*-wave superconductivity well before the BEC regime is entered. This is found at all but extremely low electron densities and derives principally from the fact that *d*-wave pairs have a more extended size. As a result, a pair-pair repulsive interaction that is always present (Micnas, Ranninger, and Robaszkiewicz, 1990) is sufficiently strong to inhibit pair hopping, and pairs become localized. Note that this happens in the fermionic regime, well away from where $\mu < 0$. Consequently, in the *d*-wave case, the BEC limit cannot generally be accessed (Chen *et al.*, 1999), as illustrated in Fig. 8.

What this implies more concretely is that the *d*-wave system undergoes a transition at moderately strong attraction, where $T_c \to 0$. Here superconductivity continuously disappears, albeit in the presence of a finite pairing gap Δ or finite T^*. This has features that are suggestive of the widely discussed "Cooper-pair insulator" (Hebard and Paalanen, 1990;
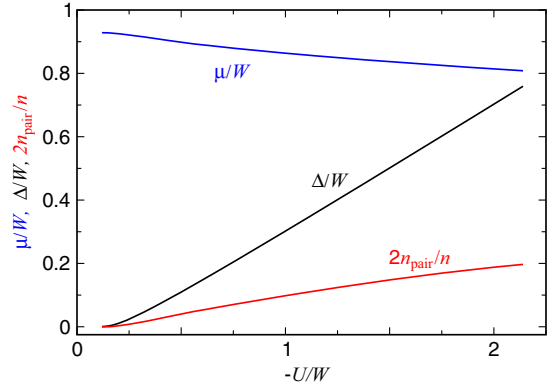

FIG. 9. Quantitative values of the parameters μ and Δ and the number density of pairs n_{pair} at T_c for the quasi-2D *d*-wave BCS-BEC crossover superconductor in Fig. 8 as a function of the attractive interaction (normalized again by the half bandwidth W). The normal-state kinetic-energy dispersion is $\epsilon_{\mathbf{k}} = (4t + 2t_z) - 2t(\cos k_x + \cos k_y) - 2t_z \cos k_z$, with $t_z/t = 0.01$. The electron density is $n = 0.85$ per unit cell.

Paalanen, Hebard, and Ruel, 1992; Hollen *et al.*, 2011) or a pair density wave alternative (Che, Wang, and Chen, 2016; Chen, Wang *et al.*, 2020; Sun and Chen, 2022; Sun *et al.*, 2022). But the form of pair localization considered here pertains to a clean system and represents a different mechanism, derived from strong intrapair attraction and strong interpair repulsion, that inhibits pair hopping. This same localization has also been observed in cases where the band filling is high in *s*-wave superconductors, as well as in 2D systems. In these instances it provides an interesting comparison but is not to be associated with strong disorder effects, which are known to drive a superconductor-insulator transition in superconducting films (Fisher, 1990; Hebard and Paalanen, 1990; Paalanen, Hebard, and Ruel, 1992; Yazdani and Kapitulnik, 1995).

Figure 9 provides more quantitative details on the characteristic energy scale parameters that enter BCS-BEC crossover for this *d*-wave lattice case (Chen *et al.*, 1999). Plotted in the figure is the behavior of Δ and μ at T_c as a function of varying attractive interaction. Also indicated is the number of pairs n_{pair} [derived from Eq. (18)] at the onset of the transition.

C. The interplay of conventional fluctuations and BCS-BEC crossover physics: Normal-state transport

The question as to how conventional superconducting fluctuations relate to BCS-BEC crossover physics continues to be raised in the literature. In this regard it is interesting to note that the treatment of preformed pairs presented here is closely related to self-consistent theories of fluctuation superconductivity. In particular, it represents a natural extension to arbitrarily strong attraction of time-dependent Ginzburg-Landau-based transport theory (Ullah and Dorsey, 1991) when the quartic terms in this free-energy expansion are treated in a self-consistent Hartree-level approximation (Patton, 1971; Ullah and Dorsey, 1991; Stajic *et al.*, 2003; Tan and Levin, 2004). This observation suggests that there is a continuous variation, associated with an enhancement of

many transport fluctuation signatures, as the coupling varies from weak to strong.

To address these issues more quantitatively, we note that dominating transport in these more strongly correlated super-conductors (Boyack *et al.*, 2018, 2019, 2021) is the fact that there are now two distinct temperature scales that control "fluctuation" effects: T_c and T^*. Transport is additionally complicated by the fact that there are two types of quasiparticles: fermions that experience the gap onset at T^*, where they thus generally become less conducting, and bosons whose presence is expected to increase conductivity at temperatures somewhat below T^*. These two types of quasiparticles are schematically represented in the upper row of Fig. 3.

The fermionic contribution has been discussed (Wulin and Levin, 2012; Wulin *et al.*, 2012) in some detail both above and below T_c. The more familiar fluctuation contributions to bosonic transport derive from the Aslamazov-Larkin (Aslamazov and Larkin, 1968) diagrams and are associated with a small pair chemical potential $\mu_{pair}(T)$ that is found in the immediate vicinity of T_c. In conventional superconductors, μ_{pair} depends only on T_c, but in the presence of more stable preformed pairs one expects that T^* will play an important role. It is at this higher temperature that the pair density vanishes; consequently, fluctuation effects are expected to have a presence even at temperatures as high as T^*.

The previous discussion leads one to conclude that, for more strongly coupled superconductors, the nature of fluctuation effects associated with T^* in transport requires that one establish the relative size of the contributions from the fermionic and bosonic channels; as we have seen, these two channels generally introduce opposite temperature dependencies in their conduction properties. Their relative size depends on their relative scattering times.

Central to this comparison is the fact that the resistivity downturn, a canonical signature of the pseudogap onset at T^*, is frequently associated with the concomitant and rather ubiquitous large normal-state resistivity. This bad-metal behavior (Gunnarsson, Calandra, and Han, 2003; Boyack *et al.*, 2021) reflects a suppressed fermionic conduction channel. Note that bad metallicity allows the bosonic conducting channel to become more prominent and leads to a boson-related downturn near T^* in the resistivity that would otherwise be obscured by gap effects in the fermionic spectrum.

We see later in the review examples of transport signatures that are viewed as indicative of the presence of BCS-BEC crossover physics. In addition to a resistivity downturn, these include enhanced diamagnetism and Nernst signatures, albeit not all uniquely pointing to a BCS-BEC crossover scenario.

D. Relation between BCS-BEC crossover and the Uemura plots

In an interesting series of papers, Uemura *et al.* (1989, 1997) used muon-spin resonance (μSR) experiments to establish a classification scheme for superconducting materials. This classification, in effect, distinguishes so-called exotic superconductors from conventional superconductors. The μSR relaxation rates in these experiments effectively measure the London penetration depth, which in turn reflects the ratio of the number of superfluid electrons n_s to their effective mass m. Notably at sufficiently low temperatures these same
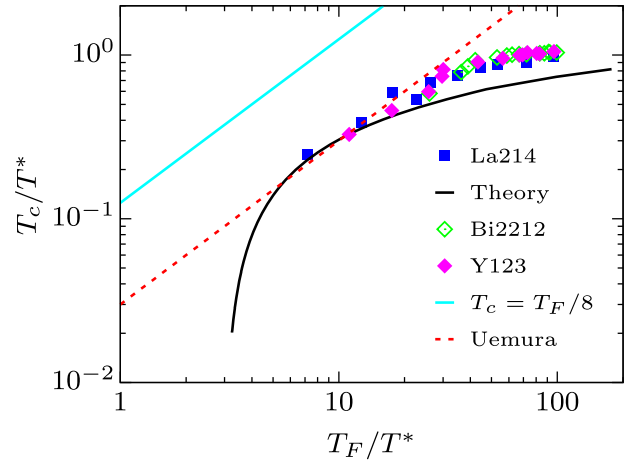

FIG. 10.   Replot of results from Tallon *et al.* (2003) suggesting a modification of the Uemura plot in which T_c depends not only on T_F but also on T^*. This replotting yields a simple, complete scaling of cuprate transition temperatures for different hole concentrations. A BCS-BEC crossover theory curve (solid black line) for the quasi-2D d-wave case (Chen *et al.*, 1999) is included. Legend: La214, La$_{2-x}$Sr$_x$CuO$_4$; Bi2212, Bi$_2$Sr$_2$CaCu$_2$O$_{8+\delta}$; Y123, Y$_{0.8}$Ca$_{0.2}$Ba$_2$Cu$_3$O$_{7-\delta}$. The dashed line (labeled Uemura) corresponds to $T_c = 0.03T_F$.

two quantities help one to determine an effective Fermi temperature.

Uemura used this analysis to suggest that "unconventional" superconductors are characterized by the proportionality $T_c \propto T_F$, where $T_F = E_F/k_B$ is the Fermi temperature. This observation, which follows from plots of the transition temperature versus muon-spin relaxation rate, has led many to believe that a dependence on a single parameter T_F is suggestive of a Bose-condensation description of exotic superconductors. Underlying this inference is the behavior of the Fermi-gas phase diagram, as shown in Fig. 1(b), where the asymptotic BEC value of T_c is given by $T_c \equiv T_{BEC} = 0.218T_F$ in three dimensions.

In Uemura's analysis it seems that there is a large number of superconductors belonging to the unconventional category, although one should not presume that all of these are associated with Bose condensation or BCS-BEC crossover. While focusing on a smaller subset of just the high-temperature superconductors, Tallon *et al.* (2003) argued for an interesting and modified version of the Uemura scheme that plots the ratio T_c/Δ_0 vs T_F, thereby introducing a second energy scale Δ_0, which reflects T^*. Figure 10 shows the resulting universal scaling of the cuprate data. The solid black line represents the d-wave BCS-BEC crossover theory at moderate band filling, as previously discussed.

Such an analysis emphasizes that for an arbitrary super-conductor, more relevant for establishing that a crossover picture is applicable is showing the presence of distinct energy scales T^* and T_c. This is a necessary although insufficient requirement. In the crossover scenario a moderately large value for Δ_0/E_F must simultaneously be present. In this way the Uemura plots have elucidated a useful classification scheme, but we stress that one should be cautious about inferring too strong a connection to BCS-BEC crossover.

Thus, in this review it is useful to show how to arrive at a more discriminating procedure that was inspired to some extent by Fig. 10. We do so here, focusing on 2D superconductors in the form of plots of Δ_0/E_F vs T^*/T_{BKT}. To begin, however, one has to have a better understanding of 2D superconductivity.

V. BCS-BEC CROSSOVER PHYSICS IN THE 2D LIMIT

A. Overview of 2D theory

In two dimensions there is no true condensation with off-diagonal long-range order. More quantitatively, in the language of a *t*-matrix approach to BCS-BEC crossover, the chemical potential for pairs μ_{pair} never reaches zero; this is effectively a consequence of the Thouless criterion, which provides a constraint on the *t* matrix. A subtle issue that is pertinent here and in the following discussion is that a fermionic system in either two or three dimensions involves in some sense noninteracting bosons, but these noninteracting pairs nevertheless support superconductivity only because they interact indirectly through their underlying fermionic nature.

In this review we build on the cold-atom literature to address the BKT phase transition (Berezinskii, 1972; Kosterlitz and Thouless, 1973). This focuses on the approach from the high-temperature side and on bosonic degrees of freedom or bosonic "quasicondensation" (associated with algebraic rather than long-range order). This transition can be equivalently described as the onset of vortex-pair binding and unbinding as in the original BKT papers; in the latter context the role of superfluid phase stiffness is more apparent.

From the quasicondensation perspective, the BKT transition occurs when the de Broglie wavelength is large and comparable to the interpair separation, similar to a BEC transition in three dimensions. More precisely, this transition arises when the temperature-dependent bosonic phase-space density reaches a critical value as was independently established in well-known papers by Fisher and Hohenberg (1988) and Popov (2001). This leads to

$$T_{BKT} = \left(\frac{2\pi}{\mathcal{D}_{pair}^{crit}}\right)\frac{n_{pair}(T_{BKT})}{M_{pair}(T_{BKT})}, \tag{23}$$

where $\mathcal{D}_{pair}^{crit}$ is the critical phase-space density, which is essentially a constant and is specified later in the review. Note that in Eq. (23) we have replaced the number density and mass of true bosons appearing in the standard expression [Eq. (5)] with their counterpart values for a composite-boson (or fermion-pair) system. In this way we see that the pair density and pair mass play a role similar to that in the 3D superfluid transition in Eq. (21).

Note that, since $n_{pair}(T)$ is temperature dependent and disappears at T^*, there is a significant difference between BKT behavior in Bose and Fermi superfluids. That is, the latter will be implicitly dependent on the two distinct temperature scales T^* and T_{BKT}. Since $T_{BKT} \leq T^*$, the physical implications of these two scales become apparent

only when one studies the BKT transition, as we do here, by approaching the transition from the normal state.

The most detailed numerical analysis of 2D atomic-gas condensates focuses on the Bose gas in the weakly interacting limit and provides (Prokof'ev and Svistunov, 2002) results for the critical value $\mathcal{D}_{pair}^{crit}$, which is given by

$$\mathcal{D}_{pair}^{crit} = \ln(C/\tilde{g}), \tag{24}$$

where $\tilde{g}$ is a dimensionless coupling constant reflecting the effective repulsive interaction between pairs. Note that the constant

$$C \approx 380 \tag{25}$$

has been established (Prokof'ev and Svistunov, 2002) from Monte Carlo studies. We also note that $\tilde{g}$ in Eq. (24) is, in principle, dependent on the bosonic pair density, as shown by Fisher and Hohenberg (1988). However, this dependence is logarithmic (and therefore weak) and can be neglected for most purposes because of the large constant C. This is a normal-state approach to the BKT transition; it is based on the phase-space density and has been supported by numerous experimental studies on atomic Bose gases (Cladé *et al.*, 2009; Tung *et al.*, 2010; José, 2013).

It is useful to compare this to the more familiar expression (Nelson and Kosterlitz, 1977) for the same T_{BKT} in a superconductor when it is approached from the low-temperature superfluid side. This provides a complementary interpretation

$$T_{BKT} = \frac{\pi}{2}\rho_s(T_{BKT}) \equiv \frac{\pi}{8}\left[\frac{n_s}{m}\right], \tag{26}$$

where one introduces the temperature-dependent superfluid phase stiffness $\rho_s(T)$, evaluated at T_{BKT}, instead of the total pair density as in Eq. (23). In Eq. (26), n_s and m are the superfluid density and the effective mass of the fermions, respectively. To connect Eq. (23) to Eq. (26), one replaces $\mathcal{D}_{pair}^{crit}$ with 4 and converts from pairs to fermions, following Halperin and Nelson (1979).

Note that there is a practical difficulty in using either of these formulations. We need phenomenological input to arrive at $\tilde{g}$ in Eq. (24). However, to apply Eq. (26) one must approximate $\rho_s(T)$ using a suitably chosen (generally mean-field) expression.[6]

B. Procedure for determining T_{BKT} in the Fermi gases

The Heidelberg cold-atom group (Murthy *et al.*, 2015) claimed that the fits for their 2D Fermi-gas data find a range of values for $\mathcal{D}_{pair}^{crit} = 4.9$–6.45 (Murthy *et al.*, 2015; Ries *et al.*, 2015). These values are close to but somewhat different than values for atomic Bose gases, where the range is about 6–10. In general, $\mathcal{D}_{pair}^{crit}$ depends on the nonuniversal boson-boson

---

[6]This excludes using the present *t*-matrix theory, more precisely the 2D counterpart of Eq. (22), where the superfluid density n_s is necessarily zero in two dimensions, which reflects the fact that simple bosonic condensation with long-range order cannot occur.
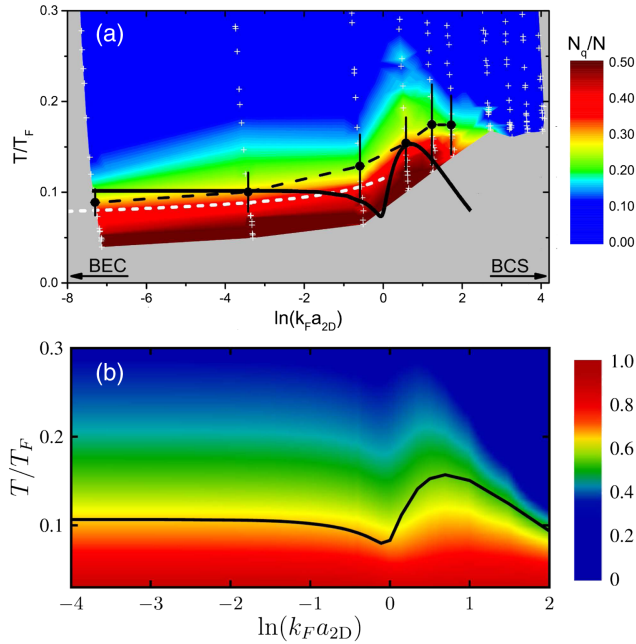
FIG. 11. (a) Comparison of theory (Wu *et al.*, 2015b) and experiment for quasicondensation phase diagram of the strongly interacting 2D Fermi gas. The color variations reflect the normalized momentum distribution of pairs at low momentum **q**, $N_{\mathbf{q}}/N$, which is used to quantify the quasicondensate fraction (Ries *et al.*, 2015). (b) Theoretical results (with a trap included) (Wu *et al.*, 2015b). The color variations similarly refer to the pair-momentum distribution at low **q**. The estimated onset of the superfluid transition, which derives from an abrupt change in $N_{\mathbf{q}}/N$ is indicated by the solid black line in both panels: the dashed line for experiment and the solid line for theory. The dashed white line in (a) is a theoretical estimate for the BKT transition from Petrov, Baranov, and Shlyapnikov (2003).

interaction strength $\tilde{g}$, about which one has no precise knowledge. A relatively small value of $\tilde{g}$ is presumed in the theoretical framework (Prokof'ev, Ruebenacker, and Svistunov, 2001; Prokof'ev and Svistunov, 2002), which represents an effectively weakly interacting gas. This would be expected in a BCS ground state of composite bosons, as the bosonic degrees of freedom enter this wave function in a quasi-ideal manner. For the analysis in this review, we adopt the value $\mathcal{D}_{\text{pair}}^{\text{crit}} = 4.9$ (Ries *et al.*, 2015), which turns out to best fit the data on Fermi gases.[7]

Based on experiments (Ries *et al.*, 2015) in Fermi gases, the 2D BKT superconducting transition is thus interpreted as a "quasicondensation" of preformed Cooper pairs. For application to 2D superconductors, more generally the BKT transition temperature is presumed to be

$$\frac{n_{\text{pair}}(T_{\text{BKT}})}{M_{\text{pair}}(T_{\text{BKT}})} = \left(\frac{4.9}{2\pi}\right) T_{\text{BKT}} \qquad (27)$$

in two dimensions.

---

[7]Note that this best fit case presumes a larger value of $\tilde{g}$ than would be expected for the weakly interacting case (Murthy *et al.*, 2015).

Experiments from the Heidelberg group (Murthy *et al.*, 2015; Ries *et al.*, 2015) on a strongly interacting 2D Fermi gas use the momentum distribution to establish the presence of a quasicondensate. This is based on magnetic-field sweeps that, through a Feshbach resonance, convert pairs to deeply bound molecules. As shown in Fig. 11(a), in this way one obtains a plot of the quasicondensation transition temperature as a function of scattering length or equivalently variable interaction strength. An overlay of theory and experiment is shown in Fig. 11(a), while Fig. 11(b) represents only the theory (Wu *et al.*, 2015b). Note that there are claims (Hazra, Verma, and Randeria, 2019) that the experimentally observed maximum, which is above $T_F/8$, could be an artifact of coupling to a third dimension in the trap, although this issue, which pertains exclusively to the 2D Fermi gas, has not been settled.

Subsequent experiments on the 2D gas (Hueck *et al.*, 2018; Sobirey *et al.*, 2021) extended these measurements on trapped gases to accommodate a box potential. An alternative methodology was used in those experiments to obtain the momentum distribution. These important studies presented more direct measurements of superfluidity, as distinct from quasicondensation of pairs. Determination of one particular critical temperature in the BEC regime yielded consistency with the experiments of the Heidelberg group as a check.

C. Quantitative description of BCS-BEC crossover in two dimensions and comparison with three dimensions

Equation (27) is adopted along with the results of Sec. III.B for n_{pair} and M_{pair}, as these characterize T_{BKT} and other features of 2D superconductors. Plotted in Fig. 12 is a comparison of transition temperatures, pairing-onset temperatures, pair size (Leggett, 2012), gap size, and coherence length in both two and three dimensions for the *s*-wave case. In Fig. 12(a) one sees the presence of a domelike structure reflecting BCS-BEC crossover in the solid state, which should be evident for T_c or T_{BKT}. This dome is well within the fermionic regime, where $\mu > 0$. The transition to the BEC regime with negative μ is evident here as a shoulder in each of the transition temperature curves. There has been some emphasis on bounds on the magnitude of the highest transition temperature in these 2D systems (Hazra, Verma, and Randeria, 2019), although we caution that in a lattice system these are less indicative of the BEC limit, as the maximum is found in the fermionic regime.

The inset of Fig. 12(a) quantifies the important effect of two dimensionality presented in Fig. 2. This inset, representing moderately low filling $n = 0.1$ per unit cell, shows that the deviation from BCS behavior (associated with T^*/T_c substantially above 1.0) occurs at significantly smaller attraction for 2D than for 3D superconductors.

We turn now to Figs. 12(b) and 12(c), which are the basis for more experimentally relevant studies. The main plots in those two panels represent a natural extension of the Tallon-Uemura scaling (Tallon *et al.*, 2003) in Fig. 10, but for the case of *s*-wave pairing in both two and three dimensions. They show that the ratio of the two distinct temperature scales T^*/T_c or T^*/T_{BKT} (which are in principle measurable) is correlated with the magnitude of the $T \approx 0$ value of Δ/E_F (which is also measurable).
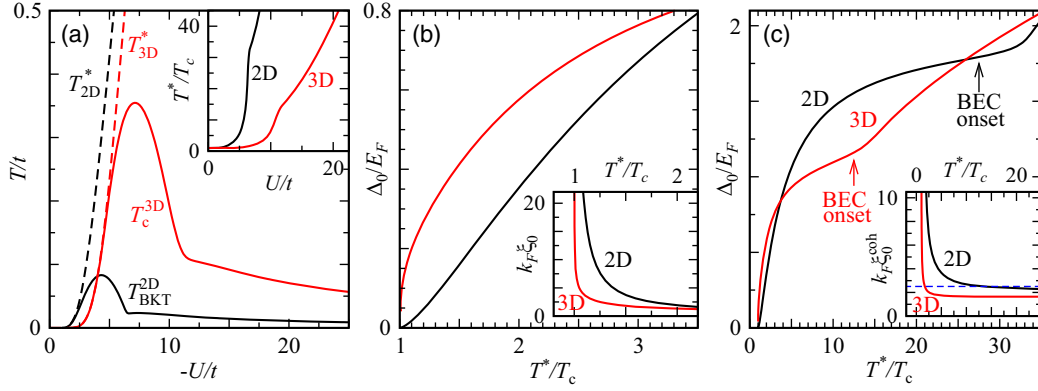
FIG. 12.   Detailed comparison of 2D and 3D transition temperatures, as well as other properties in the BCS-BEC crossover scenario for a tight-binding s-wave superconductor at a low density $n = 0.1$. (a) Transition (T_c or T_{BKT}) and pairing-onset temperatures (T^*) as a function of $-U/t$, the strength of the attractive interaction in units of the hopping matrix element t. The vertical axis in the inset quantifies the degree of departure from strict BCS (through the difference between T^*/T_c and unity). (b) Characteristic magnitude of Δ_0/E_F in two and three dimensions on a normalized scale. Inset: pair size ξ_0. (c) Extended view of the results in (b). Indicated here are the high critical values of T^*/T_c at which the system crosses over to a BEC. Inset: the behavior of the superconducting coherence length ξ_0^{coh}, in contrast to the pair size ξ_0. The former reaches a finite saturation value in the BEC regime, while the latter continuously decreases toward zero.

The inset in Fig. 12(b) shows how the zero-temperature pair size ξ_0 varies as the system crosses out of the BCS regime. Representing this crossover in the figure is T^*/T_c, which is chosen as the horizontal axis. The pair size is a reasonably good indicator of when the system is promoted out of the BCS regime. However, it can be inferred from Fig. 12(c) (where the BEC transitions are marked) that it does not display features at the onset of the BEC; rather, the pair size decreases continuously toward zero as this limit is approached. Note that in two dimensions the pair sizes for equivalent T^*/T_c are significantly larger than in the 3D case.

Finally, we emphasize that the pair size (which is less accessible experimentally) and the coherence length represent important but distinct length scales. The "bare" GL coherence length can be most readily obtained experimentally from the measured slope of the upper critical field H_{c2} versus the temperature T plot

$$\frac{dH_{c2}}{dT}\bigg|_{T=T_c} = -\frac{\Phi_0}{2\pi(\xi_0^{coh})^2 T_c}, \qquad \text{with } \Phi_0 = \frac{hc}{|2e|},$$

where $h = 2\pi\hbar$. Here the slope is evaluated at the zero field T_c. The parameter ξ_0^{coh} satisfies (Boyack *et al.*, 2018; Boyack *et al.*, 2019)

$$\xi_0^{coh} = \frac{\hbar}{\sqrt{2M_{pair}(k_B T_c)}}. \qquad (28)$$

This quantity times the Fermi wave vector is plotted in the inset in Fig. 12(c). From an experimental point of view there may be some advantage to measuring and evaluating ξ_0^{coh} in a somewhat different way, just above T_c in the normal state (Suzuki and Hikita, 1991) as here one avoids the challenging determination of $T_c(H)$, which corresponds to a magnetic-field broadened transition.

The coherence length has a distinct physical interpretation when we make use of the expressions for the transition temperatures in Eqs. (3) and (23). We define k_F in terms of the free and isotropic electron dispersion such that $k_F \equiv (3\pi^2 n)^{1/3}$ and $(2\pi n)^{1/2}$ in three and two dimensions, respectively, where we use the same symbol n to refer to the appropriate fermion number density. It follows that $k_F\xi_0^{coh}$ evaluated near the transition temperature depends only on the normalized pair density n_{pair}/n. This leads to

$$k_F\xi_0^{coh} = 1.6(n/n_{pair})^{1/2} \qquad (29)$$

and

$$k_F\xi_0^{coh} = 1.2(n/n_{pair})^{1/3} \qquad (30)$$

in two and three dimensions, respectively.

We note that Eqs. (29) and (30) are relatively easy to understand physically. The coherence length is a length scale representing the effective separation between pairs. Not surprisingly for weakly interacting pairs, it relates only to their density. This is distinct from the pair size. In BCS theory there are almost no pairs present at T_c, and the length that represents their average separation is necessarily long. As pairing becomes stronger more pairs form and their separation becomes shorter. On a lattice, in the BEC regime their separation is bounded from below by the characteristic lattice spacing and ξ_0^{coh} approaches an asymptote set by the interparticle distance as the system varies from BCS to BEC.

From plots of n_{pair}/n such as those in Fig. 7, one sees that $k_F\xi_0^{coh}$ allows a useful and direct monitoring of the location of a system between the BCS and BEC limits. Notably $k_F\xi_0^{coh}$ reaches a finite lower bound at the onset of the BEC, given by $k_F\xi_0^{coh} \approx 2.2$ in two dimensions and 1.5 in three dimensions (for the case of s-wave superconductors). The fact that these saturation numbers are of order unity is consistent with what has been anticipated by the experimental community (Park *et al.*, 2021).

We end this section with a discussion of Fig. 12(c), which presents an enlarged view of the main figure in Fig. 12(b). This provides information about where to expect the onset of the BEC. The BEC regime appears to be associated with large values of T^*/T_c. In this way, one might expect the BEC limit to be inaccessible.

D. Low carrier density in BCS-BEC crossover

In this section we clarify what one should expect when the carrier density is dramatically reduced in a lattice superconductor. For definiteness we consider only two-dimensional systems here and presume that "low density" corresponds well below quarter-filled bands, say, $n < 0.1$.

The notion that low carrier density promotes a system out of the BCS regime dates back to Eagles (1969). Indeed, in the literature it has been stressed (Kanigel *et al.*, 2008) that when the band is nearly empty it requires only a small change in the attractive interaction to push the fermionic chemical potential below the conduction band bottom; hence, the BEC regime is more accessible at low n.

What is not clear is whether or not low n alone can increase the magnitude of T_c (or T_{BKT}). Also of interest is determining whether or not at low densities the nature of the underlying lattice dispersion becomes irrelevant. If so, this would mean that the low-density system could be treated as a Fermi gas.

In the phase-fluctuation approach of Sec. II.C, low density plays a dominant role (Emery and Kivelson, 1995). While this scenario has been developed primarily for the cuprates, it can be considered in a broader context, much as the BCS-BEC crossover scenario is viewed as more generally applicable. Indeed, one might wonder whether the two scenarios converge in the low-carrier-density limit. We find that they do not.

In the phase-fluctuation scenario it is emphasized that low carrier density is associated with both poor screening and small phase stiffness or low superfluid density. Small phase stiffness, in turn, means that classical phase fluctuations of the superconducting order parameter become more prominent. These fluctuations necessarily lead to a more extensive (in temperature) "critical regime."

To address to what extent this scenario is to be distinguished from the low-carrier-density limit in BCS-BEC crossover, it is useful to determine what the implications for other properties are: namely, the size of the transition temperature and the coherence length along with Δ_0/E_F. Figures 13 and 14 address these questions.

Figure 13(a) presents a plot of T^*/T_{BKT} as a function of the pairing interaction normalized to half of the normal-state bandwidth for a range of different low densities. This figure is in many ways similar to the inset of Fig. 12(a). It shows that low carrier density does indeed promote the system out of the BCS limit, where $T^* \equiv T_{BKT}$. One can determine from the small kinks in the figure where the Bose-condensation regime sets in. It is evident that, as expected, low density makes this BEC regime more accessible, as the BEC onset occurs at a smaller attraction strength.

An important message is contained in Fig. 13(b), namely, Δ_0/E_F remains comparably large at low and relatively high densities for the same T^*/T_{BKT}. Thus, pairing remains strong and, because of the large size of Δ_0/E_F (and the small size of
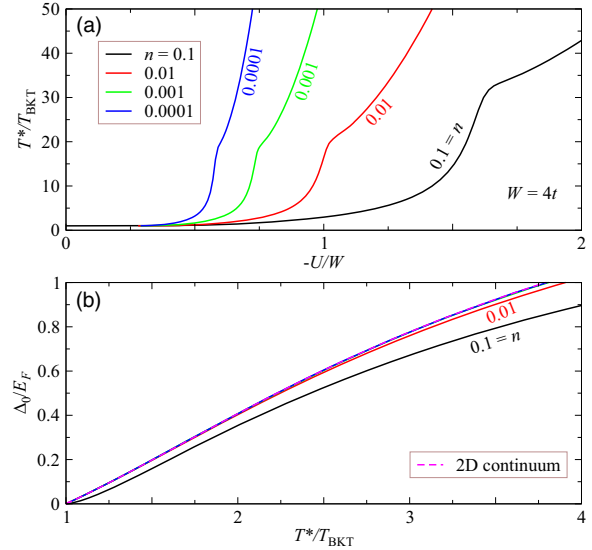

FIG. 13. (a) Plots of T^*/T_{BKT} for an *s*-wave superconductor on a square lattice at different low electron filling levels n, as labeled. The normal-state band dispersion is $\epsilon_{\mathbf{k}} = 4t - 2t(\cos k_x + \cos k_y)$, with t the hopping integral. $W = 4t$ is half of the bandwidth. Low density more readily promotes a given superconductor out of the strict BCS limit (where the ratio T^*/T_c is unity). (b) Ratio of the zero-temperature gap to E_F (i.e., Δ_0/E_F) vs T^*/T_{BKT} for different n. This panel indicates that at extremely low densities and as long as μ/E_F is neither too small nor negative, Δ_0/E_F plotted here is equivalent to the values obtained for a Fermi gas. The sizable Δ_0/E_F is indicative of BCS-BEC crossover.

$k_F\xi_0^{coh}$, which is not shown), even in the low-carrier-density limit it should be possible to distinguish BCS-BEC crossover from a phase-fluctuation scenario. We emphasize, however, that the phase-fluctuation approach does not address fermionic degrees of freedom; hence, strictly speaking, the pairing gap is irrelevant.

Figure 14 presents a plot of the normalized transition temperature T_{BKT}/W as a function of normalized interaction strength for variable density. One sees that all curves assume a fairly universal shape, but there is a dramatic reduction in the size of the transition temperature as the density is decreased. One can glean from these observations a notable trend. In the cases both of changing dimensionality from three to two and of changing carrier density from moderate to low, it follows that the superconductor is more readily promoted out of the strict BCS regime. But at the same time the transition temperatures are significantly reduced.

Another important observation from Fig. 14 is that the effect of the underlying lattice structure is always present in the BEC regime of the T_{BKT} phase diagram (Chen, 2012). In particular, the $T_{BKT} \sim t^2/|U|$ asymptote at large $|U|$ persists all the way to the zero carrier density limit, so a Fermi-gas description of the phase diagram is not applicable. At the same time, Fig. 13(b) indicates that Δ_0/E_F approaches its counterpart value for a Fermi gas. This occurs at extremely low densities but still in the BCS-BEC crossover regime, where the strength of $|U|$ is such that the fermionic chemical potential μ remains positive.
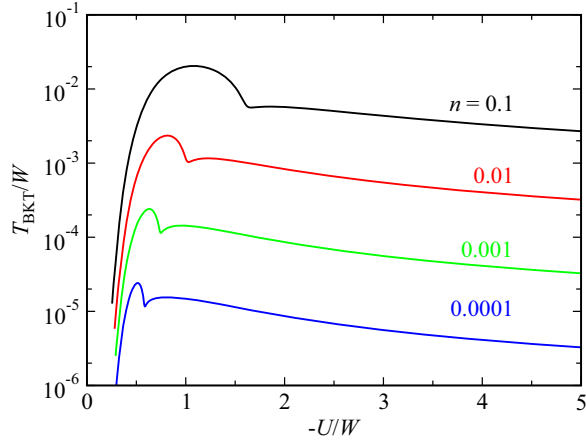
FIG. 14. T_{BKT} as a function of U on a semilog scale for variable carrier density, showing a nearly universal shape but with a dramatically decreasing magnitude of the transition temperature. The model and dispersion are the same as in Fig. 13. The small dips displayed are associated with the crossover to the BEC regime, after which the canonical $t^2/|U|$ dependence is found for the transition temperature. This dependence is a lattice effect, which persists even in the zero carrier density limit. W is half the bandwidth.

The small size of T_{BKT} found here for BCS-BEC crossover at low density should not be surprising from the perspective of the phase-fluctuation scenario, as the transition temperature, even in 3D, is governed by the small superfluid density. But it is interesting to note that there are instances in the literature when a decreasing carrier density is found to be associated with an increase in the transition temperatures (Nakagawa *et al.*, 2021). This would seem to require that the pairing mechanism is assisted by lowering density. Although this is highly speculative, one might suspect that when this occurs Coulomb interactions are driving the pairing and not undermining it.
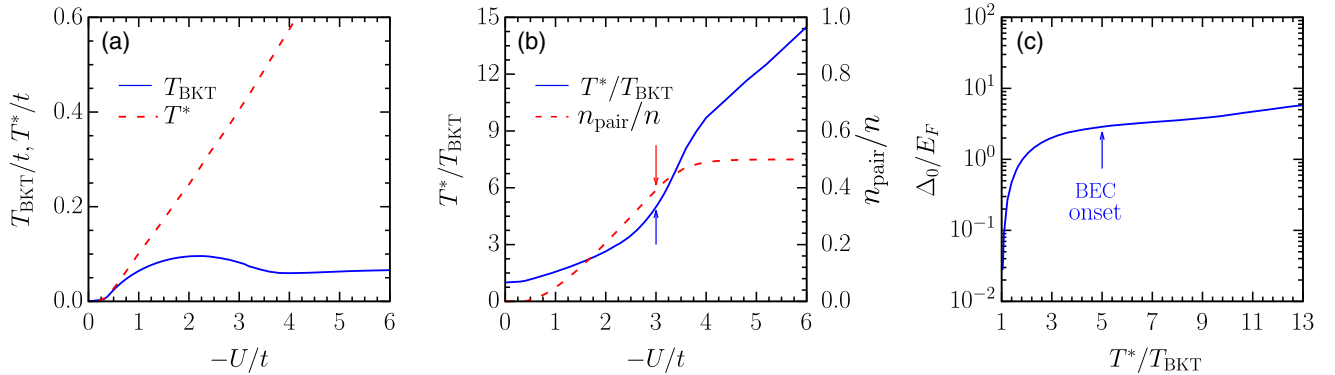
E. Topology and quantum geometry in BCS-BEC crossover

In this review, we see that current experimental candidates for BCS-BEC crossover tend to have values of T^*/T_c of the order of 2 or 3, and corresponding values of Δ_0/E_{F} of the order of 0.5. From Fig. 12(c), one can infer that these are not likely to be in the BEC regime. There is, however, an exception having to do with flat-band, topological systems. These may be relevant to the recent discovery of 2D superconductivity in MATBG and MATTG, where there are claims that these flat-band systems are somewhere between BCS and BEC (MATBG) or even beyond, within the BEC regime (MATTG) (Cao *et al.*, 2018; Park *et al.*, 2021; Kim *et al.*, 2022).

Experimentally when twist angles in these graphene systems are associated with extremely flat bands, this seems to correlate with the highest transition temperatures. There is, however, a subtle and important feature here. In flat-band superconductors, pair hopping, like single-particle hopping, is also suppressed (Peotta and Törmä, 2015; Wang *et al.*, 2020; Törmä, Peotta, and Bernevig, 2022). As a consequence, the pair mass M_{pair} becomes large and the superfluid stiffness is small. This would lead to a vanishing T_{BKT} in the extremely flat-band limit, were it not for multiband (or multiorbital) effects. Moreover, it has been emphasized (Peotta and Törmä, 2015) that the latter interband contributions (which work to decrease the pair mass) can be amplified in the presence of nontrivial normal-state band topology. This occurs through so-called quantum geometric effects.

Such multiband effects have been incorporated into a 2D s-wave BCS-BEC crossover framework (Wang *et al.*, 2020) where a phase diagram with the usual superconducting dome is found, as shown in Fig. 15(a). The model topological Hamiltonian yields two bands, whose conduction bandwidth is much smaller than the interband energy separation. The calculated phase diagram resembles that obtained from Monte Carlo results using the same model Hamiltonian (Hofmann, Berg, and Chowdhury, 2020).

FIG. 15. Flat-band and quantum geometric effects in the BCS-BEC crossover theory showing (a) T_{BKT} and T^* for a 2D topological band structure. (b) Plot of T^*/T_{BKT} as well as the number of pairs as a function of attractive interaction strength. The BEC onset, determined from $\mu(T=0) = 0$, is indicated by arrows. (c) Plots analogous to Fig. 12(c), but here the BEC appears with a similar Δ_0/E_{F} and considerably smaller T^*/T_{BKT}. T^*/T_{BKT} is reduced by quantum geometric effects that substantially increase T_{BKT} without affecting T^*. This tight-binding band structure for a square lattice (with t the nearest-neighbor hopping) leads to two energy bands whose conduction bandwidth is approximately 0.2 times the interband separation. Here $n = 0.3$ is the electron density per square lattice site. From Wang *et al.*, 2020.

Note that this phase diagram can be used to extract the ratio T^*/T_{BKT} along with the number of bosons n_{pair}/n, as shown in Fig. 15(b); both of these variables are plotted as a function of renormalized interaction strength. The quantity n_{pair} provides a ready indication of where the BEC sets in, as here n_{pair} first reaches $n/2$.

At the transition point to the BEC regime [indicated by the arrows in Fig. 15(b)], the interaction strength U is on the order of the entire conduction bandwidth. Correspondingly $\Delta_0/E_F \sim 3$, as shown in Fig. 15(c), which is not unlike the single-band result in Fig. 12(c). However, because of quantum geometry, T_{BKT} is substantially enhanced by interband effects while T^* is almost unaffected, leading to a smaller and physically more accessible value of $T^*/T_{BKT} \sim 5$. This behavior is summarized in Fig. 15(c), where the BEC onset point is indicated by the arrow. This provides a counterpart plot of Fig. 12(c), but here for a multiband, topological case. We note that the value of Δ_0/E_F at the BEC onset is nonuniversal. For a topological band structure with an extremely flat conduction band (Wang *et al.*, 2020), Δ_0/E_F can be as large as 30.

This contrast leads us to the conclusion that, in the presence of flat bands and nontrivial band topology, a BEC phase can potentially become more accessible, as it leads to a moderate size for T^*/T_{BKT}. We emphasize that these effects derive from the participation of more than one band in the superconductivity and note for completeness that there are other, rather different approaches in the literature that also treat BCS-BEC crossover phenomena in multiband systems both analytically (Chubukov, Eremin, and Efremov, 2016; Tajima, Pieri, and Perali, 2021) and numerically (Loh *et al.*, 2016).

VI. STRONGLY DISORDERED CONVENTIONAL FILMS: TWO ENERGY SCALES AND A PSEUDOGAP

We return to our discussion of Fig. 12(b), noting that it presents a unique signature of 2D pseudogap effects associated with a strong-pairing mechanism. It may be surprising, but strong disorder can lead to similar pseudogap effects in 2D superconducting films (Sacépé *et al.*, 2010). However, the parameters governing these dirty thin films are very different from those indicated in Fig. 12(b). In understanding the origin of this other pseudogap, it is important to recall that 2D superconductors have a propensity for manifesting a separation of the two energy scales T^* and T_{BKT}, which can be thought of as corresponding to the onset temperatures for amplitude and phase coherence, respectively. As an important signature, those conventional superconducting films in which the two temperature scales are well separated due to disorder (Sacépé *et al.*, 2010; Zhao *et al.*, 2013) will have rather small values of Δ_0/E_F.

While the distinctions between the two scenarios for a pseudogap (strong pairing and strong disorder) should be obvious, a number of phenomenological similarities are striking. Most notable are the reported observations of charge $2e$ pairs (Božović and Levy, 2020; Bastiaans *et al.*, 2021), the contrasting behavior of Andreev and conventional tunneling (Dubouchet *et al.*, 2019; Oh *et al.*, 2021), and the observations of boson or pair localization (Chen *et al.*, 1999; Hollen *et al.*, 2011).
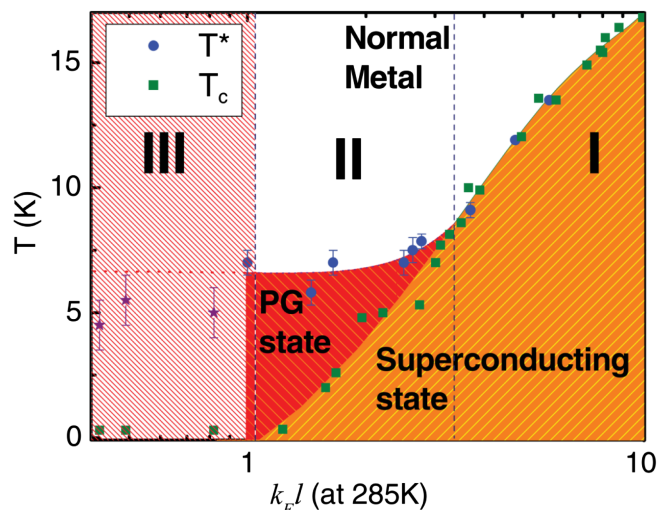

FIG. 16. Experimental temperature scales as a function of mean free path $k_F l$ in disordered NbN films (Chand *et al.*, 2012). The value of $k_F l$ is determined from resistance and Hall-coefficient measurements at $T = 285$ K. With increasing disorder or sufficiently small $k_F l$ a pseudogap (PG) phase appears, which is associated with $T^* \neq T_c$ in region II, while in region III T_c is 0 although pairing likely persists in this insulating phase.

The behavior found rather generically for a highly disordered 2D superconductor is illustrated in Fig. 16, which represents an experimentally determined phase diagram (Chand *et al.*, 2012) with temperature on the vertical axis and disorder measured through $k_F l$ on the horizontal axis. Here l is the electron mean free path. In Fig. 16, the superconducting state is shown in orange, the pseudogap state in red, and the normal-state metal in white. Also indicated are the temperatures T^* and $T_c = T_{BKT}$.

There are three demarcated regions in Fig. 16. At small disorder (region I) a pseudogap is absent and $T^* \approx T_c$, while as disorder increases (region II) T^* separates from T_c and is relatively independent of the disorder strength, whereas the transition temperature (which is more sensitive to the undermining of coherence) rapidly decreases. Finally, in region III T_c vanishes although there are indications that pairing persists. The two temperatures become distinct at a critical value of $k_F l$.

These experiments on NbN are reasonably generic, and similar observations have been made for TiN and InO$_x$ as well, where Sacépé *et al.* (2010) claimed that a pseudogap appears to be present, reflecting the existence of paired electrons above T_{BKT}. This pseudogap is found to be continuously and directly transformed into a superconducting gap below the transition.

An interesting set of parallel experiments (Zhao *et al.*, 2013) shown in Fig. 17 was performed on Pb films by a group at Tsinghua University that determined the experimental phase diagram obtained by studying crystalline and atomically flat Pb films, now as a function of variable thickness. In Fig. 17, temperature appears on the vertical axis and film thickness on the horizontal axis. The superconducting state is shown in green, the "fluctuating" or pseudogap state is depicted in blue (where nonsuperconducting Cooper pairs are said to exist), and the normal-state metal is shown in yellow. The solid circles represent superconducting or phase-coherent order, as
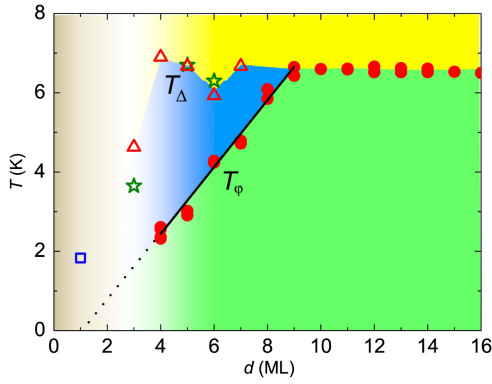
FIG. 17. Experimental behavior of characteristic temperatures $T^* \equiv T_\Delta$ and $T_\varphi \equiv T_{\mathrm{BKT}}$ as a function of the thickness d of Pb films. A more extensive analysis of the resistivity (see the text) suggests that the pseudogap effects, evident here and in Fig. 16, are likely to be associated with high disorder rather than strong-pairing correlations. ML, monolayer. From Zhao *et al.*, 2013.

determined by transport with an onset at $T_\varphi \equiv T_{\mathrm{BKT}}$; the open symbols represent the pairing transition ($T_\Delta \equiv T^*$), which is established by tunneling spectroscopy.

From Fig. 17 one can infer that the pairing temperature remains nearly constant with variable thickness, while the coherence temperature is strongly depressed. This appears to suggest that disorder may be playing a role,[8] as supported by the sheet resistance data measured by Zhao *et al.* (2013).

It is reasonably well established that T_{BKT} generally decreases with decreasing thickness in 2D films (Khestanova *et al.*, 2018), although there is no consensus on the extent to which disorder is the only relevant mechanism. The central point is that pairs form at higher temperatures than those at which they exhibit superfluidity. Equivalently, at T_φ, while phase coherence is destroyed, the superconducting gap remains nonzero. Note that for Pb the two characteristic temperatures merge in the 3D regime, as is the hallmark of a "conventional" weak-coupling bulk superconductor.

A key finding of the Tsinghua group (Zhao *et al.*, 2013) pertains to the voltage-current (V-I) characteristics, which provide an alternative method for deducing the pairing-onset temperature T^*. We emphasize that this shortcut procedure should be applicable to all 2D superconductors. More precisely, Zhao *et al.* (2013) showed that V-I plots of this type can be used to simultaneously measure the two important energy scales T^* and T_{BKT}. This is illustrated in Fig. 18, where voltage-current plots are presented for a range of different temperatures in a specific Pb thin film.

More specifically, it is well known (Halperin and Nelson, 1979) that estimates based on V-I curves allow one to determine the BKT transition, which occurs when the

---

[8]Since T^* essentially represents a mean-field transition temperature of an s-wave superconductor, this should satisfy Anderson's theorem (Anderson, 1959) of disordered superconductivity; T^* is thus expected to remain fairly robust in the presence of weak disorder that does not break time-reversal symmetry provided that the effective pairing interaction is not strongly affected by localization effects.
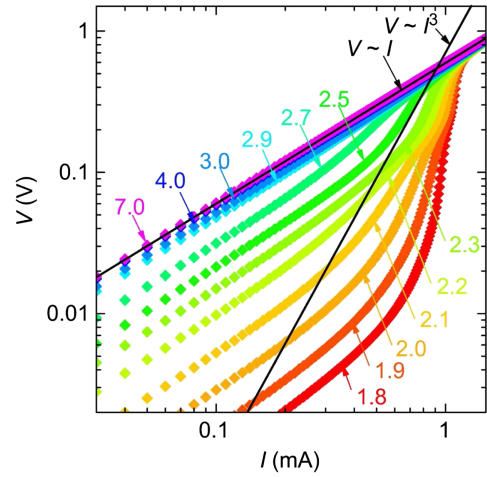

FIG. 18. V-I isotherms on a log-log plot associated with the Pb films in the Fig. 17. Each curve is labeled with its temperature (in kelvins), and a straightforward analysis identifies T_{BKT} with the $V \propto I^3$ black line. One sees that the V-I characteristics display a continuous evolution toward Ohmic behavior as the temperature is raised to the pairing-onset temperature T^*, here identified as 7 K (the $V \sim I$ black line) for a Pb film of a particular fixed thickness. From Zhao *et al.*, 2013.

condition $V \propto I^\alpha$ is satisfied with a particular value of $\alpha = 3$. Zhao *et al.* (2013) pointed out that one can also obtain the pairing-onset temperature T^* from V-I plots. This is associated with the recovery of fully Ohmic behavior shown in Fig. 18 by the $V \propto I$ black line.

While this observation could seem intuitively obvious, Zhao *et al.* (2013) made the last point more convincing by accompanying their analysis with more direct measurements of the pairing gap through scanning tunneling microscopy (STM) experiments, which yield $\Delta(T)$ and hence T^*. We note that one should take care in establishing the "Ohmic recovery" temperature, as it involves the behavior of the entire V-I curve for an extended range of I above the critical current.

VII. APPLICATION OF BCS-BEC CROSSOVER IN THE LITERATURE (BEYOND FERMI GASES)

In this section we present summaries of experimental observations concerning candidate systems for BCS-BEC crossover. We show here that the majority of the candidates appear to be consistent with this scenario, as they possess all or most of the first three discriminating properties listed in Sec. II.A. These correspond to (i) the observation of large Δ_0/E_{F}, (ii) the presence of a normal-state pseudogap such that T^*/T_{c} is significantly above 1.0, and (iii) a moderately short coherence length $k_{\mathrm{F}}\xi_0^{\mathrm{coh}}$. Also reported in a few cases is the observation of enhanced superconducting fluctuation-like behavior in the normal state, particularly in the response to a magnetic field (Li *et al.*, 2010; Proust and Taillefer, 2019).

Notably, however, what is missing in a number of cases [particularly for the organic superconductors (Suzuki *et al.*, 2022) and the two twisted magic-angle graphene systems] is information about how the temperature scale T^* varies across their respective T_{c} domes. We note that in strictly 2D systems

this appears to be reasonably accessible should there be future measurements of the *V-I* characteristics. This capability was discussed in Sec. VI based on the Ohmic recovery temperature, which effectively yields T^*.

Overall, what seems to be nearly universally observed in these candidate BCS-BEC crossover superconductors is a large magnitude for Δ_0/E_F and a relatively small size for the GL coherence length $k_F\xi_0^{\mathrm{coh}}$. The focus on the last quantity serves to emphasize the contrast with Fermi gases, where this coherence length is not as readily accessible.

Connections to more specific aspects of BCS-BEC crossover theory are presented in Sec. IX via a summary figure (Fig. 36) for all the candidate materials in two dimensions. Unlike Fermi gases, where the magnitude of the attractive (Hubbard-like) interaction can be quantified, here one has to circumvent this parameter. As we later show, in Fig. 36 we address correlations of T^*/T_{BKT} and Δ_0/E_F instead. A related plot that focuses on commonalities between the graphene and cuprate families is Fig. 40. While in Fig. 36 a simple tight-binding band structure is used for all candidate materials, we argue that the specific details of the band structure are viewed as less important than distinguishing between *s*- and *d*-wave pairing symmetries, or 2D and 3D systems or addressing some of the more universal features of the crossover.

A. BCS-BEC crossover in 2D organic conductors

Over the years there have been observations that a class of quasi-2D organic superconductors based on the bis(ethylene-dithio)tetrathiafulvalene (BEDT-TTF) molecule, of the type κ-$(\mathrm{BEDT\text{-}TTF})_2 X$, might have something in common with the high-temperature superconductors (McKenzie, 1997). Here X is an inorganic anion and κ denotes the specific packing arrangement in the crystal. The basic unit here is a dimer consisting of two BEDT-TTF molecules stacked on top of each another. Upon binding with the anion, the dimer provides one electron to the anion leaving behind a mobile hole.

The similarity with the cuprates has been based on the observations (Oike *et al.*, 2017; Imajo *et al.*, 2021; Matsumura *et al.*, 2022) of competing metallic, insulating, superconducting, and antiferromagnetic states in the phase diagram, which is generally plotted as a function of pressure. As the pressure decreases (presumably in analogy to a decrease in doping in the cuprates), the properties of the molecular conductor (and its superconducting phase) deviate progressively from those of a typical metal (and BCS superconductor). Conversely, with an increase in pressure the behavior appears more conventional.

Of interest is the case where X involves HgBr [specifically, one studies κ-$(\mathrm{BEDT\text{-}TTF})_4\mathrm{Hg}_{2.89}\mathrm{Br}_8$] in the "parent" compound of these systems, which seems to exhibit features of a quantum spin liquid (Powell and McKenzie, 2011; Suzuki *et al.*, 2022). This quantum spin liquid is associated with a frustrated spin configuration, often modeled theoretically via a triangular Hubbard lattice (Yokoyama, Ogata, and Tanaka, 2006). Notably (Oike *et al.*, 2017; Imajo *et al.*, 2021; Matsumura *et al.*, 2022) with varying pressure this particular class of organic superconductors exhibits possible $d_{x^2-y^2}$ ordering and transition temperatures as high as 7–10 K, with suggestions of pseudogap behavior for $T > T_c$. One also sees an unexpectedly large slope for dH_{c2}/dT near T_c in fields

both in parallel with and perpendicular to the two-dimensional conducting layers. There is also a wide region of fluctuating superconductivity above T_c, along with a large superconducting energy gap.

What is particularly relevant in this review is that recent studies have more quantitatively addressed pressure variations in κ-$(\mathrm{BEDT\text{-}TTF})_4\mathrm{Hg}_{2.89}\mathrm{Br}_8$ in the context of BEC-BCS crossover. It is presumed that pressure works to enhance the itinerant nature of electrons through the increase of the transfer integral t between molecular orbitals, leading to a pressure-dependent band structure. Thus, one can imagine in the context of Fig. 12 that variable pressure could cause a variation in T_c through the generic phase diagram parameter $|U|/t$; as t increases, the dimensionless interaction strength decreases, thus moving the system closer to the BCS regime.

Indeed, this is what is observed in Fig. 19. Of considerable interest in Fig. 19 are the combined plots of the in-plane coherence length $k_F\xi_0^{\mathrm{coh}}$ and the transition temperature. If we implicitly make the assumption that pressure scales inversely with $|U|/t$, this provides a pedagogical and rather powerful representation of BEC-BCS crossover. Figure 19 appears to be consistent with the various plots of the T_c dome and the behavior of the coherence length shown in Fig. 12. Notably, for a *d*-wave gap symmetry, the smallest value reached by $k_F\xi_0^{\mathrm{coh}}$ will be significantly larger than for *s*-wave symmetry since the BEC limit is generally not reachable for these extended-size pairs; see also Fig. 8.
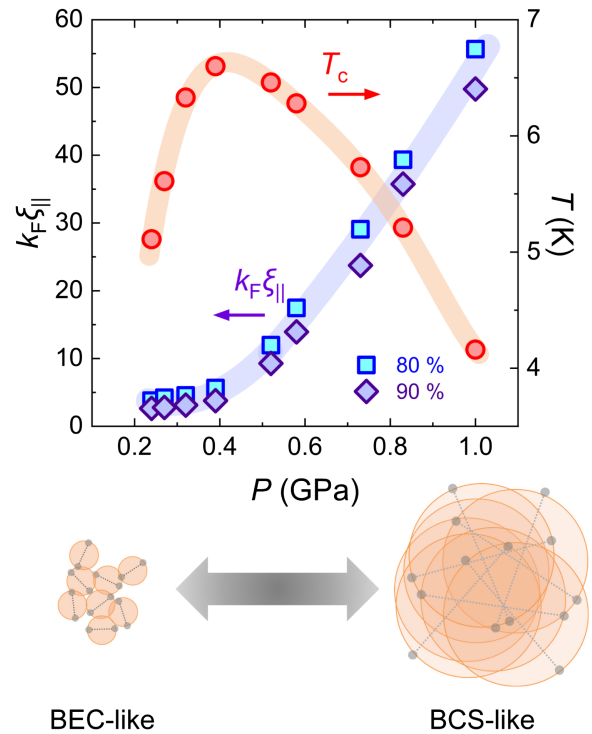

FIG. 19. Pressure dependence of the measured in-plane coherence length $k_F\xi_0^{\mathrm{coh}}$ (where k_F is determined by the Hall coefficient) and superconducting transition temperatures in κ-$(\mathrm{BEDT\text{-}TTF})_4\mathrm{Hg}_{2.89}\mathrm{Br}_8$. If we assume that pressure scales inversely with the effective attractive interaction strength, the T_c dome with overlain coherence length provides an ideal prototype for BCS-BEC crossover in the solid state. From Suzuki *et al.*, 2022.
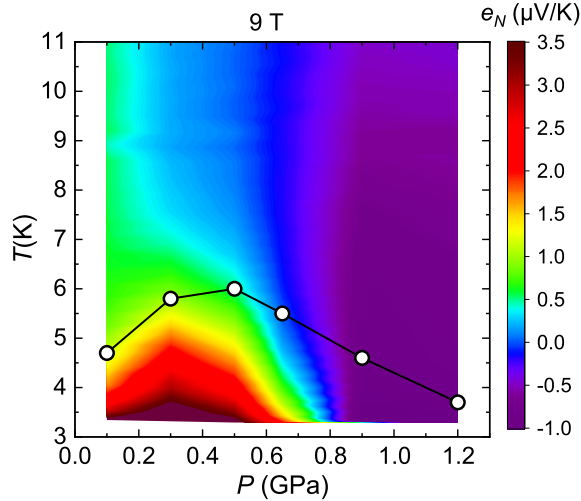
FIG. 20. Temperature-pressure plot of the Nernst signal e_N for the organic superconductor at a magnetic field of 9 T. The white circles indicate the zero-field transition temperature T_c. As the system becomes more strongly paired with decreasing pressure, an enhanced positive Nernst response appears at temperatures far above T_c. From Suzuki *et al.*, 2022.

Adding support to the picture of BCS-BEC crossover in this family of organic metals are studies of nuclear magnetic resonance (NMR) (Kanoda *et al.*, 1996; McKenzie, 1997) and the Nernst coefficient. In a closely related organic superconductor (McKenzie, 1998), NMR experiments have provided evidence for d-wave pairing as well as a pseudogap.

We turn next to the Nernst studies (Suzuki *et al.*, 2022) in the HgBr system, as shown in Fig. 20. In the strong-pairing regime, as T_c is approached from above the Nernst coefficient acquires (Boyack *et al.*, 2021) a large positive (magnetic-field-dependent) value that peaks within the superconducting state and subsequently falls below. From Fig. 20 it can be seen that the Nernst coefficient becomes anomalously large well above the transition temperature for low pressures where the molecular superconductor is closest to the strong-coupling end of the spectrum. This enhancement of the standard Aslamazov-Larkin (AL) contribution is expected (Boyack *et al.*, 2021). It reflects the fact that the noncondensed pairs have a more extended temperature region where the chemical potential of the pairs $|\mu_{pair}|$ (which governs the size of the AL contribution) becomes small. Such an enhancement becomes more pronounced as the system deviates progressively from the BCS regime.

In summary, these studies of κ-(BEDT-TTF)$_4$Hg$_{2.89}$Br$_8$ seem to suggest a welcome convergence between different schools of thought for treating strongly correlated superconductors through the concept of "Mott-driven BCS-BEC crossover." In the context of cuprates both the doped Mott insulator (Lee, Nagaosa, and Wen, 2006) and the BCS-BEC scenarios have been widely discussed. It would appear in this organic superconductor system that both aspects are combined: Mott physics may well provide the source of the pairing mechanism, while BCS-BEC crossover appears to be relevant to the machinery.

B. BCS-BEC crossover in the iron chalcogenides

Considerable attention has been paid to the superconducting properties of iron chalcogenides (Kasahara *et al.*, 2014, 2016; Okazaki *et al.*, 2014; Hanaguri *et al.*, 2019; Kang *et al.*, 2020; Shibauchi, Hanaguri, and Matsuda, 2020; Mizukami *et al.*, 2023), where there appears to be growing evidence that FeSe and isovalent substituted FeSe$_{1-x}$S$_x$ and FeSe$_{1-x}$Te$_x$ may be in the BCS-BEC crossover regime. These systems, in which the characteristic electronic energy scales are anomalously low, appear to exhibit strong-pairing effects. This is not due to two dimensionality, nor is it because the pairing glue itself is particularly large on an absolute scale. Rather, the attractive interaction is large when compared to the characteristic low Fermi energies. Also present, and possibly relevant, are nematic effects (Hashimoto *et al.*, 2020; Shibauchi, Hanaguri, and Matsuda, 2020) associated with broken rotational symmetry (but preserved translational symmetry). FeSe is a layered anisotropic material; it is also a compensated semimetal, with roughly equal densities of electron and hole carriers. This leads to both electron and hole pockets and a more complicated scenario for BCS-BEC crossover.

Adding to the support for a BCS-BEC crossover picture is the fact that in the iron chalcogenides (Shibauchi, Hanaguri, and Matsuda, 2020) the characteristic Fermi energies and zero-temperature gap magnitudes are comparable. STM and STS experiments indicate gap sizes of the order of $\Delta_1 \approx 3.5$ meV and $\Delta_2 \approx 2.5$ meV for the two bands. From this it follows that the ratios of the pairing gaps to transition temperatures ($T_c \approx 9$ K) in FeSe are large, of the order of $2\Delta_1/k_B T_c \approx 9$ and $2\Delta_2/k_B T_c \approx 6.5$, well beyond the BCS value of 3.5. The Fermi energies associated with the two nearly cylindrical Fermi surface sheets are anomalously small, of the order of $E_F \approx 10$–20 meV for the holelike Fermi surface (Shibauchi, Hanaguri, and Matsuda, 2020). This leads to estimates of $T_c/T_F \approx 0.04$–0.08. This analysis has led many to conclude that these superconductors are well outside the strict BCS regime.

ARPES experiments (Hashimoto *et al.*, 2020) on bulk FeSe show that, rather than the characteristic backbending associated with conventional BCS superconductors, there is instead a flat dispersion near $\mathbf{k} = \mathbf{0}$, which appears to be more typical of the crossover regime. This flat-band feature is even more enhanced with the addition of sulfur.

Of considerable importance is the characteristic correlation length extracted from magnetic-field data (Kasahara *et al.*, 2014), which is argued to be small, of the order of $k_F \xi_0^{coh} \approx 1$–4. One can deduce from these numbers that FeSe superconductors are most likely not in the BCS regime. One can also compare these numbers with earlier theoretical estimates of $k_F \xi_0^{coh}$, which found a BEC saturation value of approximately 2 to 3 [Fig. 12(c)]. We caution, however, that complementary diagnostic information comes from vortex imaging using STM. This derives from the subgap fermionic states that are inside the vortex core. The observation of Friedel-like oscillations (Chien, He *et al.*, 2006; Hanaguri *et al.*, 2019) suggests that fermionic degrees of freedom are still present in bulk FeSe, and thus these superconductors are not yet in the BEC regime.
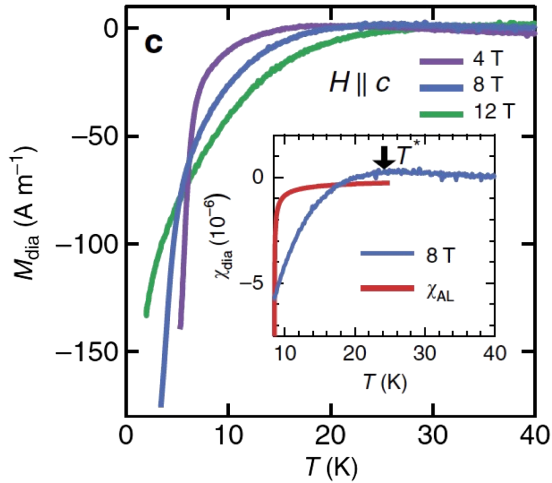
FIG. 21. Diamagnetic magnetization response in bulk FeSe as a function of temperature at different values of the applied magnetic field H. Inset: comparison of the diamagnetic susceptibility χ_{dia} with the predictions χ_{AL} of AL theory (Larkin and Varlamov, 2009), showing an extended range of fluctuations. From Kasahara *et al.*, 2016.

Also notable is that there are enhanced superconducting fluctuation effects (Kasahara *et al.*, 2016) in FeSe. This enables one to identify a characteristic temperature T^* where, in particular, diamagnetism sets in. Figure 21 presents a plot of this "unprecedented, giant" diamagnetic response. The inset serves to emphasize the key point that the diamagnetic fluctuation regime in FeSe is considerably wider than predicted from the conventional fluctuation theory of Aslamazov and Larkin (1975) and Larkin and Varlamov (2009). It was argued that this provides evidence for preformed pairs associated with BCS-BEC crossover, as fluctuation effects are expected to be amplified. Similarly, studies of the dc conductivity showed that the expected downturn behavior is observed in the resistivity. Additionally, NMR experiments (Shibauchi, Hanaguri, and Matsuda, 2020) showed the expected suppression of $1/T_1 T$ around T^*, although there seem to be none of these large fluctuation effects in the heat capacity (Hardy *et al.*, 2019).

There has also been a focus on crossover from BCS to BEC in a slightly different iron chalcogenide (Rinott *et al.*, 2017) $Fe_{1+y}Se_x Te_{1-x}$, where chemically doping the carrier concentration, through decreasing y, introduces an increased ratio of Δ_0/E_F, where E_F is as small as a few meV. Here there are claims[9] based on figures such as Fig. 22 that, as Δ_0/E_F increases, the dispersion of the peak in ARPES evolves from the characteristic backbending behavior seen in the BCS regime to a BEC-like signature with a gap minimum at $\mathbf{k} = \mathbf{0}$.

All of this would make an effective illustration of superconductivity in the intermediate- and even strong-coupling regime, were it not for the fact that STM and STS experiments do not support the existence of a spectroscopic pseudogap in this class of compounds (Shibauchi, Hanaguri, and Matsuda,

---

[9]There are complications in this analysis due to the vicinity of a heavy d_{xy} band, which may affect the interpretation.

2020). Understanding this behavior is still a work in progress; the multiband character of the iron chalcogenides may be relevant here. Issues such as interband pairing may also be playing an important role.

C. BCS-BEC crossover in interfacial superconductivity

A great deal of excitement has been generated recently in studies of interfacial superconductivity (Reyren *et al.*, 2007; Caviglia *et al.*, 2008; Richter *et al.*, 2013; W.-H. Zhang *et al.*, 2014; Cheng *et al.*, 2015; Gariglio *et al.*, 2015; Ge *et al.*, 2015; Gasparov *et al.*, 2017; Rebec *et al.*, 2017; Suyolcu *et al.*, 2017; Wang *et al.*, 2017; Zhang *et al.*, 2019; Kang *et al.*, 2020; Han *et al.*, 2021; Song *et al.*, 2021), particularly involving the iron chalcogenide FeSe. Here one sees an unexpected and dramatic enhancement of the pairing-onset temperature in interfacial monolayer FeSe (Ge *et al.*, 2015). While the early literature (W.-H. Zhang *et al.*, 2014; Rebec *et al.*, 2017; Pedersen *et al.*, 2020) did not often distinguish this pairing-gap onset from that of coherent superconductivity, it is now becoming clear that this system is associated with a large pseudogap, as well as a sizable BKT transition temperature.

Indeed, it was discovered in 2012 (Wang *et al.*, 2012) that one-unit-cell-thick (1UC) FeSe grown on $SrTiO_3$ exhibits a gap that survives up to 60–70 K. Remarkably this gap onset temperature is 1 order of magnitude higher than the T_c of bulk FeSe, and it has inspired an enormous effort to reveal the mechanism driving the interfacial enhancement. Owing to the extreme air sensitivity, it has been challenging to perform traditional resistivity measurements. FeTe-capping or *in situ* transport measurements have made it possible to characterize T_c from the resistivity transition. Among these measurements, except for a singular study that reported a T_c of 109 K, all transport studies reported a resistivity onset associated with coherent superconductivity at $T \lesssim 45$ K.

Recent work by one of us (Faeth *et al.*, 2021) combined *in situ* ARPES and *in situ* transport measurements to simultaneously characterize the spectroscopic and resistive transitions (Fig. 23). The former is sensitive to the presence of a pseudogap that can be associated with pairing, while the latter probes superconductivity. The band structure of the 1UC FeSe is simpler than in the bulk system. Only electron-like Fermi surfaces are identified by ARPES near the Brillouin zone corners, with a Fermi energy $E_F \approx 60$ meV (Liu *et al.*, 2012). An excitation gap $\Delta \approx 15$ meV is observed at 12 K and persists up to 73 K. This leads to a ratio of Δ/E_F of the order of 0.25. The coherence length from vortex mapping is about 2 nm (Chen, Liu *et al.*, 2020), which suggests that $k_F \xi_0^{\mathrm{coh}} \approx 4$. This places 1UC $FeSe/SrTiO_3$ firmly in the BCS-BEC crossover regime, but not yet in the BEC.

A second example of interfacial superconductors that has been interpreted in terms of a possible BCS-BEC crossover scenario (Božović and Levy, 2020) corresponds to a superconductor formed within the conducting 2D interface between two band insulators $LaAlO_3$ and $SrTiO_3$. This belongs to the class of superconductors with anomalously low carrier density. Indeed, it is argued that this 2D superconductor is similar in many ways to the behavior in 3D doped $SrTiO_3$ and also has features of the high-T_c copper oxides. The phase diagram (Richter *et al.*, 2013) shown in Fig. 24 is analogous to the
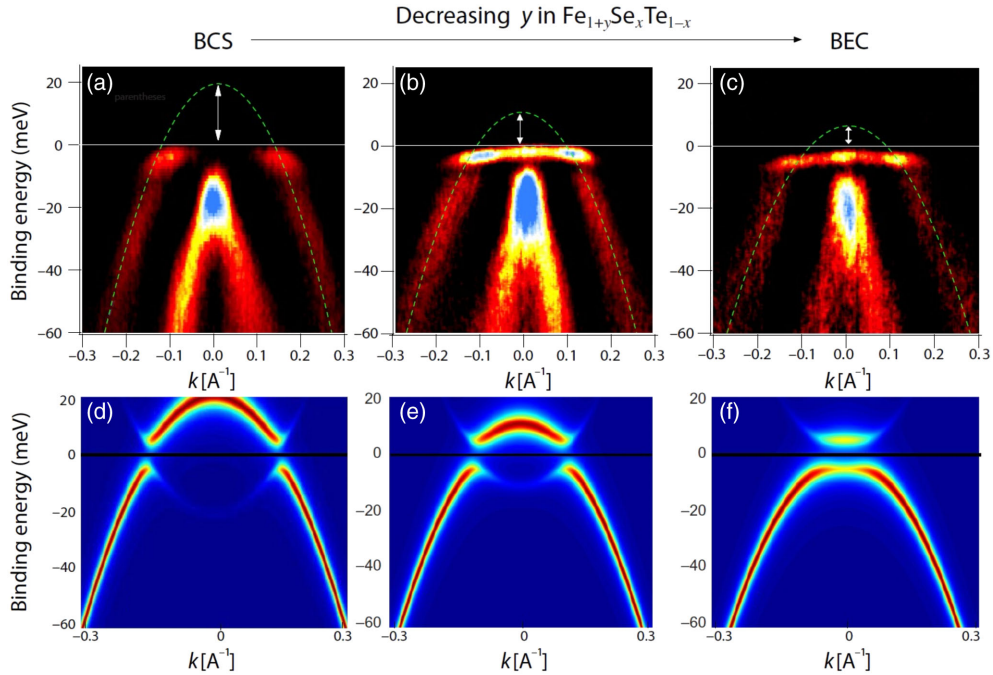
FIG. 22.   ARPES signatures in $Fe_{1+y}Se_xTe_{1-x}$, where chemically doping the carrier concentration is through decreasing y. (a)–(c) ARPES spectra for three samples from left to right, in order of decreasing y. The green dashed line is the best fit to the data. (d)–(f) Theory plots using parabolic band dispersion and other model parameters. From Rinott *et al.*, 2017.

cuprates in many ways; in addition, there are claims of preformed pairs in both. In the two cases the gap onset temperature does not follow T_c in the underdoped region but increases with charge carrier depletion.

This heterostructural system is particularly useful, as it can be tuned continuously through gating. There is a superconducting dome along with a pairing gap Δ that survives up to $T^* \approx 500$ mK for the 2D carrier density $n \sim 0.02$ per unit cell (Richter *et al.*, 2013). At $T = 0$, $\Delta_0 \approx 65$ µeV. Moreover, with decreasing temperature the pseudogap Δ_{PG} evolves smoothly into the pairing gap within the superconducting phase. Also supporting the pairing-onset interpretation of T^* is that the ratio of Δ_0 to T^* remains close to the BCS prediction;

at more general temperatures the pairing gap follows the BCS-like mean-field temperature dependence.

Using an atomic force microscope tip, the Levy group (Cheng *et al.*, 2015) was able to draw single-electron transistors on the $LaAlO_3/SrTiO_3$ interface. This enabled the observation of preformed pairs that persist up to 900 mK, well above the transition temperature, which ranges between 200 and 300 mK.

These temperature scales, however, pose some concern about interpreting the nature of interfacial superconductivity in $LaAlO_3/SrTiO_3$. The Fermi energies of various $3d\ t_{2g}$ bands have been characterized by soft x-ray ARPES (Cancellieri *et al.*, 2014) and found to be around 50 meV
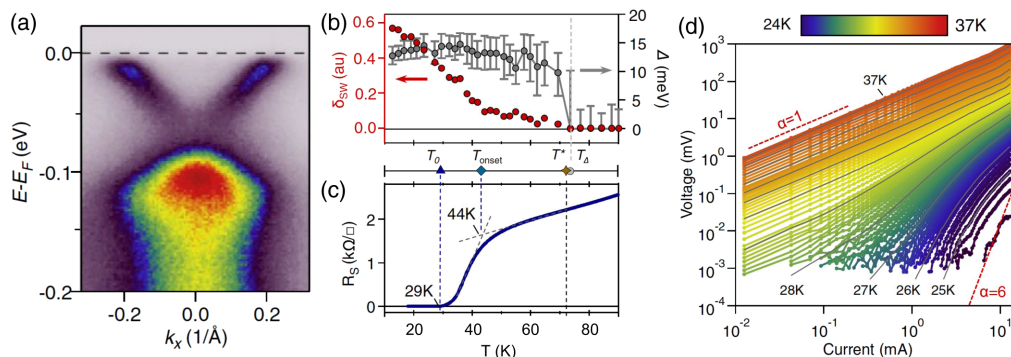

FIG. 23.   Combined ARPES and transport studies on 1UC $FeSe/SrTiO_3$ showing (a) ARPES data near the M point of the Brillouin zone taken at 12 K. (b) Extracted values of the gap Δ and spectral weights δ_{SW} at the Fermi level as a function of temperature. (c) Resistivity measurements. (d) Voltage-current relationship. From Faeth *et al.*, 2021.
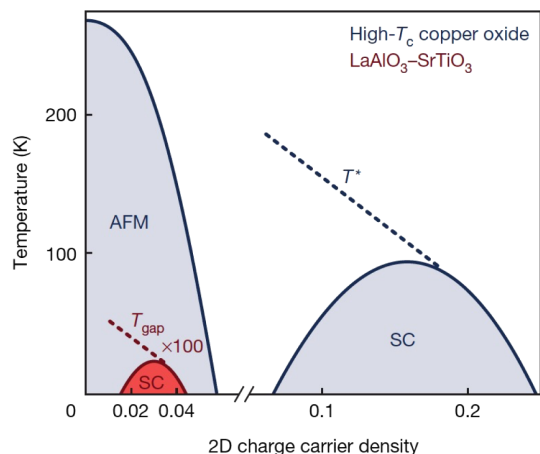
FIG. 24. Interface superconductivity in LaAlO$_3$-SrTiO$_3$ (shown in red), which is tuned with an electric gate field. Represented is a comparison between high-T_c cuprate superconductors and the *n*-doped interface superconductors. The horizontal axis is the carrier density per unit cell. The end point of the LaAlO$_3$-SrTiO$_3$ SC dome on the underdoped side is a quantum critical point that separates the superconducting from an insulating phase (Caviglia *et al.*, 2008). SC, superconducting; AFM, antiferromagnetic. From Richter *et al.*, 2013.

for the d_{xy} orbital band (Sulpizio *et al.*, 2014; Pai *et al.*, 2018),[10] which leads to a rather small ratio of $\Delta_0/E_F \sim 10^{-3}$.

This observation, indicative of a more BCS-like system, appears to be incompatible with a strong-pairing crossover scenario. Even more persuasive of this incompatibility is the additional fact that the measured coherence length is large, of the order of 30–70 nm (Fillis-Tsirakis *et al.*, 2016), leading to $k_F \xi_0^{\text{coh}} \approx 30$–70. This is based on previous estimates in the literature for $k_F \approx 0.1$ Å^{-1} (Pai *et al.*, 2018).

There is strong evidence that disorder effects are important in this interfacial superconductor (Chen *et al.*, 2018). In particular, Chen *et al.* (2018) showed that applying an electrostatic gate voltage not only tunes the carrier density but also significantly modifies the interfacial disorder via the mobility. Nevertheless, it is somewhat difficult to associate a phase diagram like that in Fig. 24, in which there is a T_c dome while T^* is monotonic, with the effects of disorder. This behavior of T^* can be contrasted with the disorder-induced pseudogap effects discussed in Sec. VI. While there is some uncertainty, a reasonable conclusion is that disorder is relevant to interfacial superconductivity in LaAlO$_3$/SrTiO$_3$, and a strong-pairing mechanism does not seem to be operative. Possibly related to these observations are theoretical calculations (Che *et al.*, 2017), albeit for 3D *s*-wave systems, that reveal that disorder-induced superconductor-insulator

quantum phase transitions can occur in the BCS regime. Here the superconducting order is destroyed, leading to an insulating phase that is caused by a residual pseudogap.

D. BCS-BEC crossover in magic-angle twisted bilayer and trilayer graphene

There is growing support that MATBG (Cao *et al.*, 2018) as well as MATTG (Park *et al.*, 2021; Kim *et al.*, 2022) superconductors exhibit BCS-BEC crossover features. Notably these are clean systems associated with a BKT transition. One piece of cited evidence is based on the relatively large values of T_{BKT}/T_F. These were reported in the initial groundbreaking paper by Cao *et al.* (2018), as well as in subsequent works (Lu *et al.*, 2019; Oh *et al.*, 2021; Kim *et al.*, 2022). Such estimates are in turn based on *V-I* plots that allow one to determine the BKT transition that occurs when $V = I^\alpha$ with a specific value of $\alpha = 3$. As a caution we note that the ratio T_{BKT}/T_F should not be viewed as a proxy for the fraction of electrons involved in superconductivity; in the BEC regime, this parameter becomes extremely small.

More recent tunneling experiments on MATBG [which are summarized in Fig. 25(a)] help to make the association with BCS-BEC crossover stronger (Oh *et al.*, 2021). They have presented clearer indications of an extensive pseudogap regime in the phase diagram, as can be seen in Fig. 25. These STM experiments suggest an anomalously large value for the ratio $2\Delta_0/k_B T_{\text{BKT}} \approx 25$ (Oh *et al.*, 2021) that can be viewed as representative of strong pseudogap effects and can be equivalently associated with large T^*/T_{BKT}. Adding support to a BCS-BEC crossover scenario is the presence of another much smaller energy-gap scale associated with point-contact Andreev tunneling, which is present only in the ordered phase where there is phase coherence.

The results from this STM tunneling (Oh *et al.*, 2021) provide a value for $\Delta_0 \approx 1.4$ meV in MATBG. We previously pointed out that *V-I* measurements in 2D films can be used (Zhao *et al.*, 2013) for estimates of T^*. One can infer from these data (Cao *et al.*, 2018) that $T^* = 3$–5 K, which is obtained from the Ohmic recovery temperatures.[11] One can compare this to the transition temperature $T_{\text{BKT}} \approx 1$ K and the estimated Fermi temperature of the bilayer system, $T_F \approx 20$ K (Cao *et al.*, 2018). The resulting relatively large ratios of T^*/T_{BKT} and Δ_0/E_F suggest that MATBG is a superconductor in the intermediate BCS-BEC crossover regime.

Indeed, based on the claims (Oh *et al.*, 2021) that MATBG has some similarities with high-T_c superconductors, it is striking to observe similar T^*/T_F and T^*/T_c values in Fig. 40 (in Appendix C) for the underdoped cuprates and both twisted graphene families of superconductors. That figure addresses this similarity more quantitatively.

The situation for MATTG appears to be somewhat clearer and provides more quantitative information. Some pertinent results (Park *et al.*, 2021; Kim *et al.*, 2022) are summarized in

---

[10]We note that in the literature whether or not the d_{xy} orbital actively participates in the superconductivity is still being debated; see Scheurer and Schmalian (2015). Using the d_{xz}/d_{yz} orbital bands for E_F would lead to a relatively larger $\Delta_0/E_F \sim 0.05$. Our choice of the d_{xy} band for E_F is based on the consistency between the estimated Δ_0/E_F and $k_F \xi_0^{\text{coh}}$.

[11]Ideally one could arrive at more accurate numbers by making systematic *V-I* plots over finely separated temperature intervals in order to more precisely establish the temperature for the Ohmic recovery, which corresponds to T^*.
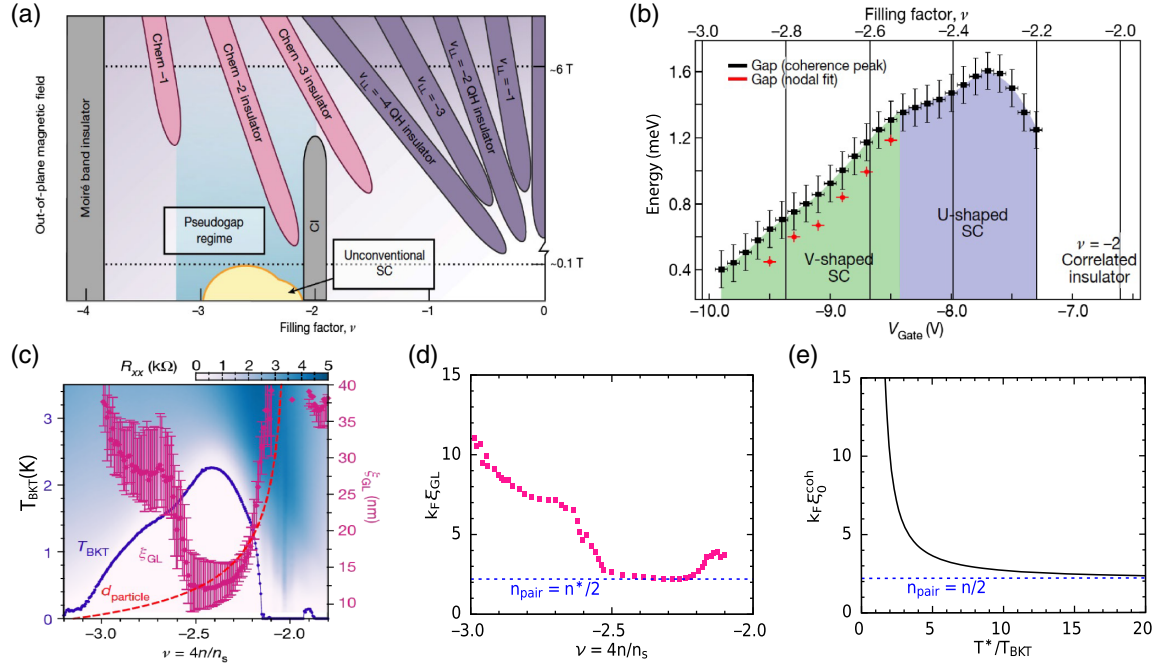
FIG. 25.   Superconducting properties of MATBG and MATTG. (a) Phase diagram of hole-doped MATBG superconductors (SC). The electron filling factor $\nu = 4n/n_s$, where n is the carrier density defined by the applied gate voltage and n_s is the corresponding n when the lower fourfold degenerate moiré flat band is fully filled. The displayed large pseudogap regime, indicated in light blue, is determined by combining conventional STM and point-contact Andreev tunneling spectroscopy (Oh *et al.*, 2021). (b) Gap size Δ vs the gate voltage V_{Gate} (and the filling factor ν) for MATTG. Δ is measured from conventional STM tunneling at low temperatures. The data points are extracted from the separation between coherence peaks at the halfway point (black squares) and from a nodal gap fit (red dots) (Kim *et al.*, 2022). In the green and violet regions the dI/dV curve exhibits a V shape and a U shape, respectively. (c) $T - \nu$ phase diagram of MATTG at displacement field $D/\epsilon_0 = -0.5$ V nm^{-1}, along with the curves of the interparticle distance $d \equiv d_{\text{particle}}$ and the coherence length ξ_{GL} (Park *et al.*, 2021). Here $d_{\text{particle}} = 1/\sqrt{n^*}$, where n^* is the effective carrier density that can be deduced from quantum-oscillation and Hall density measurements. Note that n^* is different from the density n. (d) Replotting of the ξ_{GL} data from (c) in terms of the product $k_F\xi_{\text{GL}}$. To convert n^* to k_F we use $k_F = (2\pi n^*)^{1/2}$. The dashed blue line shows the expected $k_F\xi_{\text{GL}}$ value when n_{pair} saturates to $n^*/2$. (e) Product $k_F\xi_{\text{GL}}$ calculated theoretically as a function of T^*/T_{BKT} for a 2D s-wave superconductor. In the theoretical calculation, n^* is the same as n.

Figs. 25(c) and 25(d), which address useful coherence-length experiments (Park *et al.*, 2021) based on the magnetic-field dependence of the superconducting transition temperature. Figure 25(c) shows published data for ξ_0^{coh} as well as the interparticle distance d as a function of the band filling factor ν, along with the transition temperature T_{BKT}. We note that the error bars are large here, indicative of the experimental challenges encountered when deducing the coherence length using resistivity measured at a finite magnetic field. Particularly in two dimensions and in extreme type-II superconductors, the presence of a magnetic field necessarily leads to broad transitions that make it difficult to establish $T_c(H)$ without incorporating a fairly arbitrary standard for determining where the transition is located.

The experimentally observed[12] dimensionless product $k_F\xi_0^{\text{coh}}$ [Fig. 25(d)] can be compared with the theory in Fig. 25(e), where $k_F\xi_0^{\text{coh}}$ is plotted as a function of T^*/T_c. [This is similar to the inset in Fig. 12(c).] We note that the plot

in Fig. 25(d) and the theoretical plot in Fig. 25(e) are for different horizontal axis variables; however, a direct association of the two would allow one to relate the important ratio T^*/T_c to the filling factor ν, hence completing the T^*/T_c vs ν phase diagram. From the data in Fig. 25(d) it follows that for $\nu \gtrsim -2.5$ MATTG also belongs in the intermediate BCS-BEC crossover regime.

Recent tunneling experiments (Kim *et al.*, 2022) provided additional important quantitative information about MATTG, with a focus on the gap energy scale plotted in Fig. 25(b) as a function of ν. These studies indicated that $T^* = 7$ K at the ν value where the gap is at maximum. Additional parameters are $T_{\text{BKT}} \approx 2.25$ K (Park *et al.*, 2021), with the estimated Fermi temperature given by $T_F \approx 30$ K.

Overall, there appears to be compatibility between the ξ_0^{coh} data from the MIT group and pairing-gap experiments (Kim *et al.*, 2022) shown in Fig. 25(b). Making use of the estimates of E_F based on quantum-oscillation experiments (Park *et al.*, 2021), it follows that the ratio Δ_0/E_F exhibits a trend similar to ξ_0^{coh}, changing from more BCS-like behavior at $\nu \approx -3$ to characteristic crossover behavior at $\nu \approx -2.2$. We note that interpretations of these tunneling experiments (Kim *et al.*, 2022) have suggested that the BEC regime is reached around

---

[12]Note that the band degeneracy used in the conversion here is 2, not the naive 4. As supported by experiments, the spin-valley degeneracy is broken to 2 at $-3 < \nu \lesssim -2$.
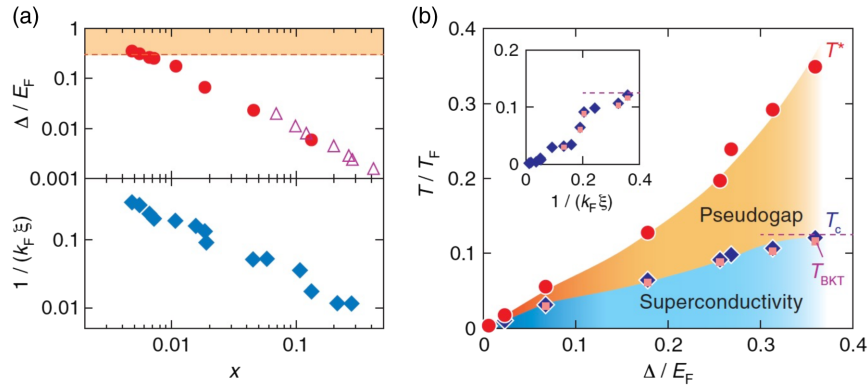
FIG. 26. Experimental data in electron-doped zirconium nitride chloride. The results are from tunneling spectroscopy and dc resistivity measurements. The transition temperature T_c is defined as the midpoint in the resistivity curves, which is identified as T_{BKT}. The in-plane coherence length $\xi = \xi_0^{coh}$ is determined from the temperature-dependent upper critical magnetic field measured near the zero-field T_c. From Nakagawa *et al.*, 2021.

the upper half of the T_{BKT} dome at $\nu \gtrsim -2.5$, although it is not straightforward to reconcile a BEC phase with the presence of coherence peaks seen in the tunneling data.

Finally, we additionally note that the theoretical plot of the coherence length in Fig. 25(e) is for the *s*-wave case, while the experimental data seem to suggest a nodal form of super-conductivity. Some aspects of the crossover theory for an anisotropic gap symmetry were addressed in Sec. IV.B,[13] but one might additionally expect that other ingredients such as flat energy bands and quantum geometry (discussed in Sec. V.E) may play an important role as well in reaching an ultimate understanding of BCS-BEC crossover for MATBG and MATTG.

E. BCS-BEC crossover for 2D gated semiconductors

There has been recent interest (Saito, Nojima, and Iwasa, 2016; Nakagawa *et al.*, 2018, 2021) in a group of layered nitrides Li$_x$ZrNCl, which are intrinsically semiconductors and exhibit superconductivity through Li-intercalated doping. These experiments impose control of the carrier density by use of ionic gating, which provides access to low-carrier-density systems that are otherwise inaccessible. Concomitantly, the varying carrier number enables a tuning of the weakly to strongly coupled superconducting regimes by simultaneously controlling the carrier density and a dimensional crossover from anisotropic three dimentions to two dimensions. Both tunneling and resistivity measurements (Nakagawa *et al.*, 2021) yield systematic information about the detailed phase diagram of this system.

This phase diagram (Nakagawa *et al.*, 2021), which is shown in Fig. 26, indicates a pronounced pseudogap regime established from dI/dV measurements. This is particularly notable at low carrier densities, where the system is more two dimensional. In particular, at extreme underdoping T_{BKT} shows a maximum of 19 K. In the most underdoped

---

[13]In the single band *d*-wave case, the counterpart of the curve in Fig. 25(e) looks qualitatively similar at low density but will not reach BEC until a much larger T^*/T_{BKT} result. No BEC is found at high densities.

sample probed, $\Delta_0/E_F \approx 0.3$, $T_{BKT}/T_F \approx 0.12$, and T^* is roughly $3T_{BKT}$.

A summary (Nakagawa *et al.*, 2021) of experimental observations is presented in Fig. 26 as a plot in terms of T/T_F vs Δ_0/E_F, with data points indicating T_{BKT} and T^*. The pseudogap and associated T^* were found to be largest when the carrier number was lowest. Here for these large gap systems (which are in the strong-coupling limit) one finds the smallest coherence length $k_F\xi_0^{coh} \approx 3$, as obtained from the upper critical fields. This suggests a system that may be close to but not yet in the BEC regime. In the opposite, highest electron doping regime, one recovers more characteristic BCS behavior with $T_{BKT} \approx T^*$. We conclude that all of this constitutes a body of evidence that lends reasonably strong support to a BCS-BEC crossover description of these ionic gated superconductors.

F. Magnetoexciton condensates with BCS-BEC crossover

The concept of condensation based on particle-hole pairs (Kohn and Sherrington, 1970; Comte and Nozières, 1982; Combescot, Combescot, and Dubin, 2017) is a natural extension of particle-particle pairing in superconductors. Indeed, one usually invokes the same ground-state wave function as in Eq. (1), here modified by replacing one of the electron operators with a hole operator and presuming that the two are associated with different bands. This subject has generated considerable enthusiasm, as one could conceive of such condensation as taking place at high temperatures. There are a number of subtle features, however, as the electrons and holes need to be sufficiently well separated to avoid recombination. Their number and effective masses also need to be equivalent; otherwise, pairing could be impeded, as this system would behave like a superfluid with population or mass imbalance.

An important configuration for arriving at exciton condensation involves quantum Hall fluids (Eisenstein, 2014; Eisenstein, Pfeiffer, and West, 2019), as was first implemented by Eisenstein, Pfeiffer, and West (2019) in a GaAs/AlGaAs heterostructure. Here two thin GaAs layers are separated by the AlGaAs spacer layer, which serves to mitigate electron-hole

recombination processes. Because each layer forms a 2D electron gas, in the presence of a strong perpendicular magnetic field B their energies are quantized into Landau levels (LLs). These bilayer quantum Hall systems have the potential to realize novel quantum states that have no analog in a single layer. A relevant parameter for characterizing such states is d/ℓ_B, where d is the interlayer spacing and $\ell_B = \sqrt{\hbar/|eB|}$ is the magnetic length.

There has been a focus (Eisenstein, 2014) on the interlayer coherent state observed in the zero or small interlayer tunneling limit and at total electron filling fraction $\nu_{\text{tot}} = \nu_1 + \nu_2 = 1/2 + 1/2 = 1$. Here the electron filling fraction $\nu_i = n_i(2\pi\ell_B^2)$ is defined for each individual layer, with n_i the electron density of the ith layer. Important questions such as whether there is a quantum phase transition separating the large and small d/ℓ_B limits have been raised (Halperin, 1983; Murphy *et al.*, 1994; Moon *et al.*, 1995; Bonesteel, McDonald, and Nayak, 1996), although recently it was suggested that the evolution of the state from the large to small d/ℓ_B might be understood as a crossover of BCS behavior to a BEC of magnetoexcitons (Sodemann *et al.*, 2017; Wagner *et al.*, 2021; Liu *et al.*, 2022).

This picture can be understood in terms of Jain's composite fermions (CFs) (Jain, 2007), where a CF can be roughly viewed as the original electron attached to two magnetic flux quanta $(2h/e)$. In the extreme $d \to \infty$ limit, the two layers decouple and each of them has a LL filling fraction $\nu = 1/2$ that can be described by a metallic state (Halperin, Lee, and Read, 1993) of either electronlike or, equivalently, holelike CFs with well-defined Fermi surfaces.

At finite d one can then consider electronlike and holelike CFs from the two different layers forming interlayer Cooper pairs, i.e., magnetoexcitons. It is reasonable to assume that their effective masses are equal near $\nu = 1/2$ due to an approximate particle-hole symmetry. The pair formation is driven by an interlayer attraction U that is derived from the original interlayer Coulomb interaction between electrons and holes, whose magnitude[14] is $|U| \sim V_{\text{inter}} \sim e^2/\epsilon d$. Here ϵ is the background dielectric constant. At the same time the parameter E_{kin}, which represents the kinetic energy of a partially filled Landau state, is set by the intralayer Coulomb repulsion $E_{\text{kin}} \sim V_{\text{intra}} \sim e^2/\epsilon\ell_B$ (Halperin, Lee, and Read, 1993).

In this way the important ratio $|U|/E_{\text{kin}} \propto \ell_B/d$ that sets the scale of a BCS-BEC crossover can be tuned experimentally by varying either d or B. Large-d or high magnetic fields correspond to the BCS-like limit, while the BEC regime is present at small-d or low magnetic fields; see Fig. 27. This BCS-BEC crossover picture is supported by recent measurements on graphene double-layer heterostructures (Liu *et al.*, 2017, 2022). Compared to the GaAs/GaAlAs double-layer experiments, this graphene bilayer system has an additional

<hr>

[14]When $d \ll \ell_B$, the interlayer interaction is actually governed by $e^2/\epsilon\ell_B$, not $e^2/\epsilon d$. We also note that the actual interlayer interaction between the CFs is not the same as V_{inter}. Instead, it is mediated by an emergent Chern-Simons gauge field that makes the renormalized interaction highly frequency dependent (Halperin, Lee, and Read, 1993; Bonesteel, McDonald, and Nayak, 1996; Wang *et al.*, 2014). Here we ignore these complications.
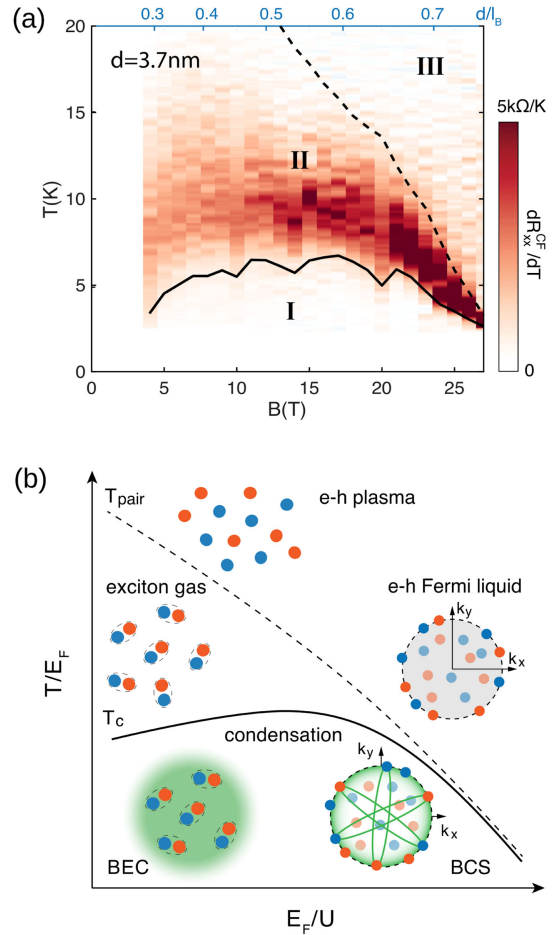

FIG. 27. BCS-BEC crossover for magnetoexcitons. (a) Color coding is associated with the temperature derivatives of the measured longitudinal resistance in the counterflow configuration. Hall drag and counterflow resistances are used, respectively, to arrive at the pairing-onset temperature T^* (dashed line) and to infer T_c (solid line) as a function of the ratio of kinetic energy over effective attraction (through the magnetic field B). (b) Schematic phase diagram expected for a magnetoexciton condensate. T_{pair} is the same as T^*. From Liu *et al.*, 2022.

advantage, as it allows the two graphene layers to be separated by a thin hexagonal boron nitride layer, which prohibits direct interlayer tunneling without introducing disorder.

Because the magnetoexcitons are neutral and cannot be probed in traditional electronic transport, two unconventional designs for resistance measurements have been employed to experimentally probe the magnetoexciton superfluidity via "counterflow" and "drag" experiments (Eisenstein, 2014). Figure 27 presents a summary of the results from these measurements for the double-layer graphene system (Liu *et al.*, 2022).

In the counterflow configuration electric currents in the two layers are of the same magnitude but flow in opposite directions. The absence of dissipation due to "superfluidity" is associated with a vanishing R_{xx}^{counter} that measures the longitudinal resistance. These experiments serve to determine the transition temperature T_c (solid black line) in Fig. 27(a).

A striking signature of magnetoexcitonic superfluidity is a quantized Hall drag resistance at low temperature in the

so-called drag configuration. Here the electric current is fed to only one layer, while the Hall voltage drops are measured in both layers, from which one can define the usual Hall resistance R_{xy} for the current-driving layer. One can also define a Hall drag resistance R_{xy}^{drag} for the passive layer.

Both R_{xy} and R_{xy}^{drag} are expected to be quantized to the same value $h/(e^2 \nu_{\text{tot}})$ at low T. As T increases above T_c, R_{xy}^{drag} decreases monotonically. Liu *et al.* (2022) defined the important temperature scale T^* as the point where R_{xy}^{drag} drops to below 50% of $h/(e^2 \nu_{\text{tot}})$. This temperature T^* is plotted in Fig. 27(a) as the dashed black line. It is reasonable to associate the residual R_{xy}^{drag} at high temperatures with incoherent pair correlations between electronlike and holelike CFs. In this way one interprets T^* as the onset of electron-hole CF pair formation. While there are some uncertainties in the definition of T^*, a clear separation of the two temperature scales T_c and T^* is apparent from Fig. 27(a), which is to be compared to the schematic phase diagram sketched in Fig. 27(b).

What is not as clear is whether at the lowest applied magnetic field $B \approx 5$ T the system has reached the BEC regime, as suggested[15] by Fig. 27. In comparing with a prototypical example of BCS-BEC crossover, as in the 2D electron gas, it is useful to establish the magnitude of the effective Δ_0/E_F, which would be expected to become arbitrarily large in a more traditional BEC superconductor. However, exact diagonalization studies showed that for the bilayer magnetoexciton system $\Delta_0 \lesssim E_F$ (Wagner *et al.*, 2021). This contrast highlights some of the key differences between traditional superconductors and the magnetoexciton bilayer that one needs to bear in mind in the interpretation of the phenomenology. Quantification of the exact behavior of T_c/T_F, and other quantities characteristic of BCS-BEC crossover, for the entire range of d/ℓ_B from ∞ to 0 requires further work, both theoretical and experimental.

Since one defining feature of the BEC regime is the disappearance of Fermi surfaces, a potentially useful future experiment is to directly probe the Fermi surface of CFs at $T_c < T < T^*$ for small d/ℓ_B, using geometric resonance techniques as employed in the determination of the Fermi wave vector of CFs for the single layer $\nu = 1/2$ state (Kamburov *et al.*, 2014). Achieving a number of these goals seems promising given the high tunability of the bilayer graphene heterostructure, as demonstrated in a new generation of experiments (Liu *et al.*, 2017, 2022).

VIII. APPLICATION TO THE CUPRATES

A. Support for and counterarguments against BCS-BEC crossover in the cuprates

The question as to whether a BCS-BEC scenario is relevant to the cuprates is, like all aspects of the cuprate literature, a highly controversial one. Despite this controversy, it is useful

---

[15]Rescaling the measured T_c of the top panel by T_F, which can be estimated as $e^2/\epsilon \ell_B$, and plotting the obtained T_c/T_F as a function of B shows that this ratio has not passed the point where it starts to decrease with decreasing B even at $B \approx 5$ T. It suggests that the system may still be in the crossover regime, not yet into the BEC, if we compare this trend of T_c/T_F to that for the 2D electron gas in Fig. 11.

to let readers make an independent judgment; thus, here we discuss the implications of such a theory for the cuprates. We address aspects that are both consistent and inconsistent with the data.

There are claims in the literature that the cuprates are somewhere between BCS and BEC. We cite some of these here.

- From Leggett (2006): "The small size of the cuprate pairs puts us in the intermediate regime of the so-called BCS-BEC crossover."
- From Hufner *et al.* (2008): "High-T_c superconductors cannot be considered as classical BCS superconductors, but rather are smoothly evolving from BEC into the BCS regime."
- From Božović and Levy (2020): "We show the likely existence of preformed pairs in the cuprates…. The existence of preformed pairs is a necessary but not sufficient condition for BEC or for BCS-BEC crossover to occur. Indeed, since Fermi surfaces have been mapped out … this favors a picture in which pairing is relatively strong, pre-formed pairs first appear at $T > T_c$ … but copper oxides are still on the BCS side of the crossover."
- From Uemura (1997): "Combining universal correlations … and pseudogap behavior in the underdoped region, we obtain a picture to describe superconductivity in cuprate systems in evolution from Bose-Einstein to BCS condensation."

We note that, even if BCS-BEC crossover theory plays a role in the cuprate superconductors, this will not address or elucidate a number of important issues that characterize their behavior and need to be understood in an ultimate theory. Among these is the pairing mechanism (Lee, Nagaosa, and Wen, 2006), which remains unknown; also challenging is arriving at an understanding of the "strange metal" behavior including the linear temperature dependence of the resistivity, which is widespread among other strongly correlated superconductors (Varma, 2020). Another puzzle is the distinct change observed in carrier concentration as a function of hole doping, which seems to correlate with the presence of a pseudogap (Proust and Taillefer, 2019). This appears to be consistent with recent ARPES claims (Chen *et al.*, 2019) that the pseudogap suddenly collapses at a fixed hole concentration.

We next list issues that have been raised to challenge the relevance of BCS-BEC crossover theory for the cuprates. Examples are the following:

(1) Current cuprate experiments show no sign of a chemical potential μ that is near or below the band bottom, as might be expected in the BEC regime. This would show up in ARPES experiments.

(2) T_c and T^* are observed to vary inversely in the underdoped regime. Some have argued that if T^* were related to preformed pairs, then as pairing becomes stronger both T_c and T^* would tend to increase together.

(3) One finds that a number of (but not all) superconducting fluctuation phenomena appear only in the immediate vicinity of T_c, which is well below the pseudogap onset temperature T^* (Vishik, 2018).

(4) There are multiple signatures of a "nodal-antinodal dichotomy" (Hashimoto *et al.*, 2014) corresponding to different behavior of the d-wave energy gap along the

nodal and antinodal directions. This is widely inter-
preted to mean that rather than preformed pairs,
another (unspecified) ordering must be responsible
for the pseudogap, which is mostly confined to the
antinodes.

(5) There are ARPES experiments (Hashimoto *et al.*, 2010)
that indicate that at higher temperatures in the normal
state, but well below T^*, the fermionic dispersion shows
disagreement with the characteristic energy dispersion
associated with BCS-like quasiparticles.

(6) There are other indications of additional ordering
associated with the pseudogap phase (Ghiringhelli
et al., 2012), quite possibly with an onset associated
with its boundary (Xia *et al.*, 2008; Zhao *et al.*, 2017).

(7) There are claims (Tallon *et al.*, 1999) suggesting that
quantum critical behavior is present such that T^*
actually vanishes beneath the superconducting dome;
this is inconsistent with the BCS-BEC crossover
picture, in which T^* is necessarily larger than T_c.

Of this list of seven items, the last two seem to be most
challenging for the BCS-BEC crossover scenario, while the
first five are not necessarily so, as discussed in this section and
in Appendices A–C. Attributing the cuprate pseudogap to
preformed pairs as distinguished from a competing order
parameter is admittedly highly controversial. This is not a
central component of this review, which is focused principally
on noncuprate superconductors. Nevertheless, for complete-
ness it is useful to present the predictions concerning the
cuprates that are derived from one particular preformed-pair
scenario: a BCS-BEC crossover perspective. The discussion
presented here and in Appendices B and C functions as a
catalog summary of some relevant theory in the literature.
Further details are provided in the cited papers.

**B. Experimental evidence that BCS-BEC crossover may be
relevant to the cuprates**

All indications are that, if this scenario is relevant to the
cuprates, these superconductors are on the BCS side and well
away from BEC (Chen *et al.*, 2024). This is consistent with the
claims in a recent paper by Sous, He, and Kivelson (2023),
although they adopted a different definition of crossover
associating it with proximity to a BEC. Indeed, there are
several experiments that stand out as providing among the
strongest support for a BCS-BEC-crossover-like description
of the copper oxides.

ARPES measurements (Kanigel *et al.*, 2008) reveal a
Bogoliubov-like dispersion in part of the Brillouin zone that
is away from the nodal Fermi-arc region. This is observed
slightly above T_c, as shown in Fig. 28. It is highly unlikely,
and indeed inconsistent with the theory that we are discussing
[see Eq. (16), which bears on point 5 in Sec. VIII.A], that this
Bogoliubov dispersion continues up to much higher temper-
atures near the onset of the pseudogap. Indeed, there are
studies that suggest that this characteristic backbending
dispersion is absent well below T^* (Hashimoto *et al.*,
2010). But in the normal state not far from T_c these experi-
ments provide indications that the presence of a pseudogap is
associated with the same fermionic quasiparticles as are found
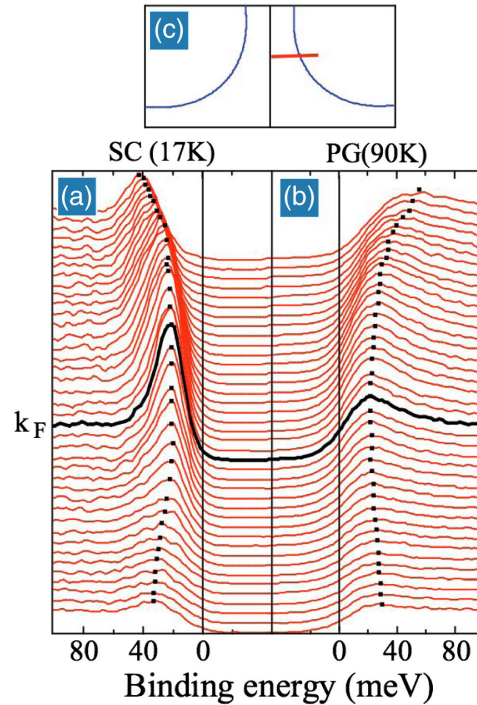in the ordered phase (Kanigel *et al.*, 2008).

FIG. 28. Experimental pseudogap ARPES data showing back-
bending of the dispersion in the normal state (b), which is
suggestively similar to that in the superconducting state (a).
The energy distribution curves were measured at the momenta
along the cut in the Brillouin zone shown in (c). From Kanigel
et al., 2008.

In a similar vein a smooth evolution of the measured
ARPES excitation gap around the antinodes as the temper-
ature is varied from above to below T_c lends some support to
the crossover picture. An additional, conceptually simple
experiment involves STM studies that compare the ratio of
the zero-temperature pairing gap to T^*. This ratio appears to
be close to the expected mean-field result (Oda *et al.*, 1997;
Kugler *et al.*, 2001). This associates the ratio of Δ_0 and T^* in a
fashion analogous to the BCS prediction of Δ_0 and T_c and for
d-wave pairing.

There are additional classes of experiments that constitute
less direct support but are worthy of note and thus are
discussed in this section. These involve the following:

(i) Recent shot-noise measurements (Zhou *et al.*, 2019),
which provided a more direct and quantitative sig-
nature of pairing above T_c. Through pair contributions
to tunneling, these shot-noise experiments (Zhou *et al.*,
2019) indicated that pairs of charge $2e$ are present in
large portions of the parameter space dominated by the
pseudogap. We caution here, however, that evidence of
$2e$ pairing may be found in the pseudogap phase of
highly disordered, presumably weakly coupled 2D
superconductors (Bastiaans *et al.*, 2021). In this way,
$2e$ pairing is a necessary but not sufficient effect to
establish BCS-BEC crossover.

(ii) Also relevant is the two-gap dichotomy (Hufner *et al.*,
2008; Hashimoto *et al.*, 2014) in which there are
distinctive temperature dependencies of the ARPES-
or STM-associated gaps in the nodal and antinodal

regions. In the BCS-BEC crossover scenario this two-gap behavior derives from the simultaneous presence of condensed and noncondensed pairs.

(iii) Additionally, an observed downturn in the dc resistivity near or below T^* seems to be most naturally associated with the contribution from bosonic transport or from preformed pairs (Timusk and Statt, 1999). Indeed, this small downturn feature is often used as the canonical signature of T^*.

(iv) Lending some support to the crossover picture is the behavior of the GL coherence length in the cuprates, which is still not firmly established, as it turns out to be difficult to measure due to vortex liquid effects. Some indications of behavior that is rather similar to that found in the organic 2D superconductor (Suzuki *et al.*, 2022) are seen in Fig. 14(a) of Suzuki and Hikita (1991). This is measured above T_c in the normal state (Chen *et al.*, 2024).

(v) Finally, there is a notable similarity between many properties of a single-layer cuprate material and that found for its counterpart in bulk systems (Y. Yu *et al.*, 2019); this seems to be compatible with the similarity contained in Eqs. (3) and (5).

We discuss some of these experiments in Secs. VIII.C–VIII.H.

C. The spectral function: Distinguishing condensed and noncondensed pairs

We first address the so-called two-gap dichotomy (Hufner *et al.*, 2008; Hashimoto *et al.*, 2014), which pertains to the behavior of the spectral function, where it should be clear that d-wave pairing plays an important role. In the BCS-BEC crossover scenario (Chen *et al.*, 2005) the fermionic self-energy, which is measured in the spectral function, has two contributions from noncondensed (PG) and condensed (sc) pairs,

$$\Sigma(\omega, \mathbf{k}) = \frac{\Delta_{\mathrm{PG},\mathbf{k}}^2}{\omega + \xi_{-\mathbf{k}} + i\gamma} + \frac{\Delta_{\mathrm{sc}}^2}{\omega + \xi_{-\mathbf{k}}} + i\Gamma_0. \quad (31)$$

This same spectral function appeared earlier as Eq. (10), but here we emphasize the momentum dependence associated with non-s-wave pairing, and, as customary, we add an additional phenomenological lifetime Γ_0 arising from incoherent, single-particle scattering processes. Note that, because of these two components, this BCS-BEC crossover scheme has Green's functions that are similar to those in a well-known cuprate theory often called the Yang-Rice-Zhang (YRZ) theory (Rice, Yang, and Zhang, 2012). In the BCS-BEC crossover scenario one finds Fermi arcs, whereas YRZ incorporates Fermi pockets (Scherpelz *et al.*, 2014).

In the normal state, a form (Chen and Levin, 2008) similar to Eq. (31) was shown (Norman *et al.*, 1998) to provide a reasonably good fit to ARPES data and insights into the Fermi arcs (Kondo *et al.*, 2015). How do the Fermi arcs originate? Note that the noncondensed pairs have a finite lifetime, in contrast to the condensate. This is particularly important for the case of d-wave pairing. If we consider cooling from above to below T_c, we see that the onset of the condensate gap Δ_{sc} in
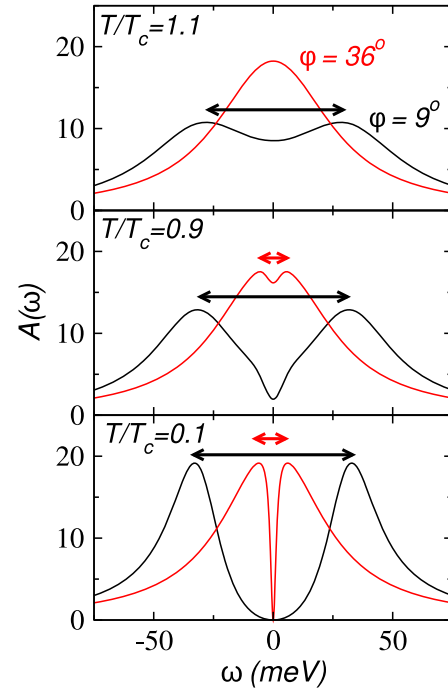

FIG. 29. Calculated spectral function $A(\omega, \varphi)$ at $T/T_c = 1.1, 0.9$, and 0.1 (from top to bottom) for $\varphi = 9°$ (black lines) and $\varphi = 36°$ (red lines). The black and red arrows indicate the size of the spectral gap, which is measured in ARPES. The angle φ is defined in Fig. 31. From Chien *et al.*, 2009.

the fermionic spectral function is more dramatic in the nodal region, where there is no normal-state background gap already present. By contrast, in the antinodal region the onset of Δ_{sc} on top of a large Δ_{PG} has little impact. Thus, as illustrated later in the review, it is the temperature dependence of the nodal gap that reflects the onset of the ordered state.

More quantitatively, one defines the spectral (or ARPES) gap as one-half of the peak-to-peak separation in the spectral function (Chen and Levin, 2008; Chien *et al.*, 2009). Figure 29 illustrates the temperature evolution of the spectral function for $\varphi = 9°$ (close to the antinodes in Fig. 31) and $\varphi = 36°$ (close to the nodes) at varying T/T_c from top to bottom. Above T_c (top panel of Fig. 29) the well understood behavior (Chubukov *et al.*, 2007; Norman *et al.*, 2007; Kanigel *et al.*, 2008) sets the stage for the normal phase that underlies the superconducting state in the middle and bottom panels of Fig. 29. At this temperature ($T/T_c = 1.1$), one sees Fermi arcs in the Brillouin zone. Here the spectral function is gapless on the Fermi surface near the nodal direction, while it is gapped in the vicinity of the antinodal direction. The Fermi arcs derive from the presence of a temperature-independent broadening term γ in Σ_{PG}. When T is slightly below T_c (middle panel of Fig. 29), a dip in the spectral function at $\varphi = 36°$ suddenly appears at $\omega = 0$. At this φ the underlying normal state is gapless, so the onset of the additional component of the self-energy via Σ_{sc} with long-lived pairs leads to the opening of a spectral gap.

By contrast, the presence of this order parameter is not responsible for the gap near the antinodes ($\varphi = 9°$), which
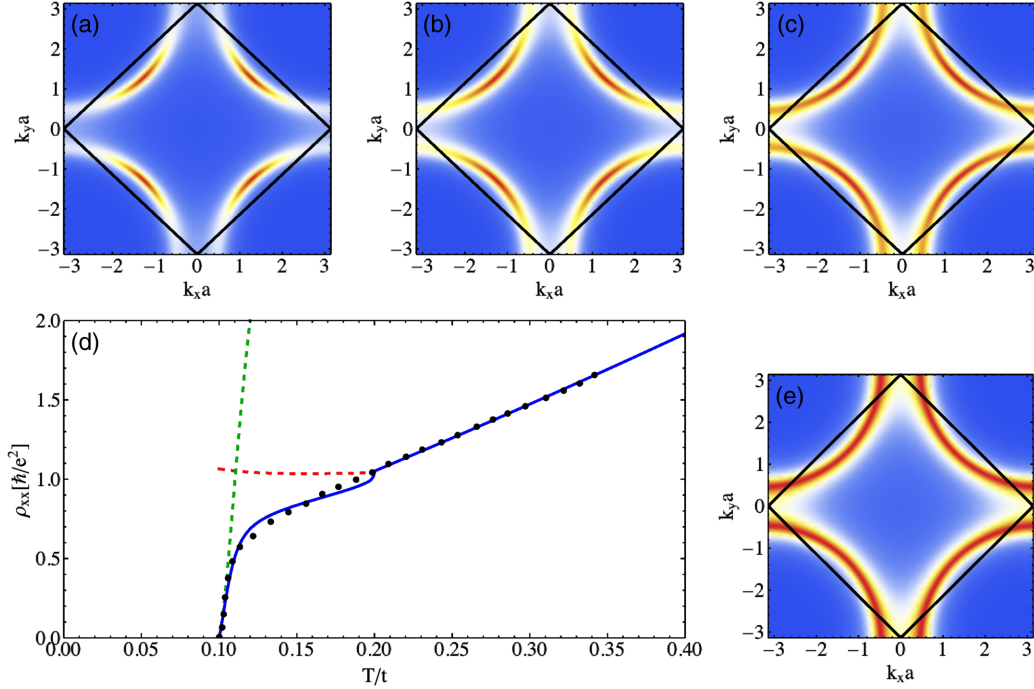
FIG. 30. Calculated behavior of the cuprate resistivity and temperature evolution of the Fermi arcs. Bad-metal behavior is important here, as the small conductivity in the fermionic channel enables the bosonic downturn in the resistivity to be more evident. (a)–(c), (e) Representative spectral function $A(\omega = 0, \mathbf{k})$ for temperatures T/t equal to (a) 0.11, (b) 0.15, (c) 0.18, and (e) 0.23. Here $T_c/t = 0.1$ and $T^*/t = 0.2$, where t is the nearest-neighbor hopping integral. (d) Experimental data for an underdoped $Bi_2Sr_2CaCu_2O_{8+\delta}$ indicated as black dots (Watanabe, Fujii, and Matsuda, 1997). The solid and dashed lines are theoretical fits. Solid blue line, calculated total ρ_{xx}; dashed red line (dashed dark-green line), fermionic (bosonic) contribution to ρ_{xx}. From Boyack *et al.*, 2021.

instead primarily derives from Δ_{PG}. Here the positions of the two maxima are relatively unchanged from their counterparts in the normal phase. Nevertheless, Δ_{sc} does introduce a sharpening of the spectral function associated with the deepening of the dip at $\omega = 0$. When $T \ll T_c$ (lower panel of Fig. 29), pairing fluctuations are small such that $\Delta(T) \approx \Delta_{sc}(T)$, and one returns to a conventional BCS-like spectral function with well-established gaps at all angles except at the precise nodes.

D. Transport in the cuprates

That the cuprates are highly resistive or bad metals is important for understanding their transport properties (Gunnarsson, Calandra, and Han, 2003). This is what allows the boson-related downturn of resistivity at T^*, a canonical signature of the pseudogap onset (Timusk and Statt, 1999), to become evident; see Fig. 30. This would otherwise be obscured by gap effects in the fermionic spectrum. The fits to the longitudinal dc resistivity shown in Fig. 30 are based on a phenomenological model (Boyack *et al.*, 2021) for the pair chemical potential (μ_{pair}) that incorporates the standard fluctuation behavior for $T \gtrsim T_c$ given by $\mu_{pair} \approx (8/\pi)(T_c - T)$. Here, however, one also includes T^* and higher temperature effects through a natural interpolation by associating T^* with the temperature where the number of pairs vanishes. This leads to the following consolidated form:

$$\mu_{pair} = \frac{8}{\pi}(T^* - T_c) \ln \frac{T^* - T}{T^* - T_c}. \tag{32}$$

This form for μ_{pair} leads to fits to the resistivity $\rho(T)$ and its downturn in Fig. 30 that are not unreasonable. Also emphasized here is the presence of "Fermi arcs," which additionally help to reveal bosonic transport by suppressing the gap in the fermionic spectrum. With the same parameters one can arrive at some understanding of the Nernst effect (Boyack *et al.*, 2021). However, there are problematic issues concerning the Hall coefficient (Geshkenbein, Ioffe, and Larkin, 1997; Boyack *et al.*, 2021) and the thermopower, which affect essentially all theoretical attempts to understand these cuprate data and make a direct comparison difficult between theory and experiment.

Indeed, there is a sizable literature dealing with the Hall coefficient in the underdoped regime (Rice *et al.*, 1991; Hwang *et al.*, 1994; Lang *et al.*, 1994; Samoilov, 1994; Jin and Ott, 1998; Konstantinovic, Li, and Raffy, 2000; Matthey *et al.*, 2001; Ando and Segawa, 2002; Segawa and Ando, 2004). Among the most serious problems is that the measured σ_{xy} does not appear to be as singular near T_c, as predicted by Gaussian pairing fluctuation theories, where the expected singularity is stronger than in σ_{xx}. This is presumably associated with the experimental observation that $R_H \propto \rho_{yx}$ starts to drop with decreasing T slightly above T_c (Lang *et al.*, 1994; Jin and Ott, 1998) and can even change its sign as T decreases toward T_c.
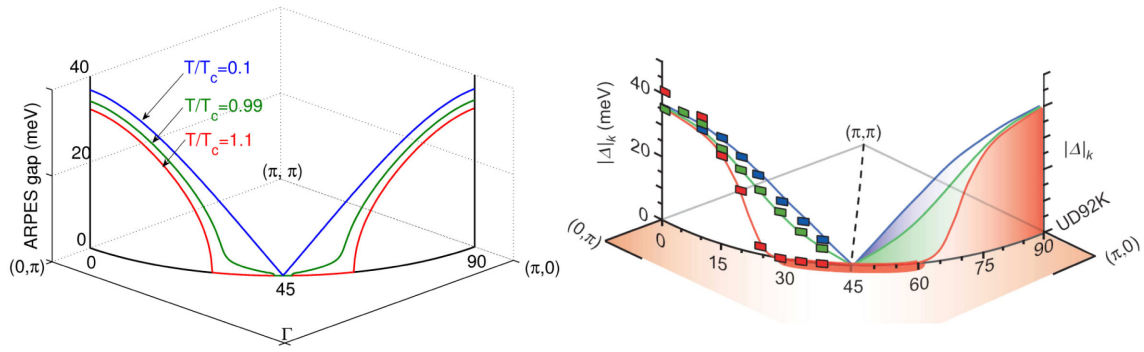
FIG. 31.   Inferred ARPES gaps as a function of **k** in one quadrant of the Brillouin zone. Fermi arcs (associated with *d*-wave pairing) appear on the Fermi surface near the nodal direction at around $\varphi = 45°$. Comparison of (left panel) theory (Chien *et al.*, 2009) with (right panel) experiment (Lee *et al.*, 2007).

Similarly, the normal-state thermopower in underdoped cuprates (Huang *et al.*, 1992; Munakata *et al.*, 1992; Fujii *et al.*, 2002; Badoux *et al.*, 2016; Cyr-Choinière *et al.*, 2017) (at $T \simeq T^*$) is positive in the experiments for the samples with the largest pseudogap. This is the opposite of the usual band-structure predictions and also the opposite of the sign of the Hall coefficient. Given these problems for the thermopower and Hall coefficients, comparisons between experiments are best addressed in the case of the Nernst coefficient.

E. Quantifying the Fermi arcs

Understanding and quantifying the Fermi arcs has become an important issue in the cuprates. In addition to ARPES experiments, the existence of Fermi arcs appears to have been independently established in STM data as well (Lee *et al.*, 2009; Pushp *et al.*, 2009). The right panel of Fig. 31 presents gaps extracted from ARPES data (Lee *et al.*, 2007) for a moderately underdoped sample. The three curves correspond to three different temperatures with the same legend as that in the left panel (representing the results of theory). One sees a pronounced temperature dependence in the behavior of the
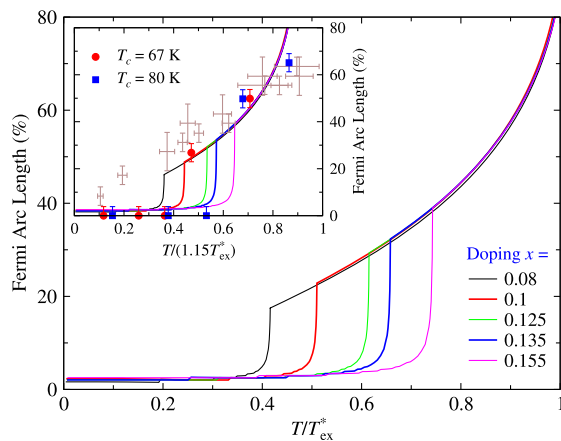

FIG. 32.   ARPES comparisons in cuprates showing the collapse of the Fermi arcs at the superconducting transition. Experimental data points (Kanigel *et al.*, 2007) are compared to theoretical curves (Chen and Levin, 2008). T_{ex}^* is the experimental T^* determined by ARPES data.

ARPES spectral gap for the nodal region (near 45°) compared to the antinodal region (near 0° and 90°), where there is virtually no T dependence. The left panel of Fig. 31 presents the corresponding theoretically predicted behavior, which exhibits some similarities.

Figure 32 addresses the temperature dependence of the Fermi arcs and their sharp collapse from above to below T_c (Chen and Levin, 2008). Note that here it is assumed for simplicity that the broadening parameter γ is temperature independent, as the noncondensed pairs, which persist below T_c, continue to be distinguished from the condensate there. Plotted is the percentage of arc length as a function of T/T^* and for different doping concentrations from the optimal to the underdoped regime. There is a clear universality seen in the normal state in both theory and experiment (shown in the inset) (Kanigel *et al.*, 2007).

F. Behavior of the finite-ω conductivity

There is substantial interest in the complex ac conductivity $\sigma(\omega) = \sigma_1(\omega) + i\sigma_2(\omega)$ in the cuprates, notably both in the optical regime and at terahertz frequencies (Basov and Timusk, 2005; Bilbro *et al.*, 2011). These experiments are particularly useful as they can reveal important information about low-energy excitations and charge dynamics. Both gapped fermions and noncondensed Cooper pairs can contribute to $\sigma(\omega)$. In theoretical work summarized here, only the fermionic contributions were considered, which might reasonably be viewed as a shortcoming.

A key feature of the in-plane $\sigma_1(\omega)$ is its two component nature consisting of a "coherent," Drude-like low-ω feature followed by an approximately T-independent midinfrared (MIR) peak (Santander-Syro *et al.*, 2004; Basov and Timusk, 2005; Lee *et al.*, 2005). This is illustrated in Fig. 33. As Lee *et al.* (2005) stated: "The two component conductivity extends to the pseudogap boundary in the phase diagram…. Moreover a softening of the mid-infrared band with doping resembles the decrease of the pseudogap temperature T^*." Also of importance is the fact (Kamarás *et al.*, 1990) that "high T_c materials are in the clean limit" and also that "… the MIR feature is seen above and below T_c." Thus, it appears that this MIR feature is not associated with disordered superconductivity and related momentum nonconserving processes, but rather is due to the
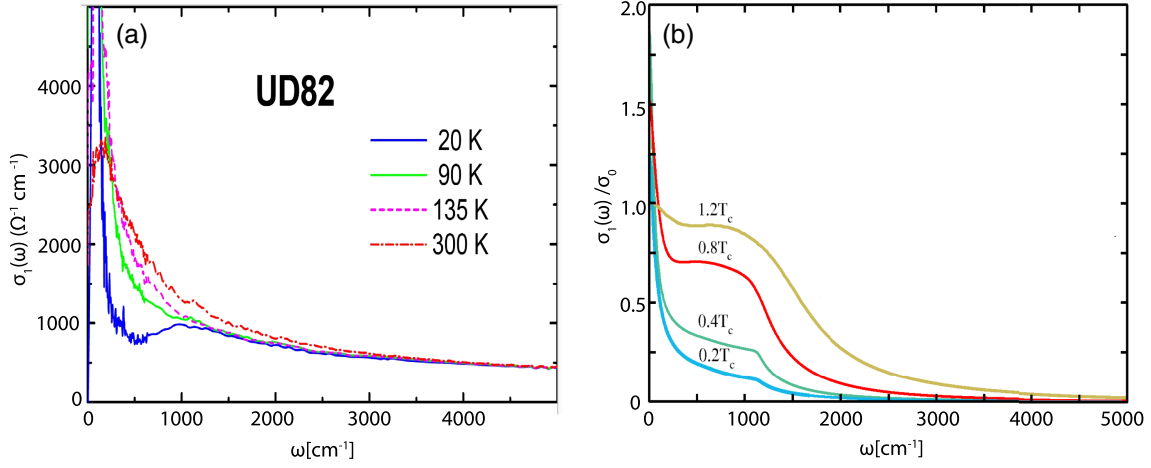
FIG. 33.   Midinfrared conductivity plots in cuprates showing experiment (left panel) (Hwang, Timusk, and Gu, 2007) and theory (right panel) (Wulin *et al.*, 2012) for an underdoped (UD) Bi2212 superconductor with $T_c = 82$ K. Both the theory and experimental panels show the real part of the frequency-dependent conductivity $\sigma_1(\omega)$ at different indicated temperatures. The midinfrared peak is presumed to be associated with the presence of a pseudogap.

unconventional nature of the finite-frequency response (Basov and Timusk, 2005).

Within the crossover scenario, the presence of noncondensed pairs both above and below T_c yields a midinfrared peak. This peak occurs around the energy needed to break pairs and thereby create conducting fermions (Wulin *et al.*, 2012). Its position is doping dependent, and only weakly temperature dependent, following the weak T dependence of the excitation gap $\Delta(T)$. As T decreases below T_c, the relatively high frequency spectral weight from these pseudogap effects present in the normal phase is transferred to the condensate. This leads to a narrowing of the low-ω Drude feature, as can be seen in both panels of Fig. 33.

Figure 34 shows the theoretical prediction (Wulin and Levin, 2012) and experimental behavior (Bilbro *et al.*, 2011) found for the imaginary part of the terahertz conductivity $\sigma_2(\omega)$ in the right and left panels, respectively. With decreasing temperature, at roughly T_c, σ_2 shows a sharp upturn at low ω of the form $\sigma_2 \propto n_s/\omega$, where n_s is the

superfluid density. The low-ω contribution above T_c is of interest to the extent that it may reflect the presence of dynamical superfluid correlations. This is shown in the insets, which present an expanded view of the temperature dependencies near T_c. Both theory and experiment show that the nesting of the σ_2 vs T curves switches order above T_c. We emphasize that for this class of experiments the contribution from preformed pairs does not extend to high temperatures. Indeed, here the effects are confined to temperatures in the vicinity of T_c, well below T^*. This is in contrast to other fluctuation experiments. It is notable that the experimental data show a more pronounced normal-state contribution than found in theory.

G. Precursor diamagnetism

The normal-state diamagnetic susceptibility in cuprates has also been widely discussed (Li *et al.*, 2010). Here, in contrast to the previous discussion surrounding $\sigma(\omega)$, the interest is
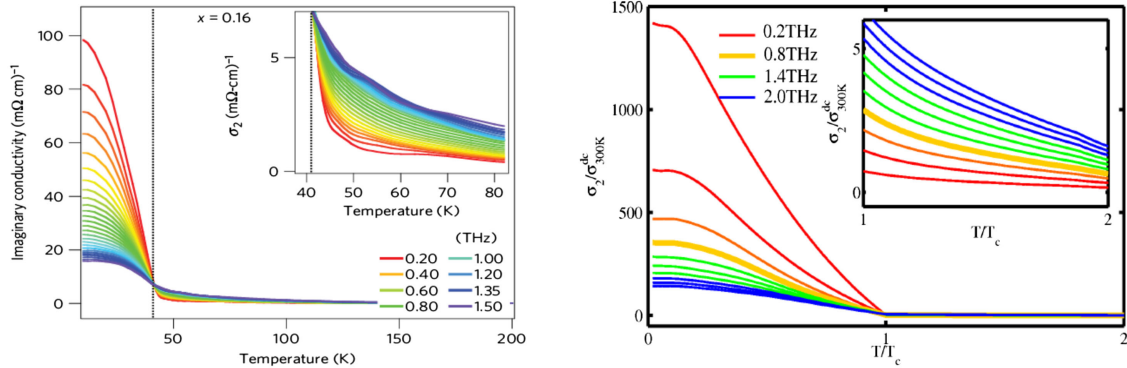
FIG. 34.   Comparison of the behavior of the imaginary part of the terahertz conductivity (σ_2) in cuprates at different frequencies as a function of temperature. Left panel: experimental data at optimal doping ($x = 0.16$) . Right panel: theory at optimal doping. A moderately large normal-state σ_2 is thought to reflect the presence of a dynamical or fluctuating superfluid density. For this reason there are enhanced plots of the normal-state regions in both insets accompanying both plots. Left panel: From Bilbro *et al.*, 2011. Right panel: From Wulin and Levin, 2012.

FIG. 35. Comparison of the behavior of the diamagnetic response above T_c between (a) experiment and (b) theory. In (b), the black 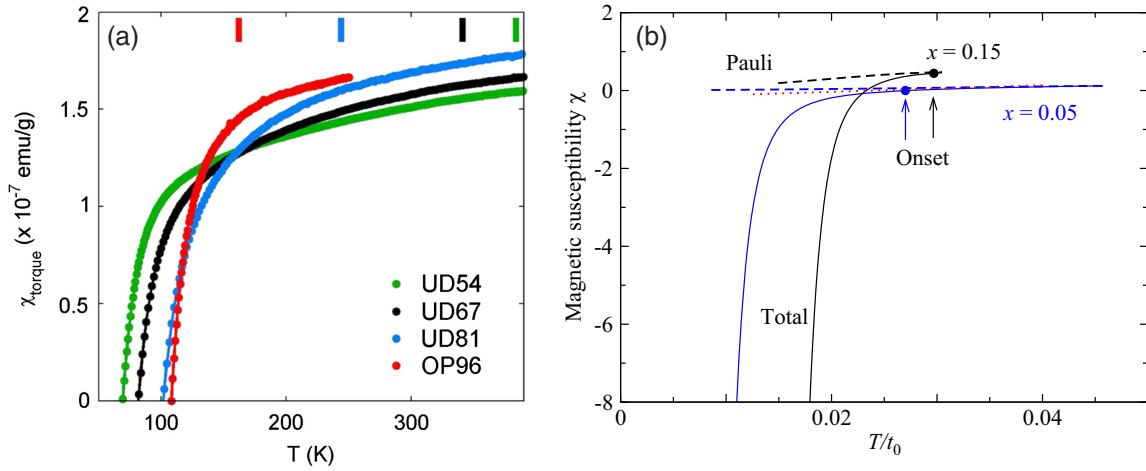curve for optimal hole doping ($x = p = 0.15$) and the blue curve for an underdoped system are labeled. The dashed lines are the Pauli paramagnetic susceptibility for each, while the solid lines are the sum of the paramagnetic and diamagnetic contributions. The solid dots in (b) indicate the temperature where the onset of the diamagnetism occurs. For the underdoped case the red dotted lines are a linear fit to the high-temperature data. (a) From G. Yu *et al.*, 2019. (b) From Boyack *et al.*, 2018.

focused on the bosonic contributions. In conventional fluctuation theory (Larkin and Varlamov, 2009) the diamagnetic susceptibility $\chi_{\rm dia}$ in the vicinity of $T \approx T_c$ can be relatively large, as it scales in three dimensions as $1/\sqrt{T - T_c}$. What happens in BCS-BEC crossover theory as a consequence of the presence of a pseudogap? In a BCS-BEC crossover scenario $\chi_{\rm dia}$ now scales (Boyack *et al.*, 2018) as $\sqrt{1/|\mu_{\rm pair}|}$ and, as seen in Eq. (32), the principal effect is that the inverse pair chemical potential remains appreciable now for an extended range of temperatures well beyond the critical region around T_c and strictly vanishes only at T^*.

This in turn suggests that there are fluctuation contributions to the diamagnetism at relatively higher temperatures than are generally observed in conventional superconductors. Note, however, that the visibility of fluctuation diamagnetism depends on other background (generally paramagnetic) contributions, which are often difficult to quantify. A more detailed analysis leads to the results in Fig. 35, which compares experiment (G. Yu *et al.*, 2019) and theory (Boyack *et al.*, 2018).

H. Other applications of BCS-BEC crossover: Features of the non-Fermi liquid

By way of completeness, we end by including several other contributions from the literature that address BCS-BEC crossover theory in cuprates but for which there are no direct back-to-back experimental comparisons. These involve studies of how the non-Fermi-liquid pseudogap state is reflected in quasiparticle-interference (QPI) experiments (Wulin *et al.*, 2009) based on STM probes, and how it is reflected in quantum oscillations (Scherpelz, He, and Levin, 2013). In particular, it was found that the observation of a QPI pattern consistent with the so-called octet model is a direct signature of coherent superconducting order (Kohsaka *et al.*, 2008). It appears from theory that the QPI pattern in the pseudogap

state (Wulin *et al.*, 2009) is distinctly different than that in the superconducting phase.

IX. CONCLUSIONS

A. Summary

This review was written in response to the large and relatively recent experimental literature on strongly correlated superconductors that are thought to exhibit BCS-BEC crossover phenomena. Many of these derive from artificial materials such as magic-angle twisted bilayer and trilayer graphene, quantum Hall bilayers, or ionic-gate-tuned semiconductors, as well as single unit cell and interfacial superconducting films. Also interesting are naturally grown superconductors such as Fe chalcogenides and the organic superconductor κ-$({\rm BEDT\text{-}TTF})_4 {\rm Hg}_{2.89} {\rm Br}_8$.

Because of the widespread interest, it is important to establish more precisely what BCS-BEC crossover theory is and what it is not. We have done so in this review and in the process have clarified distinctions between the Fermi-gas and solid-state superconductors, between two- and three-dimensional materials, and between s- and d-wave order parameter symmetries. We have also established distinguishing features of the BEC phase.

More generally, in this review and in the context of different experiments, we have addressed the three distinct ways of promoting a system out of the BCS and into the crossover regime via (i) small electronic kinetic energy scales, (ii) two dimensionality, or (iii) strong pairing glue. We have emphasized that superconducting "domes" and pseudogaps are ubiquitous for crossover systems in periodic lattices.

The narrative arc of this review is encapsulated through the evolution from Fig. 1 to Fig. 36, which we now discuss. Figure 1 introduced the concept of BCS-BEC crossover by raising the question of how to treat superconductivity in the presence of progressively stronger attractive interaction
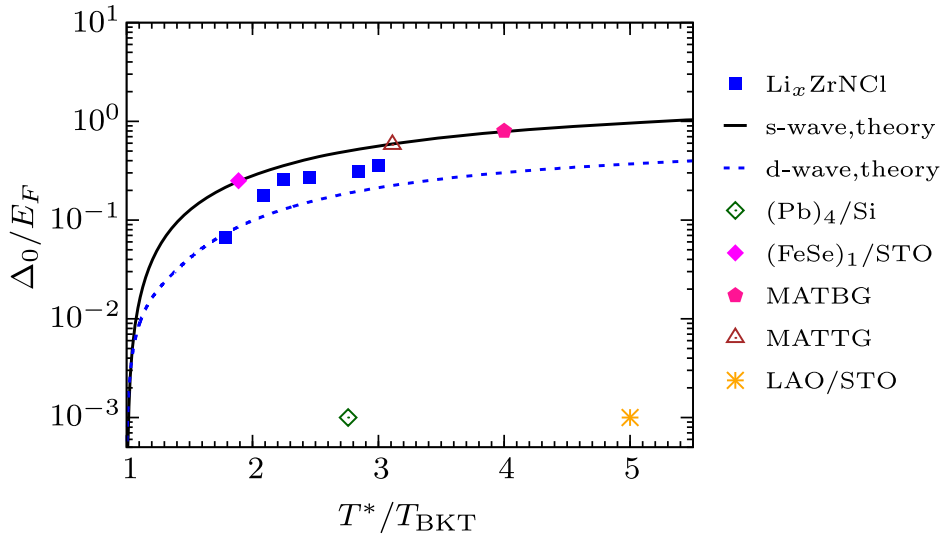
FIG. 36. Summary comparison between 2D BCS-BEC crossover theoretical predictions and experimental systems discussed in this review. The two theoretical curves correspond to *s*- and *d*-wave pairing results obtained for a square lattice. On the vertical axis, the value of Δ_0 is assumed to be at $T = 0$. The data points (see Appendix A) come from experiments on the lithium-intercalated nitride films (Nakagawa *et al.*, 2021), one unit cell FeSe on strontium titanate (Faeth *et al.*, 2021), and magic-angle twisted bilayer and trilayer graphene (Cao *et al.*, 2018; Oh *et al.*, 2021; Park *et al.*, 2021; Kim *et al.*, 2022). Two additional datasets are associated with strongly disordered Pb films (Zhao *et al.*, 2013) and those from the interface superconductor LaAlO$_3$SrTiO$_3$ (Božović and Levy, 2020). Among these the disordered Pb films are not related to BCS-BEC crossover, nor are the LaAlO$_3$/SrTiO$_3$ films, which also appear to be subject to disorder (Chen *et al.*, 2018). This figure suggests a clear separation between superconductors that are compatible with BCS-BEC crossover physics and those that are not.

strengths. Notably, in contrast to the cold Fermi gases, solid-state experiments have little access to this interaction strength parameter.

Figure 36, which represents a summary of many of the various 2D superconducting materials discussed in this review, allows us to compare crossover theory and experiment. This is made possible by effectively representing the dimensionless interaction strength parameter in BCS-BEC crossover theory through dimensionless ratios of physically accessible parameters such as T^*/T_{BKT} and Δ_0/E_F. One could similarly consider $k_F \xi_0^{coh}$ in counterpart plots. All of these are strongly interconnected, and Fig. 36 indicates that their interdependencies are generally robust to variations in the pairing symmetry (here from *s* wave to *d* wave).

Plotted on the vertical axis in a logarithmic scale is Δ_0/E_F, where Δ_0 is the zero-temperature excitation gap, while on the horizontal axis in a linear scale T^*/T_{BKT} is plotted for two-dimensional superconductors. The upper (black) and lower (blue) theoretical curves are for *s*- and *d*-wave pairing symmetries, respectively. The data points come from the lithium-intercalated nitride films (Nakagawa *et al.*, 2021), from one unit cell FeSe on strontium titanate (Faeth *et al.*, 2021), and from magic-angle twisted bilayer as well as trilayer graphene (Cao *et al.*, 2018; Oh *et al.*, 2021; Park *et al.*, 2021; Kim *et al.*, 2022).

Two additional datasets are associated with strongly disordered Pb films (Zhao *et al.*, 2013) and from the interface superconductor LaAlO$_3$SrTiO$_3$ (Božović and Levy, 2020). In Fig. 36, because of their small Δ_0/E_F ratios, both are distinct from BCS-BEC crossover candidate

materials. A comparison of theory and experiment in this replotting thus highlights the distinction between strong pairing and strong disorder. In this way, Fig. 36 serves as a template for helping to identify BCS-BEC crossover systems. The existence of a pseudogap (through the deviation of T^*/T_c from unity), as well as observations of 2*e* pairing, appears to be insufficient.

Additionally, we have addressed the question of under what circumstances one should expect to reach the BEC regime for a solid-state superconductor. In general, in this regime, rather than a large transition temperature, one finds small magnitudes of T_c or T_{BKT}. This point has often been missed in the literature because the standard for the BCS-BEC crossover phase diagrams is based on Fermi-gas physics, where the BEC asymptote is large. This distinction is emphasized in Fig. 1.

In the BEC regime, all signs of a Fermi surface have disappeared. Thus far we have not been able to report any unambiguous evidence that candidate systems have reached the BEC regime. Some signatures of the BEC that we have previously invoked are that in this regime the character of the states within vortex cores is distinctly different (Chien, He *et al.*, 2006). Similarly, in this regime coherence peaks in the quasiparticle tunneling characteristics will be absent. Theoretical indications are that a BEC superconductor can occur when either T^*/T_{BKT} is much larger (say, of the order of 10), accompanied by more conventional values of Δ_0/E_F, or alternatively with Δ_0/E_F of the order of 10 or more, accompanied by more conventional values of T^*/T_{BKT}. The latter relates to the interesting scenario in which

superconductivity occurs in the presence of flat energy bands with nontrivial band topology and quantum geometry.

We emphasize that establishing a given superconductor as belonging to the crossover regime can be done through a two-parameter analysis (both Δ_0/E_F and T^*/T_c must be moderately large, as in Fig. 36) or through a one-parameter analysis by showing that $k_F\xi_0^{\mathrm{coh}}$ is moderately small but in excess of the lower bounds set by Eqs. (29) and (30). These bounds arise because the dimensionless coherence length is readily quantified in terms of a fundamental variable of crossover physics: the normalized pair density n_{pair}/n at the transition temperature. This necessarily varies continuously from 0 in the strict BCS limit to exactly 1/2 (discounting small thermal effects) in the BEC regime, where $k_F\xi_0^{\mathrm{coh}}$ saturates. As discussed in this review, such a compact expression for the coherence length follows from the Schafroth-like equation for T_c in Eq. (3). We note that k_F here reflects the fixed density of electrons in the superconductor, and thus does not contain many-body effects or other band-structure complexities. Finally, it is most gratifying that experiments studying superconductivity in the solid state (as distinct from cold gases) have access [albeit with some uncertainty (Suzuki and Hikita, 1991)] to this parameter, as outlined in Sec. VII.

B. Outlook

More generally, in looking toward the future we are poised at the beginning of an extremely interesting era where the development of synthetic superconductors seems limitless. Tunable 2D superconductors [such as MATBG (Cao *et al.*, 2018; Oh *et al.*, 2021), MATTG (Park *et al.*, 2021; Kim *et al.*, 2022), Li$_x$ZrNCl (Nakagawa *et al.*, 2021), etc.] are likely candidates for realizing superconductivity in the strong-coupling regime. The coupling strength and Fermi energy can be dramatically and precisely tuned by twisting, gating, and doping, which provides the best platform to observe BCS-BEC crossover physics and to compare with theory.

This review can serve as a blueprint for future experimental endeavors, as it establishes concrete, experimentally falsifiable criteria to determine whether a given superconductor is in the BCS-BEC crossover regime. A singular observation of only the pseudogap phase or pairing above T_c no longer suffices. Future experimental studies will need to combine measurements of Δ, E_F, T^*, and T_c or T_{BKT} to place candidate materials on Fig. 36. Critical tests will be to perform these measurements with a continuous tuning parameter (gating, doping, twisting, or isovalent substitution) to enable a comparison between theory and experiment in an extended region of Fig. 36. An example of such complete studies is the work on Li$_x$ZrNCl summarized by Nakagawa *et al.* (2021).

We note that other tunable 2D superconductors such as twisted transition metal dichalcogenides can also host flat bands (Devakul *et al.*, 2021; Li *et al.*, 2021) and should be viewed as future candidates for superconductivity in the BCS-BEC crossover regime. It has also been predicted that nonequilibrium optical driving on twisted bilayer graphene can induce flat-band behavior associated with an effective Floquet Hamiltonian (Assi *et al.*, 2021); this provides a route toward the strong-coupling limit. The implications of the BCS-BEC crossover scenario in a general nonequilibrium context will be important to address. Ultrafast spectroscopic experiments should more generally be explored to characterize this band-structure engineering and its potentially new forms of superconductivity.

Additionally, the study of high-T_c Fe-based superconductors will lead to new opportunities and challenges to explore the connection between the BCS-BEC crossover physics, high-T_c superconductivity, and topological superconductivity. We note that the disparity between the transport T_c (~ 40 K) and the spectroscopic T^* (~ 70 K) has been a fundamental issue undermining further progress on monolayer FeSe/SrTiO$_3$ systems (Faeth *et al.*, 2021). This review can serve as the starting point to systematically explore crossover physics for understanding this interesting 2D high-T_c superconductor. A systematic tuning experiment using gating, doping, or Se:Te substitution will need to be performed. With a specific Se:Te ratio of $x:1-x$ between $x = 0.45$ and 0.55, the FeTe$_{1-x}$Se$_x$ bulk system exhibits a nontrivial topology with a superconducting topological surface state (Zhang *et al.*, 2018). It remains to be seen what the role of this topology will be in crossover physics.

Among new theoretical challenges, BCS-BEC crossover theories of superconductivity will need to accommodate the effect of magnetic fields, which will complete understanding of the canonical superconducting phase diagrams. What is the nature of the noncondensed pairs in the presence of a magnetic field (Scherpelz *et al.*, 2013)? How does condensation proceed when the dimensions of the system are effectively reduced by the presence of Landau levels (Schafroth, 1955; Lee and Shenoy, 1972), and how does one understand the dynamics of vortices from BCS to BEC (Mozyrsky and Chubukov, 2019)? Conceptually related is the central and difficult issue: How to generalize the Bogoliubov–de Gennes equations to the crossover situation at finite temperature. This would enable other important calculations, for example, those describing Andreev tunneling, the effects of proximitization, and how to address the vast number of situations that involve spatially dependent superconductivity. This is notably a difficult problem, as one needs to incorporate two distinct types of now spatially dependent gaps associated with condensed and noncondensed pairs.

In a discipline where theory and experiment work hand in hand, it is clear that the multiple experimental platforms described in this section collectively present enormous opportunities for future theoretical developments. In the process they enhance our understanding of this generalized BCS theory in a deeper and much broader sense.

LIST OF SYMBOLS AND ABBREVIATIONS

$\hbar$	(reduced) Planck constant
k_B	Boltzmann constant
c	speed of light
e	electron charge
E_F	Fermi energy
k_F	Fermi momentum
T_c	critical temperature for the (superfluid or superconducting) phase transition
T_{BKT}, T_φ	BKT transition temperature for (quasi-)2D superfluids
T^*, T_Δ, T_{pair}	pair formation or pseudogap onset temperature
T	temperature
μ	fermionic chemical potential
μ_{pair}	pair chemical potential
μ_B	bosonic chemical potential
μ_N	normal-state fermion chemical potential (which could be extrapolated down to $T = 0$)
Δ	fermionic excitation gap
Δ_{sc}	superconducting or superfluid order parameter
Δ_{PG}	pseudogap
Δ_{BCS}	mean-field gap obtained from BCS theory
$\Delta_0 \equiv \Delta(T = 0)$	zero-temperature gap
four-vector $k \equiv (i\omega_n, \mathbf{k})$	$\sum_k \equiv T\sum_n\sum_{\mathbf{k}}$, where $\omega_n = (2n + 1)\pi k_B T/\hbar$ is the odd (fermionic) Matsubara frequency, with $n \in \mathbb{Z}$
four-vector $q \equiv (i\Omega_l, \mathbf{q})$	$\sum_q \equiv T\sum_l\sum_{\mathbf{q}}$, where $\Omega_l = 2l\pi k_B T/\hbar$ is the even (bosonic) Matsubara frequency, with $l \in \mathbb{Z}$
$f(x) = 1/(e^{x/k_B T} + 1)$	Fermi-Dirac distribution function
$b(x) = 1(e^{x/k_B T} - 1)$	Bose-Einstein distribution function
$G(k)$, $G_0(k)$	full and bare Green's functions for fermions
$\Sigma(k)$	self-energy of fermions
$\Sigma_{sc}(k)$	superconducting self-energy of fermions
$\Sigma_{PG}(k)$	pseudogap self-energy of fermions
$\chi(q)$	pair susceptibility
$t(q)$	t matrix
$U < 0$	strength of the attractive interaction between fermions
U_c	critical interaction strength at which the two-body scattering length diverges in free space or, more generally, the strength at which a bound state starts to emerge
$V_{\mathbf{k},\mathbf{k}'} = U\varphi_{\mathbf{k}}\varphi_{\mathbf{k}'}$	separable pairing interaction with a strength $U < 0$ and a symmetry factor $\varphi_{\mathbf{k}}$: for a contact potential or the attractive Hubbard model, $\varphi_{\mathbf{k}} = 1$; for the cuprates, $\varphi_{\mathbf{k}} = \cos k_x - \cos k_y$
E_{kin}	characteristic kinetic-energy scale, which can be taken to be half of the bandwidth at moderate density or E_F at low density
$\epsilon_{\mathbf{k}} = \mathbf{k}^2/2m$	bare fermion dispersion in free space, with $\hbar = 1$.
$\epsilon_{\mathbf{k}} = 2t(2 - \cos k_x - \cos k_y) + 4t'(1 - \cos k_x \cos k_y) + 2t_z(1 - \cos k_z)$	bare fermion dispersion in a quasi-2D square lattice, where t and t' are the nearest and next-nearest neighbor in-plane hopping integral, respectively, and t_z is the out-of-plane hopping integral; the lattice constants have been set to unity: $a = b = c = 1$
$\xi_{\mathbf{k}} = \epsilon_{\mathbf{k}} - \mu$	bare fermion dispersion measured from the chemical potential
$E_{\mathbf{k}}$	Bogoliubov quasiparticle dispersion
$u_{\mathbf{k}}^2 = (1/2)(1 + \xi_{\mathbf{k}}/E_{\mathbf{k}})$, $v_{\mathbf{k}}^2 = (1/2)(1 - \xi_{\mathbf{k}}/E_{\mathbf{k}})$	coherence factors as given in BCS theory

Ψ^{BCS}	ground-state BCS wave function
n	fermion number density
$p = 1 - n$ or $x = 1 - n$	hole-doping concentration (in cuprates)
$n_B \equiv n_{pair}$	fermion pair or boson number density
$M_B \equiv M_{pair}$	effective mass of fermion pairs or bosons
$N_{\mathbf{q}}/N$	quasicondensate fraction (in 2D Fermi-gas experiments)
ρ_s	superfluid phase stiffness having dimension $[n]/[m]$
a_s	*s*-wave interfermion scattering length
a_{2D}	2D *s*-wave interfermion scattering length
d	interparticle distance $\equiv d_{particle}$ (in MATBG and MATTG) and interlayer distance in the double-layer quantum Hall context
ξ_0^{coh}	GL coherence length
ξ_0	pair size
H_{c2}	upper critical field
B	magnetic-field strength
$\ell_B = \sqrt{\hbar/|eB|}$	magnetic length
$\Phi_0 = hc/|2e|$	flux quantum
ρ_{xx}	longitudinal resistivity
ρ_{xy}	transverse resistivity
R_H, R_{xy}	Hall resistance, transverse resistance
$R_{xx}^{counter}$	longitudinal counterflow resistance measured in the double-layer quantum Hall systems
R_{xy}^{drag}	Hall drag resistance
σ_1, σ_2	real and imaginary parts of the conductivity $\sigma(\omega)$
χ_{dia}	diamagnetic susceptibility
M_{dia}	diamagnetic response in magnetization
$\mathcal{D}_{pair}^{crit}$	critical value associated with the phase-space density of pairs for the BKT transition
$1/T_1$	nuclear spin-lattice relaxation rate
V_g, V_{gate}	gating voltage
ν	electronic band filling factor (in MATBG and MATTG)
θ	twist angle (in MATBG and MATTG)
3D	three-dimensional
2D	two-dimensional
1UC	one unit cell (thickness)
AL	Aslamazov-Larkin (theory)
AFM	antiferromagnetic
ARPES	angle-resolved photoemission spectroscopy
BCS	Bardeen-Cooper-Schrieffer (theory)
BEC	Bose-Einstein condensation
BKT	Berezinskii-Kosterlitz-Thouless (transition)
BSCCO, Bi2212	$Bi_2Sr_2CaCu_2O_{8+\delta}$
CF	composite fermion
dc	direct current
DMFT	dynamical mean-field theory
GL	Ginzburg-Landau (theory)
GP	Gross-Pitaevskii (equation)
LAO/STO	$LaAlO_3/SrTiO_3$ (interface)
LSCO, La214	$La_{1-x}Sr_xCuO_4$
LL	Landau level
MIR	midinfrared (conductivity)
MATBG (MATTG)	magic-angle twisted bilayer (twisted trilayer) graphene
meV	milli-electron volts

NMR	nuclear magnetic resonance
NSR	Nozières and Schmitt-Rink
OD	overdoped (cuprates)
PG	pseudogap
QMC	quantum Monte Carlo (simulations)
QPI	quasiparticle interference
rf	radio frequency (spectroscopy)
RPA	random phase approximation
TDGL	time-dependent Ginzburg-Landau (theory)
TMA	*t*-matrix approximation
SC	superconductor
SCTA	self-consistent *t*-matrix approximation
SI	superconductor-insulator (transition)
SIN	superconductor-insulator-normal metal (tunneling junction)
STM	scanning tunneling microscopy
STS	scanning tunneling spectroscopy
UD	underdoped (cuprates)
YBCO	$YBa_2Cu_3O_{7-\delta}$
Y123	$Y_{0.8}Ca_{0.2}Ba_2Cu_3O_{7-\delta}$
YRZ	Yang-Rice-Zhang (theory)
μSR	muon-spin resonance, rotation, or relaxation

APPENDIX A: EXPERIMENTAL DATA FOR 2D SUPERCONDUCTORS

In this appendix, we present in Table I the data collected for Fig. 36 from various sources. In the table, if T_{BKT} is not available, we use the corresponding T_c.

The sources of the data are as follows: for $(FeSe)_1/STO$, $\{T_{BKT}, T^*\}$ are from Faeth *et al.* (2021) and $\{\Delta_0, E_F\}$ are from Liu *et al.* (2012). For $(Pb)_4/Si$ the data for $\{T_{BKT}, T^*\}$ are from Zhao *et al.* (2013). To estimate Δ_0/E_F we use data from Zhang *et al.* (2010), whose sample was actually a monolayer Pb film on a Si substrate [$(Pb)_1/Si$]. We do not expect Δ_0/E_F to differ much between $(Pb)_4/Si$ and $(Pb)_1/Si$.

The data for Li_xZrNCl are from Nakagawa *et al.* (2021). For (001)LAO/STO we use data from Pai *et al.* (2018) for T_{BKT}, data from Richter *et al.* (2013) for $\{T^*, \Delta_0\}$, and data from

TABLE I. Experimental data collected for Fig. 36. We identify the low-temperature gap with Δ_0. For Li_xZrNCl, different rows are for different carrier densities. $(FeSe)_1/STO$, monolayer FeSe grown on the $SrTiO_3$ substrate; $(Pb)_4/Si$, four-monolayer Pb film grown on the Si substrate; (001) LAO/STO, (001)-oriented $LaAlO_3/SrTiO_3$ interface; MATBG, magic-angle twisted bilayer graphene; MATTG, magic-angle twisted trilayer graphene.

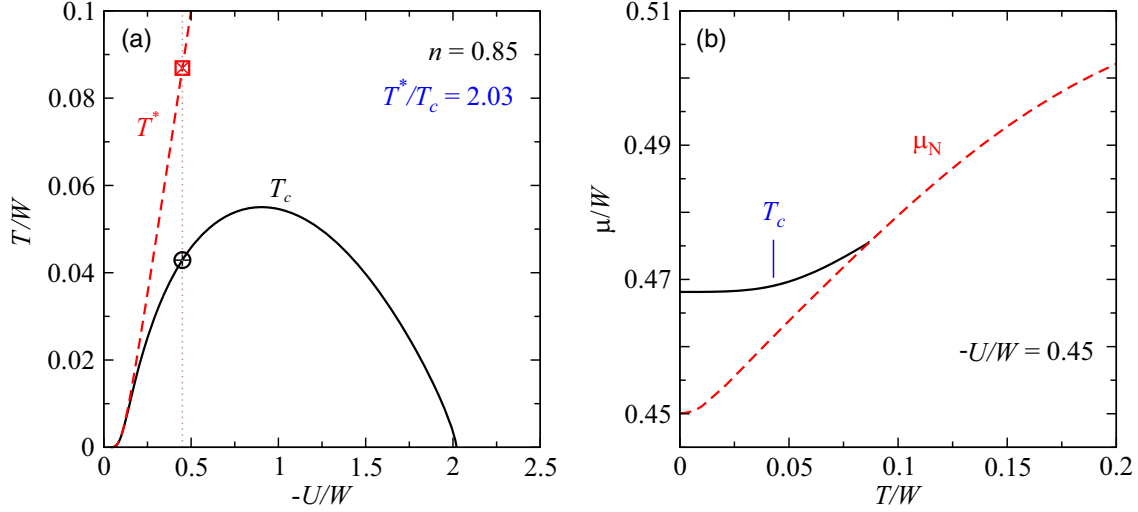| Materials	T_{BKT}	T^*	Δ_0	E_F	T^*/T_c	Δ_0/E_F
$(FeSe)_1/STO$	38 K	72 K	15 meV	60 meV	1.89	0.25
$(Pb)_4/Si$	2.4 K	6.9 K	0.35 meV	380 meV	2.9	0.001
(001) LAO/STO	100 mK	500 mK	65 μeV	47 meV	5	0.001
Li_xZrNCl	$0.031T_F$	$0.055T_F$	$\cdots$	$\cdots$	1.78	0.067
	$0.061T_F$	$0.13T_F$	$\cdots$	$\cdots$	2.1	0.18
	$0.088T_F$	$0.20T_F$	$\cdots$	$\cdots$	2.25	0.26
	$0.097T_F$	$0.24T_F$	$\cdots$	$\cdots$	2.45	0.27
	$0.10T_F$	$0.30T_F$	$\cdots$	$\cdots$	2.84	0.31
	$0.12T_F$	$0.35T_F$	$\cdots$	$\cdots$	3.0	0.36
MATBG	1.0 K	4 K	1.4 meV	20 K	4	0.8
MATTG	2.25 K	7 K	1.6 meV	32 K	3.1	0.58

FIG. 37. (a) $T_c - U$ phase diagram for a d-wave superconductor with electron density $n = 0.85$ on a quasi-2D square lattice. The energy dispersion is $\epsilon_{\mathbf{k}} = (4t + 4t' + 2t_z) - 2t(\cos k_x + \cos k_y) - 4t' \cos k_x \cos k_y - 2t_z \cos k_z$ with $t' = -0.3t$ and $t_z/t = 0.01$. All energies are normalized by $W = 4t$. The pairing gap is $\Delta_{\mathbf{k}} = \Delta \varphi_{\mathbf{k}}$, with $\varphi_{\mathbf{k}} = \cos k_x - \cos k_y$. (b) Temperature dependencies of the chemical potential μ and the extrapolated normal state μ_{N} for interaction strength $U/W = -0.45$, corresponding to the vertical dotted line in (a). We emphasize in (b) the small variations in the chemical potential. Here μ changes by -0.5% from $T = 0$ to the pairing onset T^*, and $(\mu - \mu_{\mathrm{N}})/\mu_{\mathrm{N}}$ is found to be 3.8% at $T = 0$.

Sulpizio *et al.* (2014) and Pai *et al.* (2018) for E_{F}. In this system we have used the d_{xy} orbital band to arrive at E_{F}, and the data collected all roughly correspond to the same gating voltage ($V_g \approx -100$ V).

The values of $\{T_{\mathrm{BKT}}, T^*, E_{\mathrm{F}}\}$ for MATBG are from Cao *et al.* (2018) for a twist angle $\theta \approx 1.05°$. Here T^* is estimated using the Ohmic recovery point from the V-I characteristic measurement, and Δ_0 was obtained from Oh *et al.* (2021). The latter was measured for a close but slightly different twist angle ($\theta \approx 1.01°$) system.

For MATTG we use data from Park *et al.* (2021) for T_{BKT} and data from Kim *et al.* (2022) for $\{T^*, \Delta_0\}$. The value of E_{F} was estimated by Stevan Nadj-Perge and was provided through a private communication.

APPENDIX B: GENERAL BCS-BEC CROSSOVER THEORY FOR d-WAVE CASE NEAR HALF FILLING

In this appendix, we present additional details about BCS-BEC crossover theory in the d-wave case, focusing on the region around half filling in the electron band. The results here are presumed to be generally appropriate to nodal superconductors in this half-filled regime where (as discussed in the text) a BEC is not accessible. In Appendix C, we address some aspects of cuprate experiments, but it is important not to confuse the phenomenological appendix with the more precise predictions that we present here.

For definiteness, we look at a typical band structure that happens to be used for cuprates (but otherwise is of no consequence). We take $\epsilon_{\mathbf{k}} = (4t + 4t' + 2t_z) - 2t(\cos k_x + \cos k_y) - 4t' \cos k_x \cos k_y - 2t_z \cos k_z$ with $t'/t = -0.3$. This band structure is more complicated than that used in the main text (for both s- and d-wave systems), as it has a van Hove singularity which is prominent for the band fillings

that we address. This is found to affect some properties of the crossover.

The goal of this appendix is to present the general behavior of the T^* and T_c phase diagrams and the associated properties of the chemical potential. The latter is useful to establish because it can in principle be measured. Moreover, the size of the fermionic chemical potential is often viewed as a measure of where a given system is in the crossover spectrum. By contrast, we emphasize here how improbable it is to find a solid-state superconductor anywhere near a BEC, unlike in the Fermi gases. As discussed in the main text, there are better indicators of crossover physics than

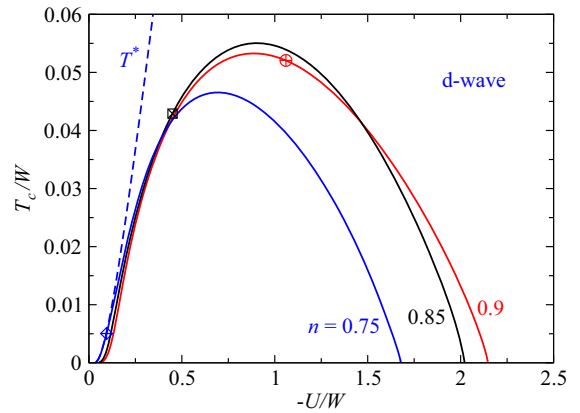FIG. 38. $T_c - U$ phase diagrams for quasi-2D d-wave superconductors with the same energy dispersion as in Fig. 37 computed for different electron densities $n = 1 - p$, where p is the hole doping. The symbols indicate where a given system (represented by the n value and T^*/T_c) is located in the corresponding experimental phase diagram (Hashimoto *et al.*, 2014). For clarity, we show the T^* line for $n = 0.75$ only.

TABLE II.   Changes in chemical potential associated with different values of T^*/T_c. Here $W = 4t$.

Hole doping	T^*/T_c	$\|U\|/W$	$\mu(T=0)/\mu_N(T=0)$
$p = 0.10$	4.73	1.06	1.09
$p = 0.15$	2.03	0. 45	1.04
$p = 0.25$	1.05	0.095	1.003

found in μ, for example, through the behavior of T^*/T_c and the coherence length.

Figure 37(a) plots a d-wave phase diagram at a hole concentration $p = 1 - n = 0.15$ as a function of the attractive coupling constant. Indicated are representative values of T^* and T_c. The solid line in Fig. 37(b) serves to characterize the behavior of the self-consistently determined fermionic chemical potential $\mu(T)$ for this particular interaction strength as a function of temperature T. The dashed line indicates the counterpart value of the extrapolated normal state $\mu_N(T)$, which is obtained by turning off the attraction. A crucial point follows by comparing Figs. 37(a) and 37(b), where we see that, although there is an appreciable separation between T^* and T_c, the chemical potential differs only slightly from its normal-state value (Sous, He, and Kivelson, 2023; Chen *et al.*, 2024).

Figure 38 presents the calculated phase diagrams for a range of hole concentrations near half filling. For reasons that later become clear, we choose T^*/T_c to be 4.7 to illustrate the behavior for a slightly lower hole doping $p = 0.1$, while $T^*/T_c = 1.05$ for a system with higher doping corresponding to $p = 0.25$. These two cases show the effects of increasing and decreasing the size of the pseudogap, respectively.

Table II summarizes some central findings. Here we tabulate results for all three hole-doping levels $p = \{0.1, 0.15, 0.25\}$, including the behavior of the chemical potentials. The table presents the ratios of the zero-temperature chemical potential μ to their normal-state counterparts. The difference from unity is small and, in the most extreme case, still less than 10%. From this comparison, one might view these systems as conventional BCS superconductors, but we emphasize that they all belong to the BCS-BEC crossover regime, as T_c and T^* are distinct.

APPENDIX C: IMPLICATIONS OF THE CUPRATE PHASE DIAGRAM AND ITS RELATION TO THE TWISTED GRAPHENE FAMILY

Whether any of the previous discussion is relevant to cuprates cannot be unequivocally established. But it is useful to explore what the consequences are if we assume the values of n and T^*/T_c chosen above and then establish the
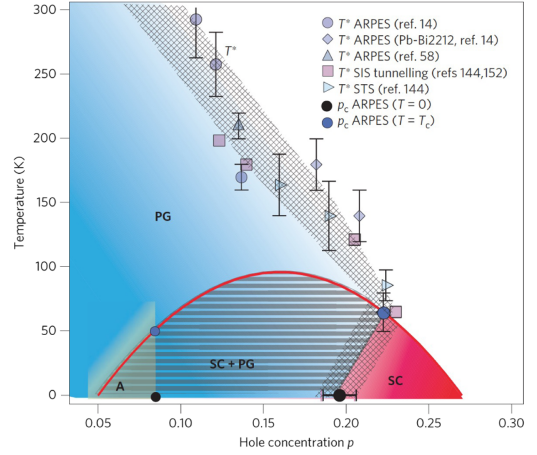
FIG. 39.   Experimental cuprate phase diagram. From Hashimoto *et al.*, 2014.

implications of this d-wave BCS-BEC crossover. Indeed, the correspondence between both of these parameters can be seen as reasonably compatible with the cuprate phase diagram shown in Fig. 39 (Hashimoto *et al.*, 2014). This compatibility of the parameter set assumes that the measured T^* is related to pairing.

We emphasize that there are complexities concerning this phase diagram that are still not fully settled. Among these is the observation of a second characteristic temperature (Vishik, 2018), which is not shown in Fig. 39. This temperature is typically about 20% above T_c, although significantly below T^* for heavily underdoped cuprates; this could be associated with the onset of a more extended fluctuation regime where bosonic transport derived from quasistable preformed pairs near condensation is significant. Here we focus only on the higher pseudogap temperature T^*. We emphasize that there is no unanimity as to whether one should associate the experimental T^* with pairing or an alternative energy scale, for example, deriving from possible ordering [for example, d-density wave (Chakravarty *et al.*, 2001)] or fluctuations in the particle-hole channel.

We view the ratio T^*/T_c and the corresponding density as input parameters. However, one test of the applicability of this theory comes from establishing the corresponding size of the electronic energy scales needed to match the size of the measured T_c and T^*, say, in kelvins. At issue are the hopping matrix elements, which determine the bandwidth and Fermi energy for each cuprate with a different hole concentration.

One could estimate that T_c/T_F is around 0.1 in the underdoped cuprates, as confirmed in Table III, where we present a more precise analysis. We emphasize that in the literature the observation that $T_c/T_F \approx 0.1$ is often

TABLE III.   Key parameters for hole-doped cuprates. In some sense these are near weak coupling, which reflects the fact that the cuprates T^*/T_c are not large, except at extreme underdoping. Here $\Delta_0 = 2\Delta$, which is the zero-temperature spectral gap $|\Delta_{\mathbf{k}}| = |\Delta(\cos k_x - \cos k_y)|$ at $(k_x, k_y) = (\pi, 0)$ as measured in ARPES.

Hole doping	T^* (K)	T_c (K)	T^*/T_c	t (meV)	$2\Delta_0/k_B T_c$	T_F (K)	T_c/T_F	$\|U\|$ (meV)
$p = 0.10$	260	55	4.73	22.7	25.9	502	0.11	96.4
$p = 0.15$	190	93	2.03	46.6	9.85	975	0.095	84.0
$p = 0.25$	32	30.6	1.05	130	4.28	2466	0.012	49.3

misinterpreted as representing the BEC limit of a Fermi gas. By contrast, the analysis here shows that this characteristic number is associated with a solid-state superconductor that is far from the BEC regime.

More specific cuprate parameters are presented in Table III, which indicates that the only adjustable parameter is the hopping parameter t, in the fifth column of the table. We note that this fitting suggests that the effective bandwidths will have to decrease as the system becomes more underdoped. Moreover, the attractive interaction U appears to become stronger as the insulator is approached. This should have some consequences for the origin of the pairing glue. The T_F values shown seem to be slightly smaller than those presented by Uemura (1997), but not by orders of magnitude. This remains an unsettled issue.

We note that, in a recent work (Harrison and Chan, 2022) that applied BCS-BEC crossover theory to cuprates, it was suggested that the cuprates with a "magic" ratio of $2\Delta_0/T_c = 6.5$ can be identified with the unitary point in a three-dimensional cold Fermi gas. This unitary point relates to the location of an isolated two-body bound state. However, as emphasized in this review, the superconducting phase diagrams of solid-state superconductors and Fermi gases are much different, making such an identification difficult to support. In particular, from Table III it follows that even at the optimal doping $p = 0.15$, we have $2\Delta_0/T_c = 9.85$, which is consistent with numbers obtained from photoemission experiments (He *et al.*, 2018). This value is larger than 6.5 and, on the basis of the analysis of the chemical potential (Table II), it follows that such systems are far from the BEC.

We end this review with a discussion of Fig. 40, which consolidates the results in Table III with those in Figs. 10 and 36. Figure 40 presents a combination of the key parameters associated with both MATBG and MATTG and a collection of counterpart data on the hole-doped cuprates. Indeed, one can see that the two graphene points are sandwiched between the

two most underdoped cuprates ($p = 0.10$ and 0.15). While it has been conjectured that MATBG bears a striking similarity to cuprates (Oh *et al.*, 2021), Figure 40 presents some quantitative evidence in support of this point.

REFERENCES

Abuki, H., and T. Brauner, 2008, Phys. Rev. D **78**, 125010.

Allen, S., and A.-M. S. Tremblay, 2001, Phys. Rev. B **64**, 075115.

Anderson, B. M., C.-T. Wu, R. Boyack, and K. Levin, 2015, Phys. Rev. B **92**, 134523.

Anderson, P. W., 1959, J. Phys. Chem. Solids **11**, 26.

Ando, Y., and K. Segawa, 2002, *J. Phys. Chem. Solids* 63, 2253.

Andrenacci, N., A. Perali, P. Pieri, and G. C. Strinati, 1999, Phys. Rev. B **60**, 12410.

Aslamazov, L. G., and A. I. Larkin, 1968, Sov. Phys. Solid State **10**, 875.

Aslamazov, L. G., and A. I. Larkin, 1975, Sov. Phys. JETP **40**, 321, http://jetp.ras.ru/cgi-bin/dn/e_040_02_0321.pdf.

Assi, I. A., J. P. F. LeBlanc, M. Rodriguez-Vega, H. Bahlouli, and M. Vogl, 2021, Phys. Rev. B **104**, 195429.

Badoux, S., *et al.*, 2016, Phys. Rev. X **6**, 021004.

Bardeen, J., L. N. Cooper, and J. R. Schrieffer, 1957, Phys. Rev. **108**, 1175.

Bartenstein, M., A. Altmeyer, S. Riedl, S. Jochim, C. Chin, J. H. Denschlag, and R. Grimm, 2004, Phys. Rev. Lett. **92**, 120401.

Basov, D. N., and T. Timusk, 2005, Rev. Mod. Phys. **77**, 721.

Bastiaans, K. M., *et al.*, 2021, Science **374**, 608.

Bauer, J., and A. C. Hewson, 2009, Europhys. Lett. **85**, 27001.

Berezinskii, V., 1972, Sov. Phys. JETP **34**, 610, http://jetp.ras.ru/cgi-bin/dn/e_034_03_0610.pdf.

Bilbro, L., R. V. Aguilar, G. Logvenov, O. Pelleg, I. Bozovic, and N. Armitage, 2011, Nat. Phys. **7**, 298.

Bloch, I., J. Dalibard, and W. Zwerger, 2008, Rev. Mod. Phys. **80**, 885.

Bonesteel, N. E., I. A. McDonald, and C. Nayak, 1996, Phys. Rev. Lett. **77**, 3009.

Bourdel, T., L. Khaykovich, J. Cubizolles, J. Zhang, F. Chevy, M. Teichmann, L. Tarruell, S. J. J. M. F. Kokkelmans, and C. Salomon, 2004, Phys. Rev. Lett. **93**, 050401.

Boyack, R., Q. J. Chen, A. A. Varlamov, and K. Levin, 2018, Phys. Rev. B **97**, 064503.

Boyack, R., X. Wang, Q. J. Chen, and K. Levin, 2019, Phys. Rev. B **99**, 134504.

Boyack, R., Z. Wang, Q. J. Chen, and K. Levin, 2021, Phys. Rev. B **104**, 064508.

Božović, I., and J. Levy, 2020, Nat. Phys. **16**, 712.

Cancellieri, C., M. L. Reinle-Schmitt, M. Kobayashi, V. N. Strocov, P. R. Willmott, D. Fontaine, P. Ghosez, A. Filippetti, P. Delugas, and V. Fiorentini, 2014, Phys. Rev. B **89**, 121412.

Cao, Y., V. Fatemi, S. Fang, K. Watanabe, T. Taniguchi, E. Kaxiras, and P. Jarillo-Herrero, 2018, Nature (London) **556**, 43.

Capone, M., C. Castellani, and M. Grilli, 2002, Phys. Rev. Lett. **88**, 126403.

Caviglia, A., S. Gariglio, N. Reyren, D. Jaccard, T. Schneider, M. Gabay, S. Thiel, G. Hammerl, J. Mannhart, and J.-M. Triscone, 2008, Nature (London) **456**, 624.

Chakravarty, S., R. B. Laughlin, D. K. Morr, and C. Nayak, 2001, Phys. Rev. B **63**, 094503.

Chand, M., G. Saraswat, A. Kamlapure, M. Mondal, S. Kumar, J. Jesudasan, V. Bagwe, L. Benfatto, V. Tripathi, and P. Raychaudhuri, 2012, Phys. Rev. B **85**, 014508.
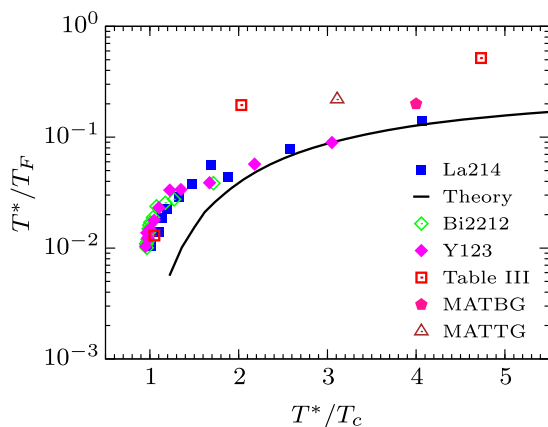
FIG. 40. Evidence supporting that cuprates may belong to the BCS-BEC crossover family and that cuprates and the two twisted graphene superconducting families MATBG and MATTG seem to be similar. The cuprate data of La214, Bi2212, and Y123 are the same as in Fig. 10. In the legend, "Table III" represents the additional two cuprate data points from Table III for hole doping $p = 0.1$ and 0.15. The solid line is the predicted behavior for a *d*-wave crossover superconductor.

Che, Y. M., J. B. Wang, and Q. J. Chen, 2016, Phys. Rev. A **93**, 063611.

Che, Y. M., L. F. Zhang, J. B. Wang, and Q. J. Chen, 2017, Phys. Rev. B **95**, 014504.

Chen, C., Q. Liu, W.-C. Bao, Y. Yan, Q.-H. Wang, T. Zhang, and D. Feng, 2020, Phys. Rev. Lett. **124**, 097001.

Chen, Q. J., 2000, Ph.D. thesis (University of Chicago) [arXiv:1801 .06266].

Chen, Q. J., 2012, Phys. Rev. A **86**, 023610.

Chen, Q. J., I. Kosztin, B. Jankó, and K. Levin, 1998, Phys. Rev. Lett. **81**, 4708.

Chen, Q. J., I. Kosztin, B. Jankó, and K. Levin, 1999, Phys. Rev. B **59**, 7083.

Chen, Q. J., and K. Levin, 2008, Phys. Rev. B **78**, 020513.

Chen, Q. J., K. Levin, and I. Kosztin, 2001, Phys. Rev. B **63**, 184519.

Chen, Q. J., J. Stajic, S. Tan, and K. Levin, 2005, Phys. Rep. **412**, 1.

Chen, Q. J., J. B. Wang, L. Sun, and Y. Yu, 2020, Chin. Phys. Lett. **37**, 053702.

Chen, Q. J., Z. Q. Wang, R. Boyack, and K. Levin, 2024, npj Quantum Mater. **9**, 27.

Chen, S.-D., *et al.*, 2019, Science **366**, 1099.

Chen, Z., *et al.*, 2018, Nat. Commun. **9**, 4008.

Cheng, G., *et al.*, 2015, Nature (London) **521**, 196.

Chien, C.-C., Q. J. Chen, Y. He, and K. Levin, 2006, Phys. Rev. Lett. **97**, 090402.

Chien, C.-C., H. Guo, Y. He, and K. Levin, 2010, Phys. Rev. A **81**, 023622.

Chien, C.-C., Y. He, Q. J. Chen, and K. Levin, 2006, Phys. Rev. A **73**, 041603.

Chien, C.-C., Y. He, Q. J. Chen, and K. Levin, 2009, Phys. Rev. B **79**, 214527.

Chin, C., M. Bartenstein, A. Altmeyer, S. Riedl, S. Jochim, J. H. Denschlag, and R. Grimm, 2004, Science **305**, 1128.

Chin, J. K., D. E. Miller, Y. Liu, C. Stan, W. Setiawan, C. Sanner, K. Xu, and W. Ketterle, 2006, Nature (London) **443**, 961.

Chubukov, A. V., I. Eremin, and D. V. Efremov, 2016, Phys. Rev. B **93**, 174516.

Chubukov, A. V., M. R. Norman, A. J. Millis, and E. Abrahams, 2007, Phys. Rev. B **76**, 180501.

Cladé, P., C. Ryu, A. Ramanathan, K. Helmerson, and W. D. Phillips, 2009, Phys. Rev. Lett. **102**, 170401.

Combescot, M., R. Combescot, and F. Dubin, 2017, Rep. Prog. Phys. **80**, 066501.

Combescot, M., W. Pogosov, and O. Betbeder-Matibet, 2013 Physica (Amsterdam) **485C**, 47.

Comte, C., and P. Nozières, 1982, J. Phys. (Paris) **43**, 1069.

Cyr-Choinière, O., *et al.*, 2017, Phys. Rev. X **7**, 031042.

Deisz, J., D. Hess, and J. Serene, 1998, Phys. Rev. Lett. **80**, 373.

Demler, E., W. Hanke, and S.-C. Zhang, 2004, Rev. Mod. Phys. **76**, 909.

Denteneer, P. J. H., G. An, and J. M. J. van Leeuwen, 1993, Phys. Rev. B **47**, 6256.

Deutscher, G., 2005, Rev. Mod. Phys. **77**, 109.

Devakul, T., V. Crépel, Y. Zhang, and L. Fu, 2021, Nat. Commun. **12**, 6730.

Diener, R. B., R. Sensarma, and M. Randeria, 2008, Phys. Rev. A **77**, 023626.

Dubouchet, T., B. Sacépé, J. Seidemann, D. Shahar, M. Sanquer, and C. Chapelier, 2019, Nat. Phys. **15**, 233.

Eagles, D. M., 1969, Phys. Rev. **186**, 456.

Eisenstein, J., 2014, Annu. Rev. Condens. Matter Phys. **5**, 159.

Eisenstein, J. P., L. N. Pfeiffer, and K. W. West, 2019, Phys. Rev. Lett. **123**, 066802.

Emery, V. J., and S. A. Kivelson, 1995, Nature (London) **374**, 434.

Engelbrecht, J. R., H. Zhao, and A. Nazarenko, 2002, J. Phys. Chem. Solids **63**, 2237.

Faeth, B. D., S.-L. Yang, J. K. Kawasaki, J. N. Nelson, P. Mishra, C. T. Parzyck, C. Li, D. G. Schlom, and K. M. Shen, 2021, Phys. Rev. X **11**, 021054.

Fillis-Tsirakis, E., C. Richter, J. Mannhart, and H. Boschker, 2016, New J. Phys. **18**, 013046.

Fisher, D. S., and P. C. Hohenberg, 1988, Phys. Rev. B **37**, 4936.

Fisher, M. P. A., 1990, Phys. Rev. Lett. **65**, 923.

Fujii, T., I. Terasaki, T. Watanabe, and A. Matsuda, 2002, Physica (Amsterdam) **378C–381C**, 182.

Fukushima, N., Y. Ohashi, E. Taylor, and A. Griffin, 2007, Phys. Rev. A **75**, 033609.

Fulde, P., and R. A. Ferrell, 1964, Phys. Rev. **135**, A550.

Garg, A., H. R. Krishnamurthy, and M. Randeria, 2005, Phys. Rev. B **72**, 024517.

Gariglio, S., M. Gabay, J. Mannhart, and J.-M. Triscone, 2015, Physica C (Amsterdam) **514**, 189.

Gasparov, V., A. Audouard, L. Drigo, X. He, and I. Bozovic, 2017, Int. J. Mod. Phys. B **31**, 1745016.

Ge, J.-F., Z.-L. Liu, C. Liu, C.-L. Gao, D. Qian, Q.-K. Xue, Y. Liu, and J.-F. Jia, 2015, Nat. Mater. **14**, 285.

Georges, A., G. Kotliar, W. Krauth, and M. J. Rozenberg, 1996, Rev. Mod. Phys. **68**, 13.

Geshkenbein, V. B., L. B. Ioffe, and A. I. Larkin, 1997, Phys. Rev. B **55**, 3173.

Ghiringhelli, G., *et al.*, 2012, Science **337**, 821.

Giorgini, S., L. P. Pitaevskii, and S. Stringari, 2008, Rev. Mod. Phys. **80**, 1215.

Greiner, M., C. A. Regal, and D. S. Jin, 2003, Nature (London) **426**, 537.

Gunnarsson, O., M. Calandra, and J. E. Han, 2003, Rev. Mod. Phys. **75**, 1085.

Guo, H., D. Wulin, C.-C. Chien, and K. Levin, 2011a, New J. Phys. **13**, 075011.

Guo, H., D. Wulin, C.-C. Chien, and K. Levin, 2011b, Phys. Rev. Lett. **107**, 020403.

Hadzibabic, A., P. Kruger, M. Cheneau, B. Battelier, and J. Dalibard, 2006, Nature (London) **441**, 1118.

Halperin, B., and D. R. Nelson, 1979, J. Low Temp. Phys. **36**, 599.

Halperin, B. I., 1983, Helv. Phys. Acta **56**, 75, https://www .e-periodica.ch/cntmng?pid=hpa-001:1983:56::1243.

Halperin, B. I., P. A. Lee, and N. Read, 1993, Phys. Rev. B **47**, 7312.

Han, S., C.-L. Song, X.-C. Ma, and Q.-K. Xue, 2021, C.R. Phys. **22**, 163.

Hanaguri, T., S. Kasahara, J. Böker, I. Eremin, T. Shibauchi, and Y. Matsuda, 2019, Phys. Rev. Lett. **122**, 077001.

Hardy, F., *et al.*, 2019, Phys. Rev. B **99**, 035157.

Harrison, N., and M. K. Chan, 2022, Phys. Rev. Lett. **129**, 017001.

Hashimoto, M., I. M. Vishik, R.-H. He, T. P. Devereaux, and Z.-X. Shen, 2014, Nat. Phys. **10**, 483.

Hashimoto, M., *et al.*, 2010, Nat. Phys. **6**, 414.

Hashimoto, T., *et al.*, 2020, Sci. Adv. **6**, eabb9052.

Haussmann, R., 1993, Z. Phys. B **91**, 291.

Haussmann, R., 1994, Phys. Rev. B **49**, 12975.

Haussmann, R., M. Punk, and W. Zwerger, 2009, Phys. Rev. A **80**, 063612.

Haussmann, R., W. Rantner, S. Cerrito, and W. Zwerger, 2007, Phys. Rev. A **75**, 023610.

Haussmann, R., and W. Zwerger, 2008, Phys. Rev. A **78**, 063602.

Hazra, T., N. Verma, and M. Randeria, 2019, Phys. Rev. X **9**, 031049.

He, L., X.-G. Huang, H. Hu, and X.-J. Liu, 2013, Phys. Rev. A **87**, 053616.

He, Y., *et al.*, 2018, Science **362**, 62.

Hebard, A. F., and M. A. Paalanen, 1990, Phys. Rev. Lett. **65**, 927.

Herbut, I. F., 2004, Phys. Rev. B **70**, 184507.

Hofmann, J. S., E. Berg, and D. Chowdhury, 2020, Phys. Rev. B **102**, 201112.

Hollen, S. M., H. Q. Nguyen, E. Rudisaile, M. D. Stewart, J. Shainline, J. M. Xu, and J. M. Valles, 2011, Phys. Rev. B **84**, 064528.

Hu, H., P. D. Drummond, and X.-J. Liu, 2007, Nat. Phys. **3**, 469.

Huang, D., R. Wang, W. Cai, G. Gu, Q. Shi, Y. Zhou, J. Fu, C. Huang, Y. Ruan, and Y. Zhang, 1992, Physica (Amsterdam) **199C**, 337.

Hueck, K., N. Luick, L. Sobirey, J. Siegl, T. Lompe, and H. Moritz, 2018, Phys. Rev. Lett. **120**, 060402.

Hufner, S., M. A. Hossain, A. Damascelli, and G. Sawatzky, 2008, Rep. Prog. Phys. **71**, 062501.

Hugenholtz, N. M., and D. Pines, 1959, Phys. Rev. **116**, 489.

Hwang, H. Y., B. Batlogg, H. Takagi, H. L. Kao, J. Kwo, R. J. Cava, J. J. Krajewski, and W. F. Peck, 1994, Phys. Rev. Lett. **72**, 2636.

Hwang, J., T. Timusk, and G. Gu, 2007, J. Phys. Condens. Matter **19**, 125208.

Imajo, S., S. Sugiura, H. Akutsu, Y. Kohama, T. Isono, T. Terashima, K. Kindo, S. Uji, and Y. Nakazawa, 2021, Phys. Rev. Res. **3**, 033026.

Jain, J. K., 2007, *Composite Fermions* (Cambridge University Press, Cambridge, England).

Jin, R., and H. R. Ott, 1998, Phys. Rev. B **57**, 13872.

Jochim, S. M. Bartenstein, A. Altmeyer, G. Hendl, S. Riedl, C. Chin, J. Hecker Denschlag, and R. Grimm, 2003, Science **302**, 2101.

José, J. V., 2013, Ed., *40 Years of Berezinskii-Kosterlitz-Thouless Theory* (World Scientific, Singapore).

Joseph, J. A., E. Elliott, and J. E. Thomas, 2015, Phys. Rev. Lett. **115**, 020401.

Kadanoff, L. P., and P. C. Martin, 1961, Phys. Rev. **124**, 670.

Kamarás, K., *et al.*, 1990, Phys. Rev. Lett. **64**, 84.

Kamburov, D., Y. Liu, M. A. Mueed, M. Shayegan, L. N. Pfeiffer, K. W. West, and K. W. Baldwin, 2014, Phys. Rev. Lett. **113**, 196801.

Kang, B. L., *et al.*, 2020, Phys. Rev. Lett. **125**, 097003.

Kanigel, A., U. Chatterjee, M. Randeria, M. R. Norman, G. Koren, K. Kadowaki, and J. C. Campuzano, 2008, Phys. Rev. Lett. **101**, 137002.

Kanigel, A., U. Chatterjee, M. Randeria, M. R. Norman, S. Souma, M. Shi, Z. Z. Li, H. Raffy, and J. C. Campuzano, 2007, Phys. Rev. Lett. **99**, 157001.

Kanoda, K., K. Miyagawa, A. Kawamoto, and Y. Nakazawa, 1996, Phys. Rev. B **54**, 76.

Kasahara, S., *et al.*, 2014, Proc. Natl. Acad. Sci. U.S.A. **111**, 16309.

Kasahara, S., *et al.*, 2016, Nat. Commun. **7**, 12843.

Keller, M., W. Metzner, and U. Schollwöck, 2001, Phys. Rev. Lett. **86**, 4612.

Khestanova, E., *et al.*, 2018, Nano Lett. **18**, 2623.

Kim, H., Y. Choi, C. Lewandowski, A. Thomson, Y. Zhang, R. Polski, K. Watanabe, T. Taniguchi, J. Alicea, and S. Nadj-Perge, 2022, Nature (London) **606**, 494.

Kinast, J., S. L. Hemmer, M. E. Gehm, A. Turlapov, and J. E. Thomas, 2004, Phys. Rev. Lett. **92**, 150402.

Kinast, J., A. Turlapov, J. E. Thomas, Q. J. Chen, J. Stajic, and K. Levin, 2005, Science **307**, 1296.

Koga, A., and P. Werner, 2011, Phys. Rev. A **84**, 023638.

Kohn, W., and D. Sherrington, 1970, Rev. Mod. Phys. **42**, 1.

Kohsaka, Y., *et al.*, 2008, Nature (London) **454**, 1072.

Kondo, T., W. Malaeb, Y. Ishida, T. Sasagawa, H. Sakamoto, T. Takeuchi, T. Tohyama, and S. Shin, 2015, Nat. Commun. **6**, 7699.

Konstantinovic, Z., Z. Z. Li, and H. Raffy, 2000, Phys. Rev. B **62**, R11989.

Kosterlitz, J. M., 2016, Rep. Prog. Phys. **79**, 026001.

Kosterlitz, J. M., and D. J. Thouless, 1973, J. Phys. C **6**, 1181.

Kovtun, P. K., D. T. Son, and A. O. Starinets, 2005, Phys. Rev. Lett. **94**, 111601.

Ku, M. J., A. T. Sommer, L. W. Cheuk, and M. W. Zwierlein, 2012, Science **335**, 563.

Kuchinskii, E., N. Kuleeva, and M. Sadovskii, 2015, J. Exp. Theor. Phys. **120**, 1055.

Kuchinskii, E., N. Kuleeva, and M. Sadovskii, 2016, J. Exp. Theor. Phys. **122**, 375.

Kugler, M., O. Fischer, C. Renner, S. Ono, and Y. Ando, 2001, Phys. Rev. Lett. **86**, 4911.

Lang, W., G. Heine, P. Schwab, X. Z. Wang, and D. Bäuerle, 1994, Phys. Rev. B **49**, 4209.

Larkin, A., and I. Ovchinnikov, 1965 Sov. Phys. JETP **20**, 762.

Larkin, A., and A. Varlamov, 2009, *Theory of Fluctuations in Superconductors*, revised ed. (Oxford University Press, Oxford).

Lee, J., K. Fujita, A. Schmidt, C. K. Kim, H. Eisaki, S. Uchida, and J. Davis, 2009, Science **325**, 1099.

Lee, P. A., N. Nagaosa, and X.-G. Wen, 2006, Rev. Mod. Phys. **78**, 17.

Lee, P. A., and S. R. Shenoy, 1972, Phys. Rev. Lett. **28**, 1025.

Lee, W.-S., I. Vishik, K. Tanaka, D. Lu, T. Sasagawa, N. Nagaosa, T. Devereaux, Z. Hussain, and Z.-X. Shen, 2007, Nature (London) **450**, 81.

Lee, Y. S., K. Segawa, Z. Q. Li, W. J. Padilla, M. Dumm, S. V. Dordevic, C. C. Homes, Y. Ando, and D. N. Basov, 2005, Phys. Rev. B **72**, 054529.

Leggett, A. J., 1980, in *Modern Trends in the Theory of Condensed Matter*, Lecture Notes in Physics Vol. 115, edited by A. Pekalski and J. A. Przystawa (Springer-Verlag, Berlin), pp. 13–27.

Leggett, A. J., 1996, Science **274**, 587.

Leggett, A. J., 2006, Nat. Phys. **2**, 134.

Leggett, A. J., 2012, in *Quantum Liquids*, edited by J. Ruvalds (Elsevier, New York).

Levin, K., Q. J. Chen, C.-C. Chien, and Y. He, 2010, Ann. Phys. (Amsterdam) **325**, 233.

Levin, K., and O. T. Valls, 1983, Phys. Rep. **98**, 1.

Li, H., *et al.*, 2021, Nat. Mater. **20**, 945.

Li, L., Y. Wang, S. Komiya, S. Ono, Y. Ando, G. D. Gu, and N. P. Ong, 2010, Phys. Rev. B **81**, 054510.

Li, X., *et al.*, 2024, Nature (London) **626**, 288.

Lin, N., E. Gull, and A. J. Millis, 2010, Phys. Rev. B **82**, 045104.

Liu, D., *et al.*, 2012, Nat. Commun. **3**, 931.

Liu, X., J. Li, K. Watanabe, T. Taniguchi, J. Hone, B. I. Halperin, P. Kim, and C. R. Dean, 2022, Science **375**, 205.

Liu, X. M., K. Watanabe, T. Taniguchi, B. I. Halperin, and P. Kim, 2017, Nat. Phys. **13**, 746.

Loh, Y. L., M. Randeria, N. Trivedi, C.-C. Chang, and R. Scalettar, 2016, Phys. Rev. X **6**, 021029.

Loktev, V. M., R. M. Quick, and S. G. Sharapov, 2001, Phys. Rep. **349**, 1.

Lu, X., *et al.*, 2019, Nature (London) **574**, 653.

Maly, J., 1997, Ph.D. thesis (University of Chicago).

Maly, J., B. Jankó, and K. Levin, 1999a, Physica (Amsterdam) **321C**, 113.

Maly, J., B. Jankó, and K. Levin, 1999b, Phys. Rev. B **59**, 1354.

Matsumura, Y., S. Yamashita, H. Akutsu, and Y. Nakazawa, 2022, Low Temp. Phys. **48**, 51.

Matthey, D., S. Gariglio, B. Giovannini, and J.-M. Triscone, 2001, Phys. Rev. B **64**, 024513.

McKenzie, R. H., 1997, Science **278**, 820.

McKenzie, R. H., 1998, Comments Condens. Matter Phys. **18**, 309 [arXiv:cond-mat/9802198].

Micnas, R., M. H. Pedersen, S. Schafroth, T. Schneider, J. J. Rodríguez-Núñez, and H. Beck, 1995, Phys. Rev. B **52**, 16223.

Micnas, R., J. Ranninger, and S. Robaszkiewicz, 1990, Rev. Mod. Phys. **62**, 113.

Mizukami, Y., M. Haze, O. Tanaka, K. Matsuura, D. Sano, J. Böker, I. Eremin, S. Kasahara, Y. Matsuda, and T. Shibauchi, 2023, Commun. Phys. **6**, 183.

Moon, K., H. Mori, K. Yang, S. M. Girvin, A. H. MacDonald, L. Zheng, D. Yoshioka, and S.-C. Zhang, 1995, Phys. Rev. B **51**, 5138.

Morawetz, K., 2011, J. Stat. Phys. **143**, 482–500.

Moukouri, S., S. Allen, F. Lemay, B. Kyung, D. Poulin, Y. M. Vilk, and A.-M. S. Tremblay, 2000, Phys. Rev. B **61**, 7887.

Mozyrsky, D., and A. V. Chubukov, 2019, Phys. Rev. B **99**, 174510.

Munakata, F., K. Matsuura, K. Kubo, T. Kawano, and H. Yamauchi, 1992, Phys. Rev. B **45**, 10604.

Murphy, S. Q., J. P. Eisenstein, G. S. Boebinger, L. N. Pfeiffer, and K. W. West, 1994, Phys. Rev. Lett. **72**, 728.

Murthy, P. A., I. Boettcher, L. Bayha, M. Holzmann, D. Kedar, M. Neidig, M. G. Ries, A. N. Wenz, G. Zürn, and S. Jochim, 2015, Phys. Rev. Lett. **115**, 010401.

Nakagawa, Y., Y. Kasahara, T. Nomoto, R. Arita, T. Nojima, and Y. Iwasa, 2021, Science **372**, 190.

Nakagawa, Y., Y. Saito, T. Nojima, K. Inumaru, S. Yamanaka, Y. Kasahara, and Y. Iwasa, 2018, Phys. Rev. B **98**, 064512.

Nascimbène, S., N. Navon, K. Jiang, F. Chevy, and C. Salomon, 2010, Nature (London) **463**, 1057.

Nelson, D. R., and J. M. Kosterlitz, 1977, Phys. Rev. Lett. **39**, 1201.

Nikolić, P., and S. Sachdev, 2007, Phys. Rev. A **75**, 033608.

Nishida, Y., and D. T. Son, 2006, Phys. Rev. Lett. **97**, 050403.

Nishida, Y., and D. T. Son, 2007a, Phys. Rev. D **76**, 086004.

Nishida, Y., and D. T. Son, 2007b, Phys. Rev. A **75**, 063617.

Nishida, Y., and D. T. Son, 2010, Phys. Rev. A **82**, 043606.

Norman, M. R., A. Kanigel, M. Randeria, U. Chatterjee, and J. C. Campuzano, 2007, Phys. Rev. B **76**, 174501.

Norman, M. R., M. Randeria, H. Ding, and J. C. Campuzano, 1998, Phys. Rev. B **57**, R11093.

Nozières, P., and S. Schmitt-Rink, 1985, J. Low Temp. Phys. **59**, 195.

Nussinov, Z., and S. Nussinov, 2006, Phys. Rev. A **74**, 053622.

Oda, M., K. Hoya, R. Kubota, C. Manabe, N. Momono, T. Nakano, and M. Ido, 1997, Physica (Amsterdam) **281C**, 135.

Oh, M., K. P. Nuckolls, D. Wong, R. L. Lee, X. Liu, K. Watanabe, T. Taniguchi, and A. Yazdani, 2021, Nature (London) **600**, 240.

O'Hara, K. M., S. L. Hemmer, M. E. Gehm, S. R. Granade, and J. E. Thomas, 2002, Science **298**, 2179.

Ohashi, Y., and A. Griffin, 2002, Phys. Rev. Lett. **89**, 130402.

Oike, H., Y. Suzuki, H. Taniguchi, Y. Seki, K. Miyagawa, and K. Kanoda, 2017, Nat. Commun. **8**, 756.

Okazaki, K., *et al.*, 2014, Sci. Rep. **4**, 4109.

Paalanen, M. A., A. F. Hebard, and R. R. Ruel, 1992, Phys. Rev. Lett. **69**, 1604.

Pai, Y.-Y., A. Tylan-Tyler, P. Irvin, and J. Levy, 2018, Rep. Prog. Phys. **81**, 036503.

Park, J. M., Y. Cao, K. Watanabe, T. Taniguchi, and P. Jarillo-Herrero, 2021, Nature (London) **590**, 249.

Park, T.-H., and H.-Y. Choi, 2019, Phys. Rev. B **99**, 174503.

Partridge, G. B., W. Li, R. I. Kamar, Y. an Liao, and R. G. Hulet, 2006, Science **311**, 503.

Patton, B. R., 1971, Phys. Rev. Lett. **27**, 1273.

Pedersen, A. K., S. Ichinokura, T. Tanaka, R. Shimizu, T. Hitosugi, and T. Hirahara, 2020, Phys. Rev. Lett. **124**, 227002.

Peotta, S., and P. Törmä, 2015, Nat. Commun. **6**, 8944.

Perali, A., P. Pieri, L. Pisani, and G. C. Strinati, 2004, Phys. Rev. Lett. **92**, 220404.

Peters, R., and J. Bauer, 2015, Phys. Rev. B **92**, 014511.

Petrov, D., M. Baranov, and G. Shlyapnikov, 2003, Phys. Rev. A **67**, 031601.

Pieri, P., L. Pisani, and G. C. Strinati, 2004, Phys. Rev. B **70**, 094508.

Pieri, P., and G. Strinati, 2005, Phys. Rev. B **71**, 094520.

Pini, M., P. Pieri, and G. C. Strinati, 2019, Phys. Rev. B **99**, 094502.

Pistolesi, F., and P. Nozières, 2002, Phys. Rev. B **66**, 054501.

Popov, V. N., 2001, *Functional Integrals in Quantum Field Theory, and Statistical Physics* (Springer Science+Business Media, Dordrecht).

Powell, B., and R. H. McKenzie, 2011, Rep. Prog. Phys. **74**, 056501.

Prokof'ev, N., O. Ruebenacker, and B. Svistunov, 2001, Phys. Rev. Lett. **87**, 270402.

Prokof'ev, N., and B. Svistunov, 2002, Phys. Rev. A **66**, 043608.

Proust, C., and L. Taillefer, 2019, Annu. Rev. Condens. Matter Phys. **10**, 409.

Pushp, A., C. V. Parker, A. N. Pasupathy, K. K. Gomes, S. Ono, J. Wen, Z. Xu, G. Gu, and A. Yazdani, 2009, Science **324**, 1689.

Quintanilla, J., B. L. Györffy, J. F. Annett, and J. P. Wallington, 2002, Phys. Rev. B **66**, 214526.

Radzihovsky, L., and D. E. Sheehy, 2010, Rep. Prog. Phys. **73**, 076501.

Randeria, M., and E. Taylor, 2014, Annu. Rev. Condens. Matter Phys. **5**, 209.

Reatto, L., and J. P. Straley, 1969, Phys. Rev. **183**, 321.

Rebec, S. N., T. Jia, C. Zhang, M. Hashimoto, D.-H. Lu, R. G. Moore, and Z.-X. Shen, 2017, Phys. Rev. Lett. **118**, 067002.

Regal, C. A., M. Greiner, and D. S. Jin, 2004, Phys. Rev. Lett. **92**, 040403.

Reyren, N., *et al.*, 2007, Science **317**, 1196.

Rice, J. P., J. Giapintzakis, D. M. Ginsberg, and J. M. Mochel, 1991, Phys. Rev. B **44**, 10158.

Rice, T. M., K.-Y. Yang, and F.-C. Zhang, 2012, Rep. Prog. Phys. **75**, 016502.

Richardson, R., 1963, Phys. Lett. **3**, 277.

Richter, C., *et al.*, 2013, Nature (London) **502**, 528.

Ries, M. G., A. N. Wenz, G. Zürn, L. Bayha, I. Boettcher, D. Kedar, P. A. Murthy, M. Neidig, T. Lompe, and S. Jochim, 2015, Phys. Rev. Lett. **114**, 230401.

Rinott, S., K. Chashka, A. Ribak, E. D. Rienks, A. Taleb-Ibrahimi, P. Le Fevre, F. Bertran, M. Randeria, and A. Kanigel, 2017, Sci. Adv. **3**, e1602372.

Sacépé, B., C. Chapelier, T. I. Baturina, V. M. Vinokur, M. R. Baklanov, and M. Sanquer, 2010, Nat. Commun. **1**, 140.

Sá de Melo, C. A. R., M. Randeria, and J. R. Engelbrecht, 1993, Phys. Rev. Lett. **71**, 3202.

Saito, Y., T. Nojima, and Y. Iwasa, 2016, Nat. Rev. Mater. **2**, 16094.

Sakai, S., M. Civelli, Y. Nomura, and M. Imada, 2015, Phys. Rev. B **92**, 180503.

Samoilov, A. V., 1994, Phys. Rev. B **49**, 1246.

Santander-Syro, A. F., R. P. S. M. Lobo, N. Bontemps, W. Lopera, D. Giratá, Z. Konstantinovic, Z. Z. Li, and H. Raffy, 2004, Phys. Rev. B **70**, 134504.

Scalettar, R. T., E. Y. Loh, J. E. Gubernatis, A. Moreo, S. R. White, D. J. Scalapino, R. L. Sugar, and E. Dagotto, 1989, Phys. Rev. Lett. **62**, 1407.

Schafroth, M. R., 1955, Phys. Rev. **100**, 463.

Scherpelz, P., Y. He, and K. Levin, 2013, Phys. Rev. B **88**, 220507.

Scherpelz, P., A. Rançon, Y. He, and K. Levin, 2014, Phys. Rev. B **90**, 060506.

Scherpelz, P., D. Wulin, K. Levin, and A. K. Rajagopal, 2013, Phys. Rev. A **87**, 063602.

Scheurer, M. S., and J. Schmalian, 2015, Nat. Commun. **6**, 6005.

Schrieffer, J. R., 1964, *Theory of Superconductivity*, 1st ed. (W. A. Benjamin, New York).

Segawa, K., and Y. Ando, 2004, Phys. Rev. B **69**, 104521.

Senthil, T., and M. P. Fisher, 2000, Phys. Rev. B **62**, 7850.

Serene, J. W., 1989, Phys. Rev. B **40**, 10873.

Sewer, A., X. Zotos, and H. Beck, 2002, Phys. Rev. B **66**, 140504.

Shi, H., and A. Griffin, 1998, Phys. Rep. **304**, 1.

Shibauchi, T., T. Hanaguri, and Y. Matsuda, 2020, J. Phys. Soc. Jpn. **89**, 102002.

Sobirey, L., N. Luick, M. Bohlen, H. Biss, H. Moritz, and T. Lompe, 2021, Science **372**, 844.

Sodemann, I., I. Kimchi, C. Wang, and T. Senthil, 2017, Phys. Rev. B **95**, 085135.

Sofo, J., and C. Balseiro, 1992, Phys. Rev. B **45**, 8197.

Sommer, A., M. Ku, G. Roati, and M. W. Zwierlein, 2011, Nature (London) **472**, 201.

Song, Y., *et al.*, 2021, Nat. Commun. **12**, 5926.

Šopík, B., P. Lipavský, M. Männel, K. Morawetz, and P. Matlock, 2011, Phys. Rev. B **84**, 094529.

Sous, J., Y. He, and S. A. Kivelson, 2023, npj Quantum Mater. **8**, 25.

Stajic, J., A. Iyengar, Q. J. Chen, and K. Levin, 2003, Phys. Rev. B **68**, 174517.

Stajic, J., J. N. Milstein, Q. J. Chen, M. L. Chiofalo, M. J. Holland, and K. Levin, 2004, Phys. Rev. A **69**, 063610.

Stewart, J. T., J. P. Gaebler, and D. S. Jin, 2008, Nature (London) **454**, 744.

Strack, P., R. Gersch, and W. Metzner, 2008, Phys. Rev. B **78**, 014522.

Strecker, K. E., G. B. Partridge, and R. G. Hulet, 2003, Phys. Rev. Lett. **91**, 080406.

Strinati, G. C., P. Pieri, G. Röpke, P. Schuck, and M. Urban, 2018, Phys. Rep. **738**, 1.

Sulpizio, J. A., S. Ilani, P. Irvin, and J. Levy, 2014, Annu. Rev. Mater. Res. **44**, 117.

Sun, L., and Q. J. Chen, 2022, Phys. Rev. A **106**, 013317.

Sun, L., J. B. Wang, X. Chu, and Q. J. Chen, 2022, Ann. Phys. (Berlin) **534**, 2100511.

Suyolcu, Y. E., Y. Wang, F. Baiutti, A. Al-Temimy, G. Gregori, G. Cristiani, W. Sigle, J. Maier, P. A. van Aken, and G. Logvenov, 2017, Sci. Rep. **7**, 453.

Suzuki, M., and M. Hikita, 1991, Phys. Rev. B **44**, 249.

Suzuki, Y., K. Wakamatsu, J. Ibuka, H. Oike, T. Fujii, K. Miyagawa, H. Taniguchi, and K. Kanoda, 2022, Phys. Rev. X **12**, 011016.

Tajima, H., P. Pieri, and A. Perali, 2021, Condens. Matter **6**, 8.

Tallon, J. L., J. Loram, G. Williams, J. Cooper, I. Fisher, J. Johnson, M. Staines, and C. Bernhard, 1999, Phys. Status Solidi (b) **215**, 531.

Tallon, J. L., J. W. Loram, J. R. Cooper, C. Panagopoulos, and C. Bernhard, 2003, Phys. Rev. B **68**, 180501.

Tamaki, H., Y. Ohashi, and K. Miyake, 2008, Phys. Rev. A **77**, 063616.

Tan, S., 2008, Ann. Phys. (N.Y.) **323**, 2952.

Tan, S., and K. Levin, 2004, Phys. Rev. B **69**, 064510.

Tan, S., and K. Levin, 2006, Phys. Rev. A **74**, 043606.

Tchernyshyov, O., 1997, Phys. Rev. B **56**, 3372.

Thouless, D. J., 1960, Ann. Phys. (N.Y.) **10**, 553.

Timusk, T., and B. Statt, 1999, Rep. Prog. Phys. **62**, 61.

Törmä, P., S. Peotta, and B. A. Bernevig, 2022, Nat. Rev. Phys. **4**, 528–542.

Tremblay, A.-M., B. Kyung, and D. Sénéchal, 2006, Low Temp. Phys. **32**, 424.

Trivedi, N., and M. Randeria, 1995, Phys. Rev. Lett. **75**, 312.

Tung, S., G. Lamporesi, D. Lobser, L. Xia, and E. A. Cornell, 2010, Phys. Rev. Lett. **105**, 230408.

Uemura, Y. J., 1997, Physica (Amsterdam) **282C–287C**, 194.

Uemura, Y. J., *et al.*, 1989, Phys. Rev. Lett. **62**, 2317.

Ullah, S., and A. T. Dorsey, 1991, Phys. Rev. B **44**, 262.

Varma, C. M., 2020, Rev. Mod. Phys. **92**, 031001.

Veillette, M. Y., D. E. Sheehy, and L. Radzihovsky, 2007, Phys. Rev. A **75**, 043614.

Vishik, I., 2018, Rep. Prog. Phys. **81**, 062501.

Viverit, L., S. Giorgini, L. Pitaevskii, and S. Stringari, 2004, Phys. Rev. A **69**, 013607.

Volcko, D., and K. F. Quader, 2012, Phys. Rev. Lett. **109**, 235303.

Wagner, G., D. X. Nguyen, S. H. Simon, and B. I. Halperin, 2021, Phys. Rev. Lett. **127**, 246803.

Wallington, J. P., and J. F. Annett, 2000, Phys. Rev. B **61**, 1433.

Wang, Q.-Y., *et al.*, 2012, Chin. Phys. Lett. **29**, 037402.

Wang, Z., C. Liu, Y. Liu, and J. Wang, 2017, J. Phys. Condens. Matter **29**, 153001.

Wang, Z. Q., G. Chaudhary, Q. J. Chen, and K. Levin, 2020, Phys. Rev. B **102**, 184504.

Wang, Z. Q., I. Mandal, S. B. Chung, and S. Chakravarty, 2014, Ann. Phys. (N.Y.) **351**, 727.

Watanabe, T., T. Fujii, and A. Matsuda, 1997, Phys. Rev. Lett. **79**, 2113.

Wu, C.-T., B. M. Anderson, R. Boyack, and K. Levin, 2015a, Phys. Rev. B **91**, 220504.

Wu, C.-T., B. M. Anderson, R. Boyack, and K. Levin, 2015b, Phys. Rev. Lett. **115**, 240401.

Wulin, D., H. Guo, C.-C. Chien, and K. Levin, 2012, Phys. Rev. B **86**, 134518.

Wulin, D., Y. He, C.-C. Chien, D. K. Morr, and K. Levin, 2009, Phys. Rev. B **80**, 134504.

Wulin, D., and K. Levin, 2012, Phys. Rev. B **86**, 134519.

Xia, J., *et al.*, 2008, Phys. Rev. Lett. **100**, 127002.

Yazdani, A., and A. Kapitulnik, 1995, Phys. Rev. Lett. **74**, 3037.

Yokoyama, H., M. Ogata, and Y. Tanaka, 2006, J. Phys. Soc. Jpn. **75**, 114706.

Yu, G., *et al.*, 2019, Phys. Rev. B **99**, 214502.

Yu, Y., L. Ma, P. Cai, R. Zhong, C. Ye, J. Shen, G. D. Gu, X. H. Chen, and Y. Zhang, 2019, Nature (London) **575**, 156.

Zhang, J., H. Hu, X.-J. Liu, and H. Pu, 2014, in *Annual Review of Cold Atoms and Molecules*, Vol. 2, edited by K. W. Madison, K. Bongs, L. D. Carr, A. M. Rey, and H. Zhai (World Scientific, Singapore), Chap. 2, pp. 81–143.

Zhang, P., *et al.*, 2018, Science **360**, 182.

Zhang, S., G. Miao, J. Guan, X. Xu, B. Liu, F. Yang, W. Wang, X. Zhu, and J. Guo, 2019, Chin. Phys. Lett. **36**, 107404.

Zhang, T., *et al.*, 2010, Nat. Phys. **6**, 104.

Zhang, W., C. A. Sackett, and R. G. Hulet, 1999, Phys. Rev. A **60**, 504.

Zhang, W.-H., *et al.*, 2014, Chin. Phys. Lett. **31**, 017401.

Zhao, L., C. Belvin, R. Liang, D. Bonn, W. Hardy, N. Armitage, and D. Hsieh, 2017, Nat. Phys. **13**, 250.

Zhao, W., *et al.*, 2013, Solid State Commun. **165**, 59.

Zhou, P., L. Chen, Y. Liu, I. Sochnikov, A. T. Bollinger, M.-G. Han, Y. Zhu, X. He, I. Bozovic, and D. Natelson, 2019, Nature (London) **572**, 493.

Zwerger, W., 2012, Ed., *The BCS-BEC Crossover and the Unitary Fermi Gas*, Lecture Notes in Physics Vol. 836 (Springer-Verlag, Berlin).

Zwierlein, M. W., J. R. Abo-Shaeer, A. Schirotzek, C. H. Schunck, and W. Ketterle, 2005, Nature (London) **435**, 1047.

Zwierlein, M. W., A. Schirotzek, C. H. Schunck, and W. Ketterle, 2006, Science **311**, 492.

Zwierlein, M. W., C. A. Stan, C. H. Schunck, S. M. F. Raupach, S. Gupta, Z. Hadzibabic, and W. Ketterle, 2003, Phys. Rev. Lett. **91**, 250401.

Zwierlein, M. W., C. A. Stan, C. H. Schunck, S. M. F. Raupach, A. J. Kerman, and W. Ketterle, 2004, Phys. Rev. Lett. **92**, 120403.